UNIVERSITY OF SALERNO

DEPARTMENT OF CHEMISTRY AND BIOLOGY "A. ZAMBELLI"

and

UNIVERSITY OF BASILICATA

DEPARTMENT OF SCIENCE

Ph.D. in Chemistry

XXX Cycle

CHIM/02 – Physical Chemistry

Thesis in

PHYSICAL CHEMISTRY OF PLASMAS AND APPLICATIONS TO CULTURAL HERITAGE AND MATERIAL SCIENCE

TUTOR:
Prof. Roberto Teghil

CO-TUTOR:
Prof. Angela De Bonis

EXTERNAL TUTOR:
Dr. Antonio Santagata

COORDINATOR:
Prof. Gaetano Guerra

Ph. D. Student:
Antonella Smaldone
mat. 8800100007

Academic Year 2016/2017

Acknowledgements

First of all I would like to thank my supervisors Prof. Roberto Teghil, Prof. Angela De Bonis and Dr. Antonio Santagata for their encouragement and support during my PhD period and for guiding me throughout the entire course of this study.

My sincere thanks also goes to Dr. Sergio Brutti, who provided me an opportunity to access to his laboratory and to work under his guide on the new project of micro batteries.

A big thanks to the technicians and colleagues of the Laser laboratory group: Agostino Galasso, Alessandro Laurita, Neluta Ibris, Maria Sansone and Mariangela Curcio for all their friendship, help and generally for taking care of me for the last three years.

I wish to thank Basilicata Archaeological Bureau, especially Dr. Teresa Elena Cinquantaquattro, for giving me the precious objects that we have analyzed.

I am grateful to Institute for Technologies Applied to Cultural Heritage (ITABC) of National Research Council, especially dr. Marco Ferretti, for XRF experiments.

Anyway, this long journey would not have been possible without the unconditional support of my family.

I would like to express my heartiest gratitude to my father, my mother and my brother for their love and endless encouragement.

Finally, my special thanks go to my lovely boyfriend, Stefano. His love, sacrifice, understanding, patience and eternal support have made this thesis possible.

Contents

List of Figures

List of Table

Introduction

Laser is an integral part of numerous applications in today's technology, including science, medicine, industry, electronics, communication, entertainment and in the military.

Focusing the light of laser pulses on a materials, the laser – matter interaction produces a plasma, with a physical process named as laser ablation.

Therefore, the term 'ablation' refers to the removal of material by complex chemical physical process which occurs after the laser – target interaction.

From the point of view of scientific applications, the laser ablation can be used in different ways.

When the ablation occurs in vacuum or gaseous environment, it is possible to obtain a micro or nano – structured thin film through Pulsed Laser Deposition technique (PLD), in which a substrate is put in front of the target, i.e. along the direction of plasma expansion.

On the contrary, when the ablation takes place in liquid environment, a colloidal solution of nano – structures is obtained. This happens in Laser Ablation in Liquids (LAL).

Finally, the laser induced plasma can be used to characterize materials by measuring the light emission from the plasma.

The optical radiation emitted is due to specific elements hence gives unique spectroscopic signatures of the atoms and ions present and provides technique to identify elemental characteristics of materials.

The spectroscopic technique that uses the plasma emission is known as Laser Induced Breakdown Spectroscopy (LIBS)

One of the distinguishing features of LIBS is its capability to carry out the characterization of the LIP. The spectroscopy of the radiation emitted by LIP may be used to obtain the characteristic physical parameters.

Thesis overview

The aim of this work is to highlight the capabilities of LIBS performed by ultra short femtosecond laser as analytical technique for archaeological sample measurement.
The analysis are performed on bronze and silver objects using different analytical procedure.
On the other hand, the laser ablation process is also used for another application, i.e. pulsed laser deposition.
A nanosecond laser is used for PLD technique in order to produce thin films of $LiCo_{0.9}Fe_{0.1}PO_4$ for micro Lithium Ion Batteries.
This thesis is presented as follows:

Chapter 1 provides an introduction to relevant background information about Laser Induced Breakdown Spectroscopy technique and mechanism of laser ablation process.

Chapter 2 provides a description of the characteristic parameters used for describing temporal and spatial evolution of a Laser Induced Plasma.

Chapter 3 presents a discussion of different quantitative method used in LIBS analysis.

Chapter 4 describes the experimental setup of ultra-short LIBS and methodology used to optimize the CF inverse LIBS method, presenting the results obtained from an investigation of standard samples.

In Chapter 5 the CF inverse LIBS method, optimize previously, is applied to a three case studies in field of Cultural Heritage. These studies investigate the applicability of

method as useful for quantitative analysis, comparing the results with those obtained with other techniques.

Chapter 6 presents a study of plasma plume generated by ns laser from a target of $LiCo_{0.9}Fe_{0.1}PO_4$ in order to evaluate the influence of different pressure conditions. Finally, using PLD technique, thin films of this material are deposited and the effects of pressure and substrate temperature are investigate.

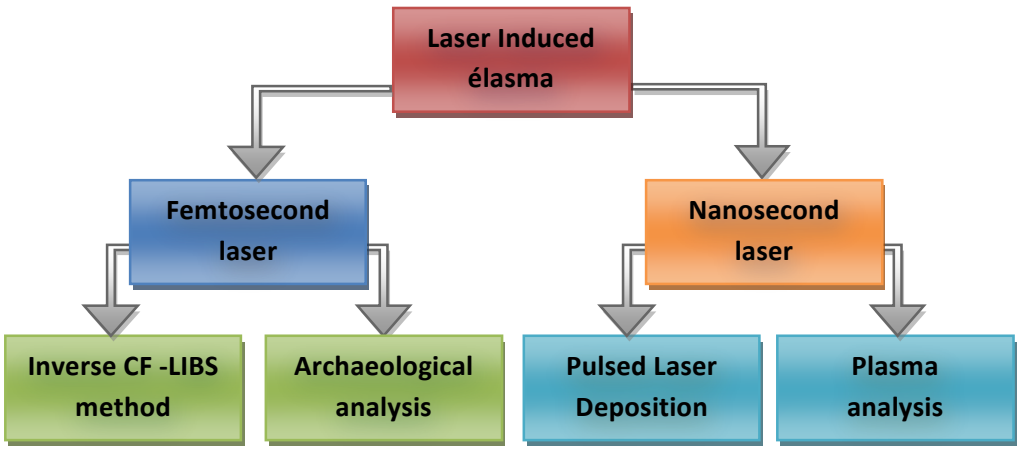

Chapter 1

Physical Chemistry of Laser Induced Plasmas: Laser Induced Breakdown Spectroscopy

i. History of Laser Induced Breakdown Spectroscopy

The Physical Chemistry characteristics of Plasmas induced by laser pulses can be summarized by taking into account the LIBS technique which has become a popular approach among other atomic emission spectroscopy methods from the seventies of the 20th century, in connection with the invention and development of lasers.

Nevertheless the intense study of LIBS took place only in the last three decades, when the more advanced instruments were introduced.

The first publication about the use of LIBS as analytical technique is in the report by L. Radziemski and D. Cremers in the 1980's [1].

Since 1990's, with the advent of high resolution spectrometers, that allowed multiple elements to be detected at once, the LIBS technique has become very important and an increasing number of articles has been published [1]–[8].

Moreover, the optimization of LIBS system has been used for various applications and for the theoretical understanding of the spatial and temporal evolution of the plasma plume. In the past ten years, many review articles have been published, such as review

by Hahn and Omenetto [9] on fundamental and applications of LIBS or by Gornushkin and Panne [10] on modelling of the plasmas.

1.1. General description of LIBS

Laser Induced Breakdown Spectroscopy (LIBS), sometimes also called Laser Induced Plasma Spectroscopy (LIPS), is an analytical technique that employs a laser pulses to ablate a small amount of material in order to obtain qualitative and quantitative information [11].

In comparison to other analytical techniques, LIBS experimental setup is very simple and includes a few main components:

- laser source: the most widely used laser in LIBS experiments is nanoseconds Nd:YAG, that provides wavelengths in a spectral range from UV to NIR (266, 355, 532 and 1064 nm);
- spectrometer;
- focusing optics;
- detector;
- computer for data acquisition;

A simple schematic scheme of LIBS technique is shown in Fig. 1.1.

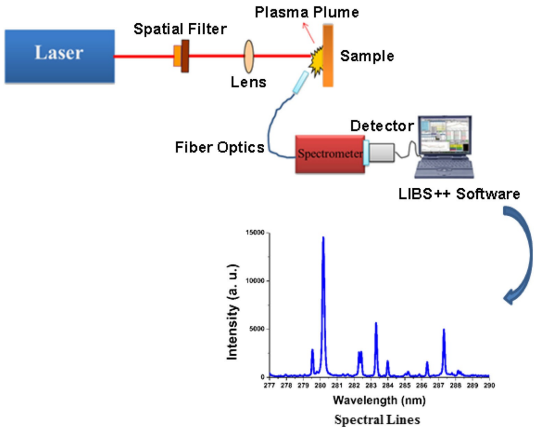

Fig. 1.1.: Scheme of a basic LIBS setup

In LIBS measurements, the experimental conditions (laser pulse energy, time delay, gate width, laser wavelength, gas pressure) vary from sample to sample, therefore the

optimal conditions must be chosen for each experiments, but when they are found, LIBS analysis becomes very fast.

From laser-matter interaction, various complex processes take place: atomization, ionization and evaporation of small amount of the sample (in order of nanograms or micrograms).

A plasma is formed which cools down quickly and, during the cooling process, the electrons and ions recombination results in emission of spectral lines of characteristic wavelengths.

The LIBS method is based on the analysis of the obtained spectra: the emission lines of the excited atoms and ions reveal information about the target composition.

The plasma emission is then collected and focused in a spectrometer coupled with a CCD or an ICCD camera.

Finally, the LIBS spectrum is obtained in the form of the graph of intensity (a.u.) vs. wavelength (nm) through a computer elaboration.

LIBS is a versatile and practical technique and presents many advantages, such as:

- simple or no pre-treatment of the target sample;
- simultaneous multi-element analysis;
- non-contact system, can be used for analysis in hazardous environments;
- micro or non destructive analysis because only a small amount of material is consumed during this process;
- fast measurement speed of analysis;
- portability of the LIBS system, useful for *in situ* analysis.

A further advantage of LIBS system is that can be used to study different kinds of materials in all physical states (solid, liquid and gaseous) obtaining spectra which contain information about the elemental composition of the sample under study [8].

For these reasons, LIBS technique has been employed in numerous applications including industrial processes [12], [13], environmental chemistry and biology [14]–[17], cultural heritage [18], [19], geology and mineralogy [20]–[22] and is a highly competitive technique compared with other conventional analytical methods. For

example, the biggest achievement in the field of LIBS is ChemCam LIBS, developed by NASA, which is attached to the Curiosity rover, in order to provide analyses on the planet Mars [23], [24].

Recently, to handle large amount of data, advanced Chemiometric algorithms are used, for data set analysis and processing. In this way, each sample can be classified into groups, clustered together or be discriminated based on the LIBS spectra [25]–[27].

A most attractive features of LIBS is the possibility to obtain qualitative and quantitative analyses at atmospheric gas pressure without the need of and vacuum chambers, therefore it is not surprising that LIBS in diluted gases has been rarely considered, with respect to atmospheric pressure ones [28].

The micro or non-destructive analysis can be useful for the analysis of rare and precious samples, where sample destruction is absolutely undesirable.

Thanks to this characteristic, elemental composition of rare and precious objects can be done, without significant damage [29]–[31].

Unfortunately, despite all these advantages, LIBS also presents some important limitations [32].

LIBS applications are limited because of low limit of detection (LOD) and poor reproducibility.

The concept of limit of detection is defined as the lowest concentration of a particular analyte in a matrix that can be detected by an analytical technique.

In general, using the LIBS technique, LOD falls in the range of parts per million (ppm), whereas other established analytical techniques such as ICP-MS gives precise measurements of the order of parts per billion (ppb) in most cases [33].

Other interferences for quantitative LIBS measurements are self-absorption and matrix effects [34]–[36].

Self-absorption occurs when the emission from the hotter region of plasma is absorbed by cooler atoms surrounding the high-temperature core.

The matrix of samples and their different physical chemical properties can significantly affect the ablation dynamics, the plasma composition, the plasma temperature and, in turn, the LIBS signal.

The intensities of detected spectral line are related to the amount of corresponding element in the plasma plume and that can be used for quantitative analysis.

However, for quantitative analysis, different approaches may be applied and will be explained in detail in the next paragraphs.

The first is the classical calibration curve method and is based on construction of the calibration curves, utilizing samples with known composition, namely reference standard materials, whose matrices are very similar to the sample under investigation.

The second approach is defined Calibration-Free (CF) method because it does not require reference materials, but is based on three theoretical assumptions (Local Thermodynamic Equilibrium, optically thin plasma and stoichiometric ablation), that have to be fulfilled in order to ensure the reliability of analysis, and on plasma parameters (electron temperature and electron density), that have to be precisely determined.

1.2. Laser-matter interaction

A general process of laser-matter interaction can be explained with these steps [37]:

(1) At first, a pulsed laser beam is focused onto the surface of the sample under study

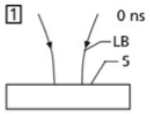

(2) Subsequently, the energy of radiation is locally transmitted into the material with a laser/matter interaction

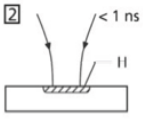

(3) Therefore, the sample begins to heat and to evaporate

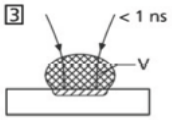

(4) A small amount of sample is ablated and a Laser Induced Plasma (LIP) is formed and expands into the space.

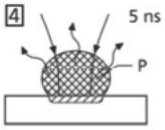

(5) The particles forming the plasma are excited and, while relaxing, emit element-specific radiation, which is detected in order to realize spectroscopic analysis

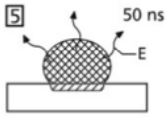

(6) (7) The energy of the plasma is dissipated and the plasma temperature decays

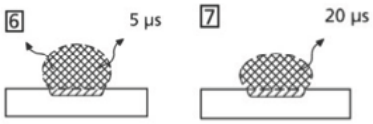

(8) Finally, a crater is formed onto sample surface

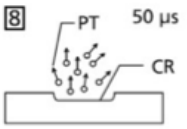

This is a very simplified description of LIP formation, that is, actually, a complex process, depending on several variables, that are [38]:

- laser irradiance;
- laser wavelength;
- thermal, optical and mechanical properties of the target material;
- duration of the laser pulse (τ);
- ambient of surrounding environment (air, He, Ar, O_2, liquid…).

The main laser parameter is pulse duration, as explained in the next section, because different laser-mater interaction mechanisms occur using short or ultra – short pulsed lasers.

Regarding the material properties, a feature that strongly affects the laser – matter interaction is the phase of the sample [8].

From wavelength point of view, using laser with shorter wavelengths, bonds easier break than using longer wavelengths laser because of their higher photon energies. Moreover, the shockwave velocity increases with the decrease laser wavelength, since the penetration depth decreases with the laser wavelength [39].

To conclude this part, LIP properties, its expansion times and dynamics are strongly dependent on the energy of laser beam, its duration and wavelength, on laser matter interaction, on state of the matter and its composition, and on ambient conditions.

1.3 Target material

The materials can be classified on the basis of theelectrical properties, obtaining three major classes: metals, semiconductors and dielectrics, that show different mechanisms of ablation due primarily to their band structures (Fig. 1.2.).

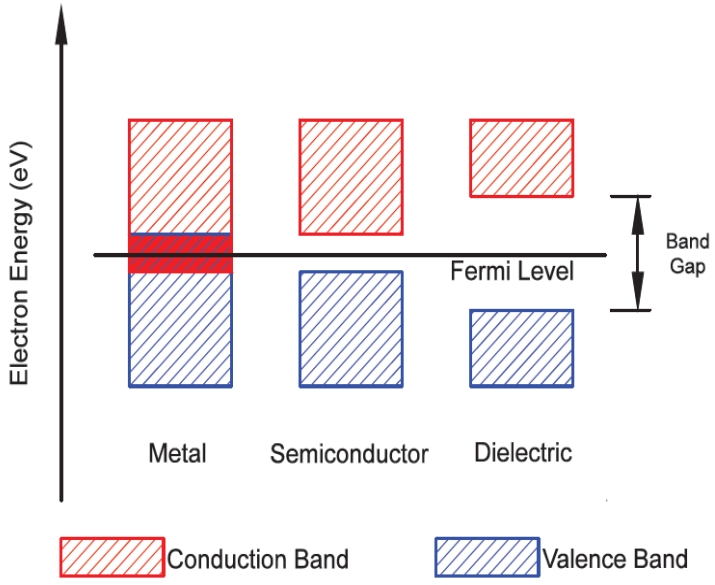

Fig. 1.2.: Schematic image of the band structure of three major groups of materials

1.3.1 Metallic systems

For metallic samples, the most simple systems, there is no energy separation between the conduction band and the valence band so the electrons are then directly excited,

by laser radiation, at higher energy levels. Ionization will start with absorption of laser photons by free electrons on the conduction band.

In general, for metallic target, where the relaxation of photon-excited electrons to the lattice is very rapid, the energy transport due to interactions between laser pulses and target can be described by a simplified model, known as **Two – Temperature Model** (TTM) [8].

This theoretical approach is one – dimensional diffusion model, where electrons and lattice are considered as two sub – systems with their corresponding heat capacities and temperatures [41].

At first, laser beam photons are absorbed by free electrons of the target, leading to the formation of a gas of hot carriers which, subsequently, transfer energy to the lattice through phonons excitation [42]

At the end, the lattice and electron gas reach equilibrium therefore the temperature of the electron gas (T_e) and the temperature of the lattice (T_l) are the same.

The equilibrium occurs on a time-scale ranging from 10^{-12} to 10^{-11} s [41]:

$$C_e \frac{\partial T_e}{\partial t} = -\frac{\partial}{\partial z}\left(k_e \frac{\partial}{\partial z} T_e\right) - \gamma(T_e - T_i) + I(t)A\alpha e^{-\alpha z} \quad \text{(eq. 1.1.)}$$

$$C_l \frac{\partial T_l}{\partial t} = \gamma(T_e - T_l) + I(t)A\alpha e^{-\alpha z} \quad \text{(eq. 1.2.)}$$

In the equations, z is the direction perpendicular to the target surface, the term ($k_e\delta/\delta z T_e$) is the heat flux, the term $I(t)A\alpha e^{-\alpha z}$ represents the laser heating source, I(t) is the laser intensity, A = 1 – R and α are the surface transmissivity and the material absorption coefficient, C_e and C_l are the heat capacities (per volume unit) of the electron and lattice subsystems, γ is the parameter characterizing the electron-lattice coupling, k_e is the electron thermal conductivity [6].

Since in a metal system the electron thermal conductivity is higher than the thermal

conductivity of lattice, the latter can be neglected in eq. 1.1.

On the other hand, the electronic heat capacity is much less than the lattice heat capacity, therefore electrons can be heated to very high transient temperature.

When the electron temperature remains smaller than the Fermi energy, the electron heat capacity and the non – equilibrium electron thermal conductivity are given by:

$$C_e = C'_e T_e$$

(eq. 1.3.)

where C'_e is a constant and$k_e = k_0(T_l) \cdot T_e/T_l$, and $k_0(T_l)$ is the equilibrium thermal conductivity of a metal.

In eq. 1.1. and eq. 1.2. it is great important consider three time scales: τ_e, τ_l and τ_L, where:

- τ_e represents the electron cooling time: $\tau_e = C_e/\gamma$;
- τ_l corresponds at the lattice heating time ($\tau_e << \tau_l$): $\tau_l = C_l/\gamma$
- τ_L is the duration of the laser pulse.

So these parameters define three different regimes of the laser – metal interaction: femtosecond, picoseconds and nanosecond regimes [6].

1.3.1.1 TTM in femtosecond regime

With femtosecond pulses, the laser pulse duration is shorter than the electron cooling time, $\tau_L << \tau_e$. In this case $C_eT_e/t >> \gamma T_e$ and the electron – lattice coupling can be neglected [6].

When this condition is fulfilled $(k_e/C_e)\tau_L < \alpha^{-2}$ (where k_e/C_e is the electron thermal diffusivity), and it is possible to neglect the electron heat conduction term in order to have a solution of equation 1.1. The equation 1.1. can be reduces to:

$$C'_e \frac{\partial T_e^2}{\partial t} = 2I_0 A \alpha e^{-\alpha z}$$

(eq. 1.4.)

and gives:

$$T_e(t) = \sqrt{T_0^2 + \frac{2I_0 A\alpha}{C_e'} t\, e^{(-\alpha z)}}$$

(eq. 1.5.)

where $I(t) = I_0$ is assumed constant, and $T_0 = T_e(0)$ is the initial temperature.

At the end of the laser pulse the electron temperature is given by:

$$T_e(\tau_L) \cong \sqrt{\frac{2F_\alpha \alpha}{C_e'}} e^{\left(-\frac{z\alpha}{2}\right)}$$

(eq. 1.6.)

where $T_e(\tau_L) >> T_0$ is assumed, $F_\alpha = I_0 A \tau_L$ is the absorbed laser fluence.

After the laser pulse, the electrons are rapidly cooled due to the energy transfer to the lattice and heat conduction into the bulk. The electron cooling time is very short thus the eq. 1.2. can be written as:

$$T_i \approx T_e(\tau_L)\, t/\tau_l$$

(eq. 1.7.)

The lattice temperature is determined by the average cooling time of the electrons and is given by:

$$T_l \cong T_e^2(\tau_L) \frac{C_e'}{2C_l} \cong \frac{F_a \alpha}{C_l} e^{-\alpha z}$$

(eq. 1.8.)

The time scale of electron cooling and the energy transfer to the lattice is of the order of 1 ps. It is possible to obtain the condition for strong evaporation when $C_i T_i$ becomes larger than $\rho\Omega$, where ρ is the density and Ω is the specific heat of evaporation per unit mass:

$$F_a \geq F_{th} e^{\alpha z}$$

(eq. 1.9.)

where $F_{th} \approx \rho\Omega/\alpha$ is the threshold laser fluence for evaporation with femtosecond pulses. Then the ablation depth per pulse L is:

$$L \cong \alpha^{-1} \ln\left(\frac{F_a}{F_{th}}\right)$$

(eq. 1.10.)

Due to the very short time scales involved in the ablation with femtosecond laser pulses, the ablation process can be regarded as a direct solid – vapour transition.
In this situation, the lattice is heated on a picosecond time scale which leads to the creation of vapour plasma phases followed by a rapid expansion.
During all these processes, thermal conduction into the target can be ignored, in a first approximation.
This is an advantages of femtosecond laser pulses, which allows very precise laser – processing of metals and other targets.

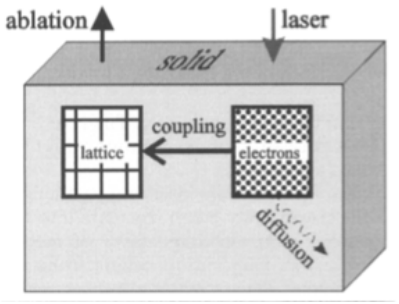

Fig. 1.3.: Schematic of fs laser ablation

1.3.1.2. TTM in picosecond regime

With picosecond laser pulses, the fulfilled condition is $\tau_e << \tau_L << \tau_I$.
The lattice temperature remains much lower than the electron temperature [6].
In this case the electron cooling is due to the energy exchange with the lattice.
The electron temperature and the lattice temperature at the end of the laser pulse are given by:

$$T_e \cong \frac{I_a \alpha}{\gamma} e^{-\alpha z}$$

(eq. 1.11.)

$$T_l \cong \frac{F_a \alpha}{C_l} e^{-\alpha z}$$

(eq. 1.12.)

Since $\tau_e << \tau_L$, the lattice temperature and the lattice temperature at the end of the laser pulse are approximately equal.

With femtosecond and picosecond lasers, the expressions are the same, therefore the logarithmic dependence of the ablation depth on the laser pulse fluence is also possible.

A strong approximation for metal target ablated in the picosecond regime is to neglect the electron heat conduction into the target but, in this case, laser ablation is accompanied by heat conduction and formation of a melted zone inside the target.

At the surface the evaporation can be considered as a direct solid – vapour transition.

1.3.1.3. TTM in nanosecond regime

Using nanosecond laser, the condition $\tau_L >> \tau_l$ is fulfilled [6] and the electron and the lattice temperatures are equal ($T_e = T_l = T$), so the eq. 1.1. can be reduced to:

$$C_l \frac{\partial T}{\partial t} = \frac{\partial}{\partial z}\left(k_0 \frac{\partial T}{\partial z}\right) + I_0 A \alpha e^{-\alpha z}$$

(eq. 1.13.)

With this laser pulses the absorbed laser energy first heats the target surface to the melting point and then to the vaporization temperature.

During the interaction, the large part of energy is lost by the heat conduction into the solid target. The ablation with ns laser pulses is enough long-lasting for the thermal

wave to propagate into the target and to create a relatively large layer of melted material [9]. The heat penetration depth is:

$$l \approx \sqrt{Dt}$$

(eq. 1.14.)

where D is the heat diffusion coefficient and corresponds to k_0/C_i.

With nanosecond laser ablation, the pulses is long enough to propagate a thermal wave into target and to create a molten layer around the ablation crater.

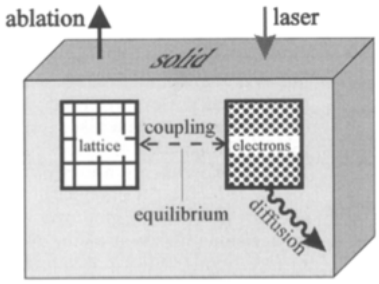

Fig. 1.4.: Schematic of ns laser ablation

On the contrary of the process occurring by ns lasers, ultra short laser pulses avoid the widespread melting of the laser incident zone together with a limited damage of surrounding target surface [43][44].

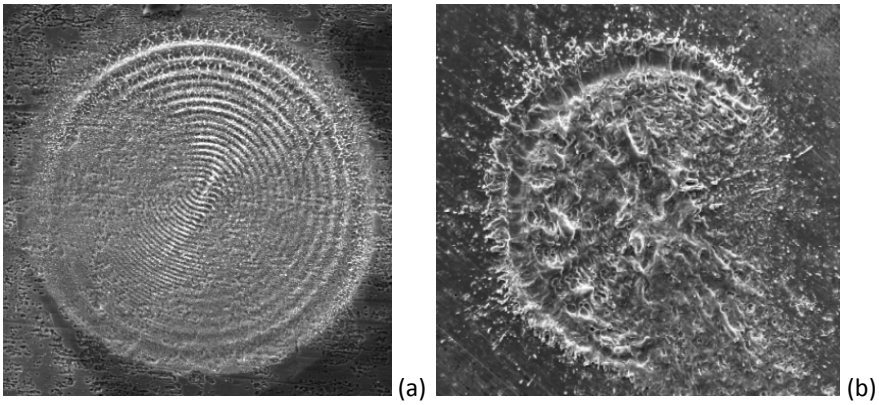

Fig. 1.5.: Damage induced by 10 shots of femtosecond pulsed laser (a) and nanosecond pulsed laser (b) on a bronze standard (sample B22)

Fig. 1.5.(a) shows the regular formation of periodic surface structures due to non thermal processes whereas Fig. 1.5.(b) displays melted features caused by a typical thermal mechanism.

It is clearly seen that in the case of fs ablation a ripple pattern has appeared and that the periodicity of the ripples is of the order of the laser wavelength. In the case of metals, the ripple pattern is almost always perpendicular to the direction of the polarization of the incoming light [45].

1.3.2. Insulating and semiconductor systems

The interaction between the laser radiation and the non metallic materials is more complex and there is no overall model to describe it. Considering also that in the follow LIBS will be applied to metal artefacts, only a brief description will be here reported for semiconductors and insulators.

In insulating and semiconductors materials, the difference in energy between conduction band and valence band (E_{gap}) can be lower or greater than the energy of laser radiation (hv_L).

If $E_{gap} < hv_L$, the absorption coefficient exceed 10^5 cm^{-1} so a large amount of electrons are promoted in the conduction band. The excited electrons retain the energy surplus as kinetic energy which can be transferred ($t \approx 1$ ps) to the lattice producing phonon excitations. So, for these semiconductors the laser ablation can be explained in terms of thermal vaporization.

If $E_{gap} > hv_L$, this means that a multiphoton absorption is necessary to have an electronic transition. Taking into account the very low cross section of multiphoton absorption, to explain the ablation in these materials, it is necessary to consider the defects present in the target or induced by the laser.

The excited states of the defects are found in E_{gap}, therefore these excited states may be involved in photon absorption.

The relaxation of these excited states is possible through the emission of weakly bound atoms (WBA) from the surface of the solid.

Alternatively, the excited states can form metastable states due to local deformations in the lattice causing alterations of internuclear distances.
The WBA are concentrated on the surface and around the defect and, when one of these atoms is released from the surface of a solid, another adjacent defect can arise therefore producing a cascade emission of WBA .
The number of atoms emitted during the ablation is proportional to the power of laser fluence.

1.4. Effect of background environment

When a high – power laser pulse hits a solid surface, the produced plasma can expands over the surface in a background gas, in vacuum or in liquid.
In the case of gaseous media, pressure and chemical nature of the gas are the main parameters that influence the plasma size, lifetime and velocity, as well as the energy exchange and emission properties [39] because the vaporized material may interact with background gas.
The quantity of ablated mass is independent from the ambient gas, since the latter is not directly involved in the very processes of absorption of the laser energy by the target.
Nonetheless, in different gas pressures, different plasma expansion dynamics are observed. In addition, the environment in which plasma and shockwave are formed plays as well a crucial role in the expansion dynamics and in the energy exchange at the contact wall.

1.4.1 Atmospheric pressure background gas

The pressure of the surrounding medium strongly influences the plasma confinement. When the plasma and the surrounding gas reach the gas-dynamic equilibrium (i.e. when the LIP pressure becomes comparable with that at the contact wall), expansion is braked and the plasma remains confined inside the contact wall.

In this stage the plasma is still characterized by high electron number density (10^{16} – 10^{19} cm^{-3}), but spectra are mainly characterized by typical discrete and intense peaks whose intensity reflects the population of the excited levels of emitting species. In this case, the main application is the chemical analysis by LIBS.

The surrounding media influences the final plasma size, the speed of the expansion and the emission properties of the plasma.

At atmospheric pressure the plasma characteristics mainly depends on the molar mass of the gas whereas the quantity of ablated mass is independent from the ambient gas.

1.4.2 Low pressure background gas

Spectroscopic features of LIPs in low pressure environment are similar to those described in the previous section but in this case the expansion is much faster, thus lower electron number density is observed and consequently spectral lines appear more thin and resolved [46].

LTE deviations for should be taken into account because the expansion time could be comparable with the characteristic recombination time (10^{-7} s).

The LIP expansion dynamics can be highly dependent on the background gas pressure and type and these differences can be useful for another relevant application of laser ablation, such as PLD.

In some cases, when a reactive ambient gas is used (e.g. air, O_2, N_2, etc.), strong mixing can occur at the contact surface between the LIP and the ambient gas.

PLD is an interesting technique for producing thin films depositing the ablated material on a substrate in a vacuum chamber.

Furthermore, the analysis of the emission spectra can provide useful information about the transport of laser ejected-material to the substrate, which in turn can be exploited to correlate the ablation process to the film properties.

During PLD, as a consequence of the low pressure, the spectra interpretation is more difficult with respect of air experiments because of the faster dynamics.

1.5. References

[1] L. J. Radziemski, T. R. Loree, and D. A. Cremers, "Laser Induced Breakdown spectroscopy (LIBS): A new spectrochemical technique," *Opt. Laser Remote Sens.*, vol. 39, pp. 303–307, 1983.

[2] L. J. Radziemski, T. R. Loree, D. A. Cremers, and N. M. Hoffman, "Time-Resolved Laser-Induced Breakdown Spectrometry of Aerosols," *Opt. Laser Remote Sens.*, vol. 55, pp. 1246–1252, 1983.

[3] D. A. Cremers and L. J. Radzlemski, "Detection of Chlorine and Fluorine in Air by Laser-Induced Breakdown Spectrometry," *Anal. Chem.*, vol. 55, no. 8, pp. 1252–1256, 1983.

[4] C. M. Davies, H. H. Telle, and D. J. Montgomery, "Quantitative analysis using remote laser-induced breakdown spectroscopy (LIBS)," *Spectrochim. Acta Part B*, vol. 50, pp. 1059–1075, 1995.

[5] R. Sattmann, V. Sturm, and R. Noll, "Laser-induced breakdown spectroscopy of steel samples using multiple Q-switch Nd:YAG laser pulses," *J. Phys. D. Appl. Phys.*, vol. 28, pp. 2181–2187, 1995.

[6] B. N. Chichkov, C. Momma, S. Nolte, F. von Alvensleben, and A. Tünnermann, "Femtosecond, picosecond and nanosecond laser ablation of solids," *Appl. Phys. A Mater. Sci. Process.*, vol. 63, no. 2, pp. 109–115, 1996.

[7] I. B. Gornushkin, M. Clara, B. W. Smith, J. D. Winefordner, and U. Panne, "Time-resolved resonance shadow imaging of laser-produced lead and tin plasmas," *Spectrochim. Acta Part B*, vol. 52, pp. 1617–1625, 1997.

[8] D. A. Rusak, B. C. Castle, B. W. Smith, and J. D. Winefordner, "Fundamentals and Applications of Laser-Induced Breakdown Spectroscopy," *Crit. Rev. Anal. Chem.*, vol. 27, no. 4, pp. 257–290, 1997.

[9] N. Omenetto and D. W. Hahn, "Laser-Induced Breakdown Spectroscopy (LIBS), Part I: Review of Basic Diagnostics and Plasma – Particle Interactions: Still-Challenging Issues Within the Analytical Plasma Community," vol. 64, pp. 335–366, 2010.

[10] I. B. Gornushkin, S. V Shabanov, S. Merk, E. Tognoni, and U. Panne, "Effects of non-uniformity of laser induced plasma on plasma temperature and concentrations determined by the Boltzmann plot method : implications from plasma modeling," *J. Anal. At. Spectrom.*, vol. 25, pp. 1643–1653, 2010.

[11] F. J. Fortes, J. Moros, P. Lucena, L. M. Cabalín, and J. J. Laserna, "Laser-induced

breakdown spectroscopy," *Anal. Chem.*, vol. 85, pp. 640–669, 2013.

[12] S. Darwiche, M. Benmansour, N. Eliezer, and D. Morvan, "Laser-induced breakdown spectroscopy for photovoltaic silicon wafer analysis," *Prog. Photovolt Res. Appl.*, vol. 20, pp. 463–471, 2012.

[13] S. Grégoire, M. Boudinet, F. Pelascini, F. Surma, V. Detalle, and Y. Holl, "Laser-induced breakdown spectroscopy for polymer identification," *Anal. Bioanal. Chem.*, vol. 400, pp. 3331–3340, 2011.

[14] V. K. Singh and A. K. Rai, "Prospects for laser-induced breakdown spectroscopy for biomedical applications: A review," *Lasers Med. Sci.*, vol. 26, pp. 673–687, 2011.

[15] V. Motto-Ros, L. Sancey, X. C. Wang, Q. L. Ma, F. Lux, X. S. Bai, G. Panczer, O. Tillement, and J. Yu, "Mapping nanoparticles injected into a biological tissue using laser-induced breakdown spectroscopy," *Spectrochim. Acta - Part B At. Spectrosc.*, vol. 87, pp. 168–174, 2013.

[16] R. A. Multari, D. Cremers, J. A. M. Dupre, and J. E. Gustafson, "Detection of biological contaminants on foods and food surfaces using laser-induced breakdown spectroscopy (LIBS)," *J. Agric. Food Chem.*, vol. 61, pp. 8687–8694, 2013.

[17] V. K. Unnikrishnan, R. Nayak, S. Bhat, S. Mathew, V. B. Kartha, and C. Santhosh, "Biomedical applications of laser-induced breakdown spectroscopy (LIBS)," *Opt. Diagnostics Sens. XV Towar. Point-of-Care Diagnostics, Ed. by Gerard L. Coté, Proc. SPIE*, vol. 9332, p. 933211, 2015.

[18] A. Nevin, G. Spoto, and D. Anglos, "Laser spectroscopies for elemental and molecular analysis in art and archaeology," *Appl. Phys. A Mater. Sci. Process.*, vol. 106, pp. 339–361, 2012.

[19] R. Gaudiuso, M. Dell'Aglio, O. de Pascale, G. S. Senesi, and A. de Giacomo, "Laser induced breakdown spectroscopy for elemental analysis in environmental, cultural heritage and space applications: A review of methods and results," *Sensors*, vol. 10, pp. 7434–7468, 2010.

[20] M. Dell'Aglio, A. De Giacomo, R. Gaudiuso, O. D. Pascale, G. S. Senesi, and S. Longo, "Laser Induced Breakdown Spectroscopy applications to meteorites: Chemical analysis and composition profiles," *Geochim. Cosmochim. Acta*, vol. 74, pp. 7329–7339, 2010.

[21] A. De Giacomo, M. Dell'Aglio, O. De Pascale, S. Longo, and M. Capitelli, "Laser induced breakdown spectroscopy on meteorites," *Spectrochim. Acta - Part B At. Spectrosc.*, vol. 62, pp. 1606–1611, 2007.

[22] M. Rossi, M. Dell'Aglio, A. De Giacomo, R. Gaudiuso, G. S. Senesi, O. De Pascale, F. Capitelli, F. Nestola, and M. R. Ghiara, "Multi-methodological investigation of kunzite, hiddenite, alexandrite, elbaite and topaz, based on laser-induced breakdown spectroscopy and conventional analytical techniques for supporting mineralogical characterization," *Phys. Chem. Miner.*, vol. 41, pp. 127–140, 2014.

[23] J. Lasue, R. C. Wiens, T. F. Stepinski, O. Forni, S. M. Clegg, and S. Maurice, "Nonlinear mapping technique for data visualization and clustering assessment of LIBS data: application to ChemCam data," *Anal. Bioanal. Chem.*, vol. 400, pp. 3247–3260, 2011.

[24] N. L. Lanza, R. C. Wiens, S. M. Clegg, A. M. Ollila, S. D. Humphries, H. E. Newsom, and J. E. Barefield, "Calibrating the ChemCam laser-induced breakdown spectroscopy instrument for carbonate minerals on Mars," *Appl. Opt.*, vol. 49, pp. C211–C217, 2010.

[25] J. Sirven, B. Bousquet, L. Canioni, and L. Sarger, "Laser-Induced Breakdown Spectroscopy of Composite Samples : Comparison of Advanced Chemometrics Methods Laser-Induced Breakdown Spectroscopy of Composite Samples : Comparison of Advanced Chemometrics Methods," *Anal. Chem.*, vol. 78, pp. 1462–1469, 2006.

[26] F. Colao, R. Fantoni, P. Ortiz, M. A. Vazquez, J. M. Martin, R. Ortiz, and N. Idris, "Quarry identification of historical building materials by means of laser induced breakdown spectroscopy, X-ray fluorescence and chemometric analysis," *Spectrochim. Acta - Part B At. Spectrosc.*, vol. 65, pp. 688–694, 2010.

[27] S. M. Clegg, E. Sklute, M. D. Dyar, J. E. Barefield, and R. C. Wiens, "Multivariate analysis of remote laser-induced breakdown spectroscopy spectra using partial least squares, principal component analysis, and related techniques," *Spectrochim. Acta - Part B At. Spectrosc.*, vol. 64, pp. 79–88, 2009.

[28] N. B. Zorov, A. M. Popov, S. M. Zaytsev, and T. A. Labutin, "Qualitative and quantitative analysis of environmental samples by laser-induced breakdown spectrometry," *Russ. Chem. Rev.*, vol. 84, pp. 1021–1050, 2015.

[29] A. Jurado-Lopez and M. D. L. De Castro, "An atypical interlaboratory assay: Looking for an updated hallmark (-jewelry) method," *Anal. Bioanal. Chem.*, vol. 372, , pp. 109–114, 2002.

[30] L. Angeli, C. Arias, G. Cristoforetti, C. Fabbri, S. Legnaioli, V. Palleschi, G. Radi, A. Salvetti, and E. Tognoni, "Spectroscopic techniques applied to the study of Italian painted neolithic potteries," *Laser Chem.*, vol. 2006, pp. 1–7, 2006.

[31] M. Corsi, G. Cristoforetti, V. Palleschi, A. Salvetti, and E. Tognoni, "A fast and accurate

method for the determination of precious alloys caratage by Laser Induced Plasma Spectroscopy," *Eur. Phys. J. D*, vol. 377, pp. 373–377, 2001.

[32] D. A. Cremers and R. C. Chinni, "Laser-induced breakdown spectroscopy-capabilities and limitations," *Appl. Spectrosc. Rev.*, vol. 44, pp. 457–506, 2009.

[33] K. Meissner, T. Lippert, A. Wokaun, and D. Guenther, "Analysis of trace metals in comparison of laser-induced breakdown spectroscopy with la-icp-ms," *Thin Solid Films*, vol. 453–454, pp. 316–322, 2004.

[34] A. M. El Sherbini, T. M. El Sherbini, H. Hegazy, G. Cristoforetti, S. Legnaioli, V. Palleschi, L. Pardini, A. Salvetti, and E. Tognoni, "Evaluation of self-absorption coefficients of aluminum emission lines in laser-induced breakdown spectroscopy measurements," *Spectrochim. Acta - Part B At. Spectrosc.*, vol. 60, pp. 1573–1579, 2005.

[35] A. M. El Sherbini, T. El Sherbini, H. Hegazy, G. Cristoforetti, S. Legnaioli, L. Pardini, V. Palleschi, A. Salvetti, and E. Tognoni, "Measurement of the Stark broadening of atomic emission lines in non-optically thin plasmas by laser-induced breakdown spectroscopy," *Spectrosc. Lett.*, vol. 40, pp. 643–658, 2007.

[36] M. a. Ismail, H. Imam, A. Elhassan, W. T. Youniss, and M. a. Harith, "LIBS limit of detection and plasma parameters of some elements in two different metallic matrices," *J. Anal. At. Spectrom.*, vol. 19, p. 489, 2004.

[37] N. Reinhald, *Laser Induced Breakdown Spectroscopy - Fundamentals and Applicastions*, Springer. 2012.

[38] D. a. Cremers and L. J. Radziemski, *Handbook of Laser-Induced Breakdown Spectroscopy*, Ltd, John. 2006.

[39] A. De Giacomo, M. Dell'Aglio, R. Gaudiuso, S. Amoruso, and O. De Pascale, "Effects of the background environment on formation, evolution and emission spectra of laser-induced plasmas," *Spectrochim. Acta - Part B At. Spectrosc.*, vol. 78, pp. 1–19, 2012.

[40] S. I. Anisimov, B. L. Kapeliovich, and T. L. Perel-man, "Electron emission from metal surfaces exposed to ultrashort laser pulses," *J. Exp. Theor. Phys.*, vol. 66, pp. 375–377, 1974.

[41] J. Byskov-Nielsen, J.-M. Savolainen, M. S. Christensen, and P. Balling, "Ultra-short pulse laser ablation of copper, silver and tungsten: experimental data and two-temperature model simulations," *Appl. Phys. A*, vol. 103, pp. 447–453, 2011.

[42] D. Perez and L. Lewis, "Molecular-dynamics study of ablation of solids under femtosecond laser pulses," *Phys. Rev. B*, vol. 67, pp. 1–15, 2003.

[43] A. De Bonis, B. De Filippo, A. Galasso, A. Santagata, A. Smaldone, and R. Teghil, "Comparison of the performances of nanosecond and femtosecond Laser Induced Breakdown Spectroscopy for depth profiling of an artificially corroded bronze," *Appl. Surf. Sci.*, vol. 302, pp. 275–279, 2014.

[44] C. Momma, B. N. Chichkov, S. Nolte, F. von Alvensleben, A. Tünnermann, H. Welling, and B. Wellegehausen, "Short-pulse laser ablation of solid targets," *Opt. Commun.*, vol. 129, pp. 134–142, 1996.

[45] D. Bäuerle, *Laser Processing and Chemistry*, Springer-V. 2011.

[46] J. a. Aguilera, J. Bengoechea, and C. Aragón, "Spatial characterization of laser induced plasmas obtained in air and argon with different laser focusing distances," *Spectrochim. Acta Part B At. Spectrosc.*, vol. 59, pp. 461–469, 2004.

Chapter 2

Plasma analysis

2.1. Introduction

The physical – chemical study of plasma is considered the basis of LIBS measurement.
The characteristic parameters used for describing temporal and spatial evolution of a LIP are the electron number density and electron temperature, which can be calculated from the spectral information observed by collecting the plasma radiation.
The electron number density can be directly evaluated from the broadening of a spectral line [1].
The plasma temperature is usually estimated from the Boltzmann plot whose construction requires particles of the plasma to obey Maxwell – Boltzmann distribution.
The methods of determination of the electron density as well as the electron temperatures are presented in detail in the following paragraphs.

2.2. Thermodynamic equilibrium in the plasma

The descriptions of plasma properties is based on the study of the whole plume system, composed by atoms, molecules, electrons, ions and radiation.

For a full kinetic description, all processes occurring in the plasma have to take into account: ionization by collisions, photo – ionization, radiative and three – body recombination, collisional excitation/de – excitation processes, radiative decay, photo – excitation, and Bremsstrahlung phenomena [2].

Each plasma component can be fully described by various forms of energies with equations derived from statistical mechanics:

- Maxwell Energy Distribution for kinetic energy of electrons:

$$f_M = \left(\frac{m}{2\pi k_B T_e}\right)^{3/2} 4\pi v^2 e^{\left(-\frac{mv^2}{2k_B T_e}\right)}$$

(eq. 2.1.)

where v is the particle speed, m is the particle mass, k_B is the Boltzmann constant and T_e is the electron temperature.

- Boltzmann Distribution is used for describing the population of species (atoms/ions) in excited states:

$$N_n = N\frac{g_n e^{\left(-\frac{E_n}{k_B T_{exc}}\right)}}{Z(T)}$$

(eq. 2.2.)

where N is the number density of the species involved, N_n, g_n and E_n refer, respectively, to the population, the degeneracy and the energy of quantum level "n", k_B is the Boltzmann constant, T_{exc} and Z(T) are the excitation temperature and the partition function of the atomic level system at such temperature.

- The population of species at different ionization stages are described by the Saha equation, where N_I and N_{II} correspond, respectively, to neutral and singly ionized species:

$$\frac{n_e N_{II}}{N_I} = 2\frac{Z_{II}(T)}{Z_I(T)}\left(\frac{4\pi^2 m_e k_B T_H}{2\pi h^2}\right)^{\frac{3}{2}} e^{\left(-\frac{E-\Delta E}{k_B T_H}\right)}$$

(eq. 2.3.)

where n_e is the electron number density, k_B is the Boltzmann constant, h is the Planck constant, m_e is the mass of the electron, T_H is the temperature of atoms and ions, E is the first ionization energy for an isolated system and ΔE is the correction of this quantity for the interactions in the plasma.

- The photon energy is described by the Planck function, where the spectral energy density in vacuum (erg cm^{-3} Hz^{-1}) is given by:

$$W(\nu) = \frac{8\pi h\nu^3}{c^3}\left(e^{h\nu/k_B T_\upsilon} - 1\right)^{-1}$$

(eq. 2.4.)

where h is the Planck constant, c is the speed of light, k_B is the Boltzmann constant and T_v is the temperature describing the photon distribution.

If a plasma is in Thermodynamic Equilibrium (TE) condition, each process is balanced by its inverse process and this property is known as “the principle of detailed balancing” [2].
In this case, all equilibrium distributions are characterized by the same temperature [3]:

$$T_e = T_{exc} = T_H = T_\nu$$

(eq. 2.5.)

2.3. Local thermodynamic equilibrium (LTE)

A complete thermodynamic equilibrium is rarely satisfied in laser-induced plasmas because of their rapid temporal evolution, but it is possible to assume a new equilibrium, a Local Thermodynamic Equilibrium (LTE), that is reached after several nanoseconds from the plasma formation.

This condition is based on the idea that equilibrium occurs in small regions of space, although it may be somewhat different from region to region, and occurs when processes are dominated by collisions with electrons and the ionization degree is sufficiently high, so $T_{exc} \sim T_e$.

In other words, excitation and de-excitation rates between levels are dominated by inelastic collisions with electrons, rather than by radiative processes.

The radiative energy is decoupled from the other forms of energy, since radiative equilibrium requires the plasma to be optically thick at all frequencies.

Therefore the balances involving electrons, atoms and ions deviate from total equilibrium because of Planck function.

However, if the energy lost by radiation is negligible compared to other processes involving material species, the Saha – Boltzmann and Maxwell distributions can still be used to describe the system and a new equilibrium, a Local Thermodynamic Equilibrium, is established. In this case:

$$T_e = T_{exc} = T_H \neq T_v \qquad \text{(eq. 2.6.)}$$

This approximation is valid when the spatial and temporal gradients in the plasma are small enough and the plasma is called quasi-stationary and characterized by local values of temperature and electron density [3].

As will be explained in detail in the next chapter, the validity of LTE is important using the Calibration – Free (CF) LIBS procedure, that is a useful method to overcome matrix effects [4].

In the CF – LIBS procedure, the composition of the sample can be calculated only from the intensity of acquired signals, knowing the values of temperature and electron number density of the plasma. For this reason, if LTE condition is not respected, the accuracy of CF quantitative analysis is low.

If local thermodynamic equilibrium exists, temperature and electron density are two key parameters to characterize the plasma [5].

The principal technique for electron density determination is the broadening measurement of spectral lines.

Under normal LIBS conditions, the most important contributions to the line width are the Doppler width and the Stark effect, whereas the natural line width, related to energy level widths, can be neglected [6].

Using the McWhirter criterion and the two above discussed additional requirements, it is possible to check the existence of the LTE in laser-induced plasma [5].

2.4. Shape of emission lines

The shape of a spectral line is due to various broadening mechanisms [7], that may contribute in different way on the line broadening, in laser induced plasmas. Each mechanism has a particular influence on the spectral line and is explained in more detail in next paragraphs.

At high plasma density, as occurs in LIBS plasma, the principal mechanism of broadening is given by the Stark effect whereas the Doppler broadening and the Natural broadening (due to Heisenberg's uncertainty principle) are important at moderate plasma density.

This broadening along spectral line intensities can be useful to determine plasma density, as explained in section 2.5.

The shape can be approximated with a Voigt profile function, which is a convolution of Gaussian and Lorentzian profile functions.

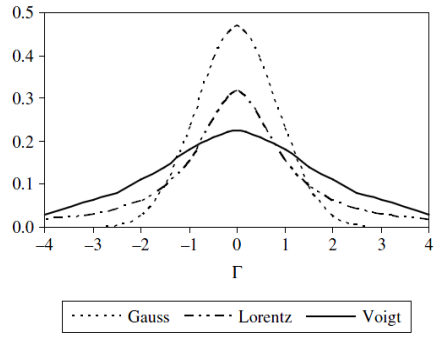

Fig. 2.1.: Gaussian and Lorentzian profile of equal half width.
The Voight profile is a convolution of other two [6]

The Voigt profile is the consequence of two main broadening mechanisms: Doppler effect and Stark effect.

2.4.1 Natural line broadening

This broadening is related to the lifetime of an excited state and the uncertainty of its energy. The effect results in a Lorentzian profile without shift with a line width of $\Delta\lambda_N$:

$$\Delta\lambda_N = 2\pi c/\left(\frac{1}{\Delta t_u} - \frac{1}{\Delta t_l}\right) \qquad \text{(eq. 2.7.)}$$

where Δt_u and Δt_l correspond, respectively, to the lifetimes of the upper and the lower states of a transition. In LIBS experiments, this broadening can be neglected.

2.4.2. Doppler broadening

This broadening is due to the Doppler effect caused by a distribution of velocity of atoms, ions or molecules.

In this case, the broadening has a Gaussian spectral profile and depends on the frequency of the spectral line, the mass of the emitting particles, and their temperature. The FWHM of the profile is given by:

$$\Delta\lambda_D = 7.16 \cdot 10^{14}\lambda\frac{T}{M}$$

(eq. 2.8.)

where T and M are the kinetic temperature and mass of emitters, and λ is the wavelength of the line.

In LIBS, Doppler broadening is not the main line broadening mechanism and is negligible compared to actual spectral line widths.

2.4.4. Instrumental broadening

Also instrumental factors can affect shape and width of spectral line.

The observed line shape is a convolution of the intrinsic line shape with the instrument function.

The instrumental line shape of a spectrometer is often approximately a Gaussian profile and, experimentally, can be determined by using a lamp with narrow spectral lines.

2.4.5. Stark broadening

In typical LIBS plasma, the main contribution to the width of the lines is given by Stark effect, which is caused by electric field that results primarily from collisions between electrons, with small contributions due to collisions with ions.

More in details, the Stark effect is responsible of shifting and perturbation of the levels of a species involved in a radiative transition, during its collision with electrons.

For this reason, there is a direct correlation between the electron density, n_e, and the FWHM of a Stark broadened line emission, $\Delta\lambda_{Stark}$, as shown in the following expression:

$$\Delta\lambda_{Stark} = 2w\left(\frac{n_e}{10^{16}}\right) + 3.5A\left(\frac{n_e}{10^{16}}\right)^{1/4}\left(1 - \frac{3}{4}\Lambda^{-1/3}\right)w\left(\frac{n_e}{10^{16}}\right)$$

(eq. 2.9.)

where:

- w is the electron impact parameter and is equal to 0.75 for a neutral line and 1.2 for an ionized one,
- A is the ion bombarding parameter,
- Λ is the number of particles estimated in the Debye sphere,
- n_e is the electron density.

The first term, on the right side of eq. 2.9. is the electron contribution to the broadening and the second term is the ion correction factor.
However, in typical LIBS conditions, for non-hydrogenic ions, Stark broadening is dominated by electron impact and thus the ion correction factor can be neglected for most atomic lines.
As a consequence the Stark broadening equation can be transformed in the following form:

$$\Delta\lambda_{\mathrm{Stark}} = \left[2\mathrm{w}\left(\frac{\mathrm{n_e}}{10^{16}}\right)\right]$$

(eq. 2.10.)

The Stark effect leads to symmetric Lorentz profiles and is usually appreciable for dense plasmas with $n_e \geq 10^{15}$ cm^{-3} emitting lines from only neutral and singled ionized species, whereas, for multiple ionized atoms Doppler effect tends to override Stark broadening.
To measure the electron density of the plasma, usually the Stark broadening method is used.

2.5. Electron density : McWhirter Criterion

A simple experimental method to check LTE assumption is the McWhirter criterion [2][5], which defines the minimum electron number density in the plasma in order to have that collisional depopulation rates for all electronic levels of the atom are more

larger than the radiative depopulation rate. In this way, it is established that collisional processes prevail over radiative processes and deviations from LTE are negligible.

For homogenous and stationary plasma, the McWhirter criterion is:

$$n_e \geq 1.6 \cdot 10^{12}\, T_e^{1/2} (\Delta E)^3$$

(eq. 2.11.)

where n_e is electron density, T_e is electron temperature, and ΔE is the gap of adjacent levels and usually corresponds to the energy differences between the ground state and the first excited state of an atom (or an ion).

However, the McWhirter criterion is a necessary but not sufficient condition for LTE, because it is derived for approximation of homogenous and stationary plasmas.

Because laser-induced plasma is transient and inhomogeneous, in order to obtain LTE assumption, two other conditions should be verified.

First of all, the temporal variation of thermodynamic parameters should be small during the time needed to establish equilibrium [2].

Second condition refers to the variation length of temperature and electron number density in the plasma. i.e. it should be larger than the distance travelled by a particle by diffusion during the time of relaxation to equilibrium.

In other word, the relaxation time $\lambda(\tau_{rel})$ of a plasma for the establishment of the thermodynamic equilibrium must be shorter than the time of variation of thermodynamic parameters of the plasma, such as the temperature or the electron density. These criteria can be expresses as [3]:

$$\lambda(\tau_{rel}) \ll \frac{n_e}{dn_e/dx}$$

(eq. 2.12.)

$$\lambda(\tau_{rel}) \ll \frac{T_e}{dnT_e/dx}$$

(eq. 2.13.)

where $\lambda = (D \cdot \tau_{rel})^{1/2}$ is the diffusion length during the relaxation time τ_{rel}.

If these conditions are not fulfilled, individual values of temperature and electron number density cannot be determined but various values of such parameters in a different region of the plasma should be considered [8].

These two conditions are more difficult to test experimentally, since they require information about the temporal evolution and the spatial distribution of those parameters [9].

For this reason, generally, the McWhirter criterion is the only one reported in the majority of papers in literature [10], [11].

2.6. Determination of the electron density: Stark broadening

In typical LIBS conditions, the line broadening is mainly due to Stark broadening (with Lorentzian profile) and instrumental broadening (with Gaussian profile).

From calculation of these two contributes, therefore, it is possible to determine the value of the electron density in the plasma.

The procedure is to choose a line profile and to fit the experimental spectral lines with a Voigt profile, that is a convolution of a Lorentzian and a Guassian profile.

Considering that, at long delay time, the Stark broadening becomes particularly negligible, because of the low electron density, the spectral lines can be fitted by Guassian function and the corresponding Stark broadening can be obtained by subtraction by the FWHM obtained with Voight profile.

The electron density is then determined by eq. 3.7., knowing the needed spectral broadening parameters [12].

2.7. Electron temperatures

For temperature calculations, the plasma has to be assumed in LTE condition. As said previously, with transient plasma, LTE is allowed if the collision time between particles

is low and excitation/de-excitations trough electrons collision are the major processes of plasma [13].

Therefore, sufficiently large electron densities and temperatures are required for LTE. Under the assumption of LTE, it can be assumed that processes are balanced and only radiation process is out of equilibrium: excitation by collisions with electrons is equal to the de – excitation process and collisional ionization is equal to three – body collisional recombination.

The temperature, which can be considered as one of the most important parameters characterizing the plasma, can be determined by emission spectroscopy.

According to the McWhirter criterion, with high electron density, plasma is generally assumes in LTE.

However, the complex processes in LIP and its transient characteristic, can lead out of equilibrium condition.

Anyway, in intermediary delay time, when the plasma is hot enough, the LTE condition is satisfied and the electron temperature can be measured using Boltzmann equation or Saha equation.

Among the various methods for temperature estimation, relative line intensity measurement is the most used technique in LIP.

If LTE exists, for each part of the plasma plume it is possible to find a temperature that satisfies the Boltzmann, Saha and Maxwell distributions.

2.8. Determination of the electron temperature

2.8.1. Boltzmann plot

In LTE, it is assumed that all the material particles present in the plume (i.e. ions, atoms and electrons) are in locally and instantaneously balance, therefore the excitation temperature should hold same value for all of them.

Taking into account this approximation, the population of atoms or ions, in different energy levels, is given by the Boltzmann distribution:

$$\frac{n_u^Z}{n^Z} = \frac{g_u^Z}{U^Z(T)} e^{\left(-\frac{E_u^Z}{k_B T}\right)}$$

(eq. 2.14.)

where Z corresponds to the ionization stage of the species (0 for neutral and 1 for singly ionized atoms), n_u^Z, E_u^Z and g_u^Z are the population, energy and degeneracy of the upper energy level "u" respectively, n^Z is the number density of the atom or the ion and $U^Z(T)$ is the partition function of the species in ionization stage Z at temperature T.
The intensity I^Z_{ul} of an emission line due to the transition between the upper energy level "u" and the lower energy level "l" of a species is given by:

$$I_{ul}^Z = \frac{hcA_{ul}^Z n_u^Z}{4\pi\lambda_{ul}^Z}$$

(eq. 2.15.)

where h is the Plank Constant, c is the speed of light, A_{ul}^Z and λ_{ul}^Z are the Einstein coefficient and the transition line wavelength for "u-l" transition.
Replacing n_u^Z with equation 2.15., the equation of intensity becomes:

$$I_{ul}^Z = \frac{hc}{4\pi\lambda_{ul}^Z} A_{ul}^Z \frac{n^Z g_u^Z}{U^Z(T)} e^{\left(-\frac{E_u^Z}{k_B T}\right)}$$

(eq. 2.16.)

The electron temperature can be calculate measuring the relative intensities and choosing lines for which the g, A and E values are known.
The equation can be rearranged into natural logarithm form:

$$\ln\left(\frac{I_{ul}^Z \lambda_{ul}^Z}{g_u^Z A_{ul}^Z}\right) = \ln\left(\frac{hcn_Z}{4\pi U^Z(T)}\right) - \frac{1}{k_B T} E_u^Z$$

(eq. 2.17.)

Since relative intensities are not easy to measure precisely, a way to achieve more accurate temperature estimation is to use simultaneously several emission lines with very different energy values.

The Boltzmann plot is performed plotting the intensity of the observed transition as a function the energy of the its upper level.

The value of electron temperature is deduced from the slope of the plot line, utilizing linear regression, which have the form $-1/k_BT$.

The Boltzmann plot technique is the most straightforward method to determine the temperature, but several deviations from this simplified approach are usually observed in LIBS experiments.

The most common is that the excitation temperature of atomic species usually has a lower value than corresponding temperature estimated with ions because of radiative recombination phenomena, which can cause an underestimation of number of atoms.

Also, spatial and temporal gradient of temperature, especially in the peripheral zones of the plasma, can be established, caused by interaction between the ablated species and background atmosphere at the contact with the shockwave produced by its supersonic expansion.

Furthermore, some experimental difficulties can bring about further inaccuracies.

2.8.2. Saha plot

For plasma in LTE approximation, the excitation temperature is the same as the ionization temperature.

Since in LIP, emission lines from different ionization stages are usually present in, a combination of the Saha ionization and Boltzmann excitation distributions can be used to measure the electron temperature.

The Saha (also know Saha – Eggert) method can be used in order to increase the reliability on temperature calculation.

Considering neutral and singly ionized species of the same element, the Saha equation is given by ratio between ionized and atomic species, described, respectively, as superscripts II and I:

$$n_e \frac{n^{II}}{n^I} \frac{2\pi m_e k_B T^{3/2}}{h^3} \frac{2Z^{II}}{Z^I} e^{\left(-\frac{E_{ion}}{k_B T}\right)}$$

(eq. 2.18.)

where n_e is the plasma electron density, n^I and n^{II} are the number densities of the neutral atomic species and the singly ionized species respectively, E_{ion} is the first ionization potential, h is the Planck constant and m_e is the electron mass.
Considering the ratio between ionic and atomic emission intensities:

$$\frac{I_{ij}^{II}}{I_{mn}^{I}} = \left(\frac{A_{ul}^{II} g_u^{II} \lambda_{mn}^{I}}{A_{mn}^{I} g_n^{I} \lambda_{ul}^{II}}\right) \left(\frac{2(2\pi m_e k_B T)^{3/2}}{n_e h^3}\right) e^{-\left(\frac{E_{ion} - \Delta E_{ion} + E_j^{II} - E_n^{II}}{k_B T}\right)}$$

(eq. 2.19.)

In this equation λ_{ul} and λ_{mn} are two lines of the same species, E_u and E_n are the different values of the upper level energy, respectively, and ΔE_{ion} is a correction parameter due to the fact that in a plasma the presence of charged particles lowers the ionization potential.
Applying natural logarithm, the eq. 2.19. becomes:

$$\ln\left(\frac{I_{ij}^{II} A_{mn}^{I} g_n^{I} \lambda_{ij}^{II}}{I_{mn}^{I} A_{ij}^{II} g_j^{II} \lambda_{mn}^{I}}\right) = \ln\left(\frac{2(2\pi m_e k_B T)^{3/2}}{n_e h^3}\right) - \left(\frac{E_{ion} - \Delta E_{ion} + E_j^{II} - E_n^{II}}{k_B T}\right)$$

(eq. 2.20.)

This logarithmic ratio results in a plot whose line slope depends on the electron temperature.

The estimation of the temperature based on the Saha equation is more complicated, but also more precise.

In this case, a higher difference of upper energy states is obtained, therefore, the slope is less sensitive to the measurement noise.

Moreover, the electron density can be obtained from the intercept:

$$n_e = \left(\frac{2(2\pi m_e kT)^{3/2}}{h^3}\right)\left(\frac{I_{ij}^{I} A_{mn}^{II} g_m^{II}}{I_{mn}^{II} A_{ij}^{I} g_i^{I}}\right) e^{-\frac{(E_{ion}-\Delta E_{ion}+E_m^{II}-E_i^{I})}{kT_e}}$$

(eq. 2.21.)

2.9. References

[1] J. A. Merten, B. W. Smith, and N. Omenetto, "Local thermodynamic equilibrium considerations in powerchip laser-induced plasmas," *Spectrochim. Acta - Part B At. Spectrosc.*, vol. 83–84, pp. 50–55, 2013.

[2] G. Cristoforetti, A. De Giacomo, M. Dell'Aglio, S. Legnaioli, E. Tognoni, V. Palleschi, and N. Omenetto, "Local Thermodynamic Equilibrium in Laser-Induced Breakdown Spectroscopy: Beyond the McWhirter criterion," *Spectrochim. Acta - Part B At. Spectrosc.*, vol. 65, pp. 86–95, 2010.

[3] G. Cristoforetti, E. Tognoni, and L. A. Gizzi, "Thermodynamic equilibrium states in laser-induced plasmas: From the general case to laser-induced breakdown spectroscopy plasmas," *Spectrochim. Acta - Part B At. Spectrosc.*, vol. 90, pp. 1–22, 2013.

[4] E. Tognoni, G. Cristoforetti, S. Legnaioli, and V. Palleschi, "Calibration-Free Laser-Induced Breakdown Spectroscopy: State of the art," *Spectrochim. Acta - Part B At. Spectrosc.*, vol. 65, pp. 1–14, 2010.

[5] C. Aragón and J. A. Aguilera, "Characterization of laser induced plasmas by optical emission spectroscopy: A review of experiments and methods," *Spectrochim. Acta - Part B At. Spectrosc.*, vol. 63, pp. 893–916, 2008.

[6] D. a. Cremers and L. J. Radziemski, *Handbook of Laser-Induced Breakdown Spectroscopy*, Ltd, John. 2006.

[7] N. Konjević, "Plasma broadening and shifting of non-hydrogenic spectral lines: present status and applications," *Phys. Rep.*, vol. 316, pp. 339–401, 1999.

[8] H. R. Griem, "Validity of local thermal equilibrium in plasma spectroscopy," *Phys. Rev.*, vol. 131, pp. 1170–1176, 1963.

[9] H. W. Drawin, "Validity conditions for local thermodynamic equilibrium," *Z.Physik*, vol. 228, pp. 99–119, 1969.

[10] A. De Bonis, A. Santagata, A. Galasso, M. Sansone, and R. Teghil, "Applied Surface Science Femtosecond laser ablation of CaF2: Plasma characterization and thin films deposition," *Appl. Surf. Sci.*, vol. 302, pp. 145–148, 2014.

[11] A. Santagata, R. Teghil, A. De Giacomo, M. Dell'Aglio, G. P. Parisi, A. De Bonis, and A. Galasso, "Optical emission spectroscopy investigation of an ultra-short laser induced titanium plasma reheated by a ns laser pulse," *Appl. Surf. Sci.*, vol. 253, pp. 7792–7797, 2007.

[12] N. Konjević, M. Ivković, and S. Jovićević, “Spectroscopic diagnostics of laser-induced plasmas,” *Spectrochim. Acta - Part B At. Spectrosc.*, vol. 65, pp. 593–602, 2010.

[13] N. Omenetto and D. W. Hahn, “Laser-Induced Breakdown Spectroscopy (LIBS), Part I: Review of Basic Diagnostics and Plasma – Particle Interactions: Still-Challenging Issues Within the Analytical Plasma Community,” vol. 64, pp. 335–366, 2010.

Chapter 3

LIBS quantitative analysis

3.1. Introduction

Although LIBS allows simple and rapid qualitative determinations, the quantitative analysis is one of the limitations of the LIBS technique and may be considered its Achille's heel [1], [2].

The intensity of signals can be directly correlated to sample composition because there is a linear dependence with the amount of emitting particles in the plasma plume.

The main limitations are the matrix effect and the low repeatability of the measurements due to small shot-to-shot signal fluctuations that may arise from the instability of the laser energy or inhomogeneity of the sample.

Moreover, the diversity of LIBS instrumentation makes the quantitative intra-comparison and reproducibility of the measurements among different LIBS groups complicate.

As previously said, the validation of LTE condition provides the basis of quantitative LIBS analysis. However, it is necessary that other assumptions must be fulfilled.

First of all, laser ablation has to be stoichiometric, i.e. the composition of the plasma plume reflects the material composition.

Secondly, the plasma should preferably be optically thin, or at least self absorption can be neglected for lines chosen for analysis.

A disadvantage of LIBS technique is that differences in sample composition result in strong differences in laser – matter interaction and, in consequence, in variations of radiation absorption, reflection and thermal conductivity.

The sample matrix strongly influences the parameters of the plasma which, in turn, influence the sensitivity for each element [3]–[5].

In LIBS literature various methods for obtaining quantitative information are present [6]–[8].

3.2. Stoichiometric ablation

The stoichiometric ablation refers to the composition of the plasma that should reflects the composition of the sample under study in order to obtain a plasma that is representative of the target composition.

However, because of the different volatilities of elements and their compounds, the composition of the plasma can be not perfectly stoichiometric.

Therefore, for minimizing selective vaporization, it is necessary that the laser fluence is much larger than the latent heat of vaporization for all of the constituents, in order to obtain that all constituents can be completely vaporized and removed.

In LIBS measurements, utilizing short or ultra-short high energy laser beam, the target is exposed to the fluence of up to 10^9 Wcm^{-2} and it has been found that consequent laser ablation is stoichiometric.

3.3. Optically thin plasma

During LIBS experiments, the plasma temperature may present inhomogeneous distributions between the external zones and the plasma core, and, if radiation passes through this temperature gradient, it can be emitted and successively reabsorbed.

In this case, the plasma created by laser ablation is defined optically thick. For evaluation of physical parameters [9], [10], optically thin plasma condition has to be

considered that assumes that all the emitted plasma radiation is not re-absorbed by the plasma itself.

If this condition is not fulfilled, the emitted photons are absorbed within the plasma and the self-absorption effect takes place, leading to a shape distortion of emission lines.

When Stark broadening method is used for the determination of electron density, this line distortion due to self-absorption leads to an overestimation whereas, including self-absorbed line in Boltzmann plot, the erroneous measurement of intensity leads to erroneous estimation of the slope that, consequently, affects the accuracies of temperature.

Therefore, it is important to respect the optically thin plasma condition to improve the reliability and precision of analysis.

The self-absorption occurs mainly in the earlier stages of a LIP evolution when the density of LIP is higher.

3.3.1. Self – absorption

Using LIBS, as for the other spectroscopic techniques, the chemical composition of the analyzed materials is obtained by measuring the intensity of emission lines.

For this reason, it is important detect and quantify the presence of nonlinear effects due to a complex mechanisms between atoms, ions and radiation [11].

As state above, the self – absorption process is most likely with very high dense plasma and causes a distortion in the line profile, resulting in broadened line or presence of a dip in the central part of the spectral line.

This effect is referred to self – reversal and results in a pronounced non – linearity at increasing concentration.

Usually most intense self – absorption occurs for resonant lines associated to ground state but may also occur for weaker and non – resonant lines of elements present at concentrations greater than, approximately, 5%.

The self – absorbed lines have measured intensities lower than expected, simulating a lower concentration of the element.

From an analytical point of view is more complicated obtaining a correct calibration curve, obtained by plotting the spectral intensity versus concentration, because there is a deviation from linearity at increasing concentrations.

However it is very difficult to evaluate the amount of self-absorption from the observed shape of a line.

In order to avoid this effect, the non-resonant lines should be used.

First of all, it is important to choose the more appropriate lines, excluding saturated lines, and optically thin plasma condition, because the self-absorption is less intense for thin plasmas where the optical path of radiation is shorter.

However, the choose of non saturated lines, which have low probability transition, minimizes self – absorption, but has the disadvantage that may result in low intensity signals.

It is therefore important to be able to get a criterion for discriminating and possibly correcting the phenomenon of self – absorption [12].

For the study of this effect, the curve of growth – COG method can be applied, using as input parameters plasma temperature, electron density, Lorentzian and Gaussian half widths and the optical path length [13].

Another experimental method to evaluate the effect of self – absorption is the duplicating mirror method, used by Moon et al.[14], in which an external spherical mirror is placed behind the plasma at twice the value of its focal length.

In this way the original plasma image must be overlapped with the image coming from the mirror and two line profile are obtained: with and without the mirror.

This method allows to evaluate a self – absorption coefficient from difference between intensity of original plasma and duplicate plasma.

Experimentally this approach presents some difficulties because of need to have a flat and regular sample surface.

The correction factor $K_{\lambda,corr}$, obtained experimentally can then be applied to retrieve the exact line profile and, consequently, to improve the linearity of calibration curves.

3.4. Limit of detection

From an analytical point of view, the limits of detections (LOD) of a system represents the lowest concentration at which it is possible declare that a given element is present or not in the analyzed sample because it is possible distinguish between the signal and the background. Limit of detection is given as:

$$\mathrm{LOD} = \mathrm{K}\frac{\sigma}{\mathrm{S}}$$

(eq. 3.1.)

where σ is the standard deviation of the background signal in the blank sample (where the analyte is not present), S is the slope of the linear calibration curve and K corresponds to the numerical factor that expresses the confidence level required for analysis, and usually, is equal to 3 for 99.86% confidence level.

On the other hand, limit of quantification (LOQ) is referred to the lowest elemental concentration which can be measured by a given apparatus with acceptable precision and reproducibility [15]. It is given by:

$$\mathrm{LOQ} = 3.3\mathrm{LOD} = 3.3\left(3\frac{\sigma}{\mathrm{S}}\right)$$

(eq. 3.2.)

The sensitivity of the measurements can be deduced from the slope of the calibration curve because linearity means that as the amount of an element increases, the related intensity also enhances.

On the other hand, the calibration curve loses its sensitivity if the signals intensity decreases with the increasing of the amount of the analyte.

Finally, the calibration curve may appear flat due to the saturation of signal intensities.

It is therefore crucial to choose carefully spectral lines for the calibration process, in order to obtain reliable data.

For example, spectral resonant lines easily show saturation effect (self absorption effect), also for low concentrations, therefore they should not be used for the calibration curve formation, but they are useful for trace element analysis because of their higher sensitivity.

Moreover, for the quantification process another phenomenon that has to be taken into account is the matrix effect, according to which, ablating two samples with different matrices, the same amount of analyte can results in significantly different signal intensities.

There are many ways how to compensate or to avoid the matrix effect, which are explained in the following section.

3.5. Calibration Curve method

As for other analytical techniques, the most common approach to quantitative LIBS analysis is calibration curve method.

This method is based on the use of calibration curves constructed plotting the intensity of the elemental line as a function of the concentration of a corresponding element in standard samples with known concentrations [16].

As said previously, because the laser – material interaction depends on the matrix, the differences between the sample matrix and the reference standard should be low, i.e. the compositions of these standard have to be similar to those of the sample under study.

The linear or polynomial function of calibration curve correlates directly the line intensity of the unknown sample with the concentration of the corresponding element.

The obtained function should pass from the origin, i.e. the zero concentration of the analyte should corresponds to the absence of signal from the sample, but experimentally, sometimes this is not the case, either of intrinsic systemic errors of the technique, or for particular experimental conditions, for example presence of interfering lines.

The quality of the calibration function may differ considerably. In fact, at low analytical concentrations, a linear relationship is usually obtained, whereas at higher concentrations, due to the higher probability of the self – absorption phenomenon, a deviation from linearity is observed.

Moreover, to build a good calibration curve, the emission lines have to be chosen on the basis of the expected concentration of the element: for low concentrations it would be desirable to choose resonance lines, which are more intense spectral lines, whereas for high concentrations it is preferable to take into account weaker lines, in order to avoid the known effects of self – absorption.

In any case, the choice of the lines analyzed must be made taking into account the concentration range considered and the possible presence of interferences due to the components of the matrix.

Concentrations are usually expressed as weight percentage $\%w_{analyte}$.

3.5.1. The matrix effect

The composition of the sample has to be taken into account in the laser-matter interaction and consecutive LIP formation and emission, due to matrix effect that affects the properties of plasma [17].

In order to compensate this effect, the normalization procedure can be used.

In this approach the selected elemental line of an analyte is normalized to the intensity of the element line of a known composition sample, defines as internal standard.

The internal standard can be either an element already present or specially added in all samples (with known concentrations) or one major component whose concentration is approximately constant in all the samples to be analyzed.

In this way, the analyte signals should have unified signal in all different samples.

Individual calibration curves should be created for each groups of samples to partially avoid the matrix effect.

This approach needs matrix-match samples as standard prior to the analysis of unknown samples.

With calibration-free method [7], [18], [19], the measurement of the standardized samples, prior to the quantitative analysis, are not require because each measurement is self – consistent by applying plasma parameters (temperature and electron density) to the spectral data.

The following paragraphs are dedicated to a description of the most common approaches to the LIBS quantitative analysis.

3.6. Calibration – Free method (CF – LIBS)

To overcome the matrix effect, the Calibration – Free LIBS procedure has been proposed by Ciucci et al. [20], allowing determination of the concentration without calibration curve [21].

The Calibration – Free (CF) LIBS has been applied to various materials and especially in analysis of metals, providing reliable quantitative analyses both for major and minor elements [18], [22].

With respect to analytical methods based on calibration methods, the main advantage of this approach is that matrix – matched reference standards, which in the case of complex materials may be difficult or impossible to obtain, are not required.

On the contrary, an important disadvantage is the high experimental uncertainty, which makes the quantitative determination of trace elements very critical or impossible [19].

CF methods is based on accurate determination of the plasma temperature, that is usually obtained with the Boltzmann plot method. For this reason, the departure of the plasma from LTE or optical thickness of the plasma may affect the accuracy of the quantitative analysis. Under the assumption described above, the integrated intensity of a spectral line can be directly correlated with the concentration of an element.

The weight percentage for each element is determined using the set of equations reported below:

$$N_{0,at} = \frac{I_{ul} Z_{at}}{g_u A_{ul} h\nu_{ul}} e^{\left(\frac{E_u}{kT}\right)}$$

(eq. 3.3.)

$$N_{0,ion} = 2\frac{N_{at} Z_{ion}}{N_e Z_{at}} \left(\frac{2\pi m_e kT}{h^2}\right)^{3/2} e^{\left(-\frac{E_I}{kT}\right)}$$

(eq. 3.4.)

$$N_{0,i} = N_{0,at} + N_{0,ion}$$

(eq. 3.5.)

$$wt\%_i = \frac{N_{0,i} M_i}{\Sigma_i N_{0,i} M_i}$$

(eq. 3.6.)

where: $N_{0,at}$ and $N_{0,ion}$ are the relative number densities of atoms and ions of a given element, I_{ul} is the emission intensity of a given transition from the upper level "u" to the lower level "l", g_u, A_{ul}, ν_{ul} and E_u are, respectively, the degeneracy of the upper level, the Einstein coefficient of spontaneous emission for the "ul" transition, the emitted photon frequency and the energy of the upper level.

Z_{at} and Z_{ion} are the atomic and ionic partition functions, N_e is the electron density, E_I is the energy of first ionization and M_i is the molar mass of species "i".

Therefore, especially for CF LIBS procedures, it is necessary to find an experimental method to evaluate the self absorption effect in order to avoid underestimating the element abundance.

3.6.1. Factors affecting the performance of CF – LIBS

The departure of plasma state from the three assumptions, above mentioned, can influence the performance of CF procedure.

Firstly, non stoichiometric ablation or incomplete atomization decrease the accuracy of the analytical results because they are extracted directly from the emission spectra of the plasma.

This situation is different with calibration curve method because, in this case, the fractionation effects are compensated by using matrix-matched standard samples.

However, for metallic system, the probability to obtain non stoichiometric ablation is very low due to prevalence of photothermal ablation processes.

Moreover, the departure from LTE condition is particularly important for CF LIBS, since the Boltzmann plot or the Saha plot are used for the determination of the concentrations.

If LTE is not validated, the CF method will provide unreliable results.

3.7. Inverse Calibration – Free LIBS

The accuracy of plasma temperature determination can be affected by several factors, first of all, by deviations from the Local Thermodynamic Equilibrium (LTE) condition but also self – absorption and plasma inhomogeneity.

Moreover, for a satisfactory accuracy, the Boltzmann plot method requires that the selected emission lines have transitions from upper excited levels with energy range as wide as possible.

Sometimes this procedure is impracticable or impossible, i.e. when only few observable transitions are adequate for a given element for drawing Boltzmann plot because of spectral interferences, low concentration, characteristics of spectroscopic constants or the energy values. Furthermore, this procedure is impracticable when many successive acquisitions must be avoided in order to preserved the integrity of the sample or to obtain fast analysis.

Moreover, in literature [23] , for copper based samples, it has been observed that the excitation temperatures of Cu I, Pb I, Ni I and Sn I, determined by the use of Boltzmann plots can be strongly different one to each other, indeed all different plots have been showed, individually, acceptable linearity but different slopes.

In particular, Cu temperature results higher, while Pb and Ni ones are considerably lower.

Therefore none of the temperatures obtained have an actual physical meaning and could be assumed as the real excitation temperature of the plasma.

Probably this result depends on whether Boltzmann plot could be a too simplified approach to determine the plasma temperature, when a multi-elemental targets are analyzed.

For all these reasons, alternative method has been introduced to overcome possible inaccuracies due to the excitation temperature measured by the Boltzmann plot [24].

This alternative method for plasma temperature determination consists in a simple empirical approach in which the classical Calibration – Free procedure is inverted.

For this reason, this new methodology is referred to as “inverse method” and requires the use of only one certified standard to obtain temperature, in contrast to what normally done in CC and CF LIBS [23].

The proposed method relies, anyway, on the same conditions of analytical CF – LIBS (LTE condition, stoichiometric ablation and plasma homogeneity) but, introduces a new practical assumption: if different samples with similar matrices are ablated in the same conditions, the excitation temperature of the produced plasmas is the same.

This allows to apply the temperature value, obtained with this procedure, to unknown targets with similar matrix, that are ablated in the same conditions as the standard.

The main difference from other method is that in the inverse calibration free the plasma is considered as a unitary system and the obtained temperature can be considered really representative of the energy distribution of all the species in the plasma phase.

The inverse method consists in applying the same equation of CF – LIBS (eq. 3.3. – 3.6.) and using the know elemental composition of the target as a starting parameter.

Inverse Calibration Free LIBS method can provide an indirect evaluation of the plasma temperature which, on the contrary of Boltzmann plots, that are employed for the CF approach, is not affected from either the limited interval of energy of the upper states of the electronically excited species or the occurrence of their excitation temperature mismatch.

In order to retrieve the plasma temperature, the calculation is repeated at different hypothetical excitation temperatures, within a plausible range, obtaining a set of weight percentages for the investigated species at every temperature.

In this way, the actual plasma temperature is assumed as the one that minimizes the discrepancy between the determined concentrations and the certified ones.

The inverse method allows to improve precision in the temperature determination and, also, only one standard is required for the analysis, that does not have to be necessarily perfectly matrix-matched and to contain concentrations similar to those of the actual samples.

3.8. References

[1] D. W. Hahn and N. Omenetto, "Laser-induced breakdown spectroscopy (LIBS), part II: Review of instrumental and methodological approaches to material analysis and applications to different fields," *Appl. Spectrosc.*, vol. 66, pp. 347–419, 2012.

[2] V. Palleschi and I. Schechter, "Laser-Induced Breakdown Spectroscopy (LIBS): Fundamentals and Applications," *Cambridge Univ. Press*, p. 16, 2006.

[3] D. A. Cremers and R. C. Chinni, "Laser-induced breakdown spectroscopy-capabilities and limitations," *Appl. Spectrosc. Rev.*, vol. 44, pp. 457–506, 2009.

[4] D. a. Cremers and L. J. Radziemski, *Handbook of Laser-Induced Breakdown Spectroscopy*, Ltd, John. 2006.

[5] F. J. Fortes, J. Moros, P. Lucena, L. M. Cabalín, and J. J. Laserna, "Laser-induced breakdown spectroscopy," *Anal. Chem.*, vol. 85, pp. 640–669, 2013.

[6] F. Colao, R. Fantoni, V. Lazic, and V. Spizzichino, "Laser-induced breakdown spectroscopy for semi-quantitative and quantitative analyses of artworks—application on multi-layered ceramics and copper based alloys," *Spectrochim. Acta Part B At. Spectrosc.*, vol. 57, pp. 1219–1234, 2002.

[7] M. Achouri, T. Baba-Hamed, S. A. Beldjilali, and A. Belasri, "Determination of a brass alloy concentration composition using calibration-free laser-induced breakdown spectroscopy," *Plasma Phys. Reports*, vol. 41, pp. 758–768, 2015.

[8] V. Lazic, R. Fantoni, F. Colao, A. Santagata, A. Morone, and V. Spizzichino, "Quantitative laser induced breakdown spectroscopy analysis of ancient marbles and corrections for the variability of plasma parameters and of ablation rate," *J. Anal. At. Spectrom.*, vol. 19, pp. 429–436, 2004.

[9] C. Aragón and J. A. Aguilera, "Characterization of laser induced plasmas by optical emission spectroscopy: A review of experiments and methods," *Spectrochim. Acta - Part B At. Spectrosc.*, vol. 63, pp. 893–916, 2008.

[10] A. De Giacomo, M. Dell'Aglio, R. Gaudiuso, A. Santagata, G. S. Senesi, M. Rossi, M. R. Ghiara, F. Capitelli, and O. De Pascale, "A Laser Induced Breakdown Spectroscopy application based on Local Thermodynamic Equilibrium assumption for the elemental analysis of alexandrite gemstone and copper-based alloys," *Chem. Phys.*, vol. 398, pp. 233–238, 2012.

[11] A. Santagata, A. De Bonis, P. Villani, R. Teghil, and G. P. Parisi, "Fs/ns-dual-pulse

orthogonal geometry plasma plume reheating for copper-based-alloys analysis," *Appl. Surf. Sci.*, vol. 252, SPEC. ISS., pp. 4685–4690, 2006.

[12] D. Bulajic, M. Corsi, G. Cristoforetti, S. Legnaioli, V. Palleschi, A. Salvetti, and E. Tognoni, "A procedure for correcting self-absorption in calibration free-laser induced breakdown spectroscopy," *Spectrochim. Acta - Part B At. Spectrosc.*, vol. 57, pp. 339–353, 2002.

[13] I. B. Gornushkin, J. Anzano, L. A. King, B. W. Smith, N. Omenetto, and J. D. Winefordner, "Curve of growth methodology applied to laser-induced plasma emission spectroscopy," *Spectrochim. Acta Part B*, vol. 54, pp. 491–503, 1999.

[14] H. Y. Moon, K. K. Herrera, N. Omenetto, B. W. Smith, and J. D. Winefordner, "On the usefulness of a duplicating mirror to evaluate self-absorption effects in laser induced breakdown spectroscopy," *Spectrochim. Acta - Part B At. Spectrosc.*, vol. 64, pp. 702–713, 2009.

[15] V. Thomsen, D. Schatzlein, and D. Mercuro, "Limits of Detection in Spectroscopy," *Pure Appl. Chem.*, vol. 18, pp. 112–114, 2003.

[16] A. De Giacomo, M. Dell'Aglio, O. De Pascale, R. Gaudiuso, A. Santagata, and R. Teghil, "Laser Induced Breakdown Spectroscopy methodology for the analysis of copper-based-alloys used in ancient artworks," *Spectrochim. Acta - Part B At. Spectrosc.*, vol. 63, pp. 585–590, 2008.

[17] R. Fantoni, L. Caneve, F. Colao, L. Fornarini, V. Lazic, and V. Spizzichino, "Methodologies for laboratory Laser Induced Breakdown Spectroscopy semi-quantitative and quantitative analysis — A review," *Spectrochim. Acta Part B At. Spectrosc.*, vol. 63, pp. 1097–1108, 2008.

[18] E. Tognoni, G. Cristoforetti, S. Legnaioli, and V. Palleschi, "Calibration-Free Laser-Induced Breakdown Spectroscopy: State of the art," *Spectrochim. Acta - Part B At. Spectrosc.*, vol. 65, pp. 1–14, 2010.

[19] E. Tognoni, G. Cristoforetti, S. Legnaioli, V. Palleschi, A. Salvetti, M. Mueller, U. Panne, and I. Gornushkin, "A numerical study of expected accuracy and precision in Calibration-Free Laser-Induced Breakdown Spectroscopy in the assumption of ideal analytical plasma," *Spectrochim. Acta - Part B At. Spectrosc.*, vol. 62, pp. 1287–1302, 2007.

[20] E. T. A. Ciucci, M.Corsi, V. Palleschi, S. Rastelli, A. Salvetti, "New Procedure for Quantitative Elemental Analysis by Laser-Induced Breakdown Spectroscopy," *Appl. Spectrosc.*, vol. 53, pp. 960–964, 1999.

[21] S. P. N. K. Rai and A. K. R. S. N. Thakur, “Contaminant concentration in environmental samples using LIBS and CF-LIBS,” *Appl. Phys. B*, vol. 98, pp. 231–241, 2010.

[22] M. L. Shah, A. k. Pulhani, G. P. Gupta, and B. M. Suri, “Quantitative elemental analysis of steel using calibration-free laser-induced breakdown spectroscopy,” *Appl. Opt.*, vol. 51, pp. 4612–4621, 2012.

[23] R. Gaudiuso, M. Dell’Aglio, O. De Pascale, A. Santagata, and A. De Giacomo, “Laser-induced plasma analysis of copper alloys based on local thermodynamic equilibrium: An alternative approach to plasma temperature determination and archeometric applications,” *Spectrochim. Acta - Part B At. Spectrosc.*, vol. 74–75, pp. 38–45, 2012.

[24] R. Gaudiuso, M. Dell’Aglio, O. De Pascale, S. Loperfido, A. Mangone, and A. De Giacomo, “Laser-induced breakdown spectroscopy of archaeological findings with calibration-free inverse method: Comparison with classical laser-induced breakdown spectroscopy and conventional techniques,” *Anal. Chim. Acta*, vol. 813, pp. 15–24, 2014.

Chapter 4

Inverse calibration free approach

4.1. Introduction

In this work Laser Induced Breakdown Spectroscopy, performed with fs laser pulses, is used to analyze a set of bronze and brass certified standards.

The inverse Calibration – Free method (inverse CF – LIBS), described in section 3.7., is applied for estimating the temperature of the fs laser induced plasma in order to optimized this quantitative method for analysis of copper based alloys.

This approach has been already studied for this type of sample by Gaudiuso et al. [1], [2] with good results.

The use of ultra-short laser pulses avoids the widespread melting of the laser incident zone together with a limited damage of surrounding target surface [3] and this favours the retaining of the starting material stoichiometry and the possibility of performing depth profile analysis [2], [4]–[6].

On the other hand, the lack of interaction between the ultra-short laser beam and the formed expanding plasma lead to a rapid plasma quenching [7], [8].

As a consequence, the detected emission lines show extremely weak intensities affecting, strongly, the technique sensitivity [9], [10].

The aim of this work is the valuation of fs inverse CF – LIBS for the compositional evaluation of seven brass and bronze certified standards.

The results show that the composition vary considering diverse temperatures and the plasma temperature has been determined taking into account the best compositional match found between the certified standard and the experimental evaluated composition.

4.2. Experimental set up LIBS

In this section the details of the basic components of a LIBS system are described.

The main components of a conventional LIBS set up include a laser, focusing lens, a detection system, to spectrally resolve the collected light, and a computer, to process the signal and data storage.

A schematic set up used in this work is shown in Fig. 4.1.

The LIBS experimental setup has been modified as needed for each of the particular experiments as explained in next chapters.

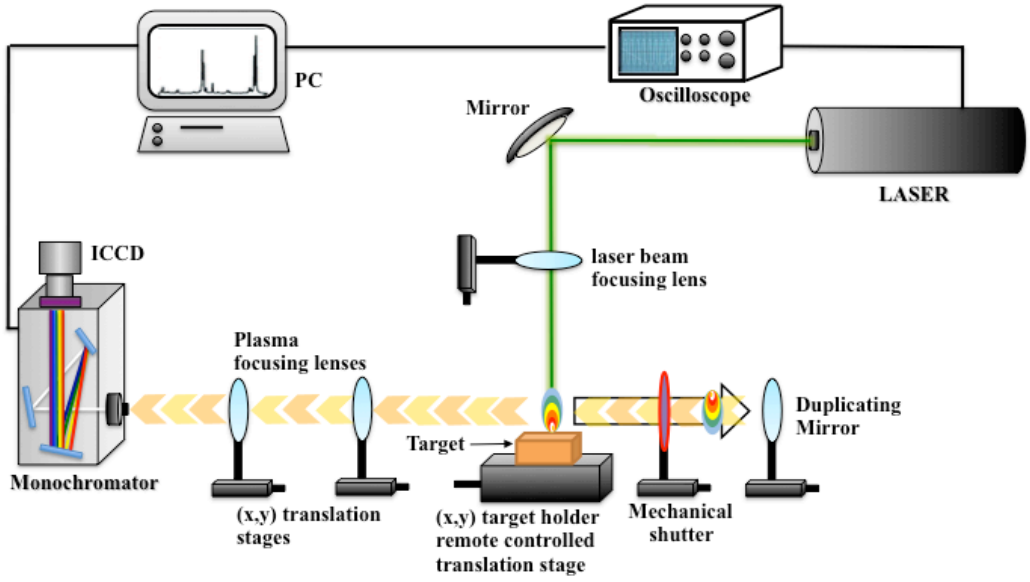

Fig. 4.1.: Sketch of the experimental LIBS set up used for analytical analysis

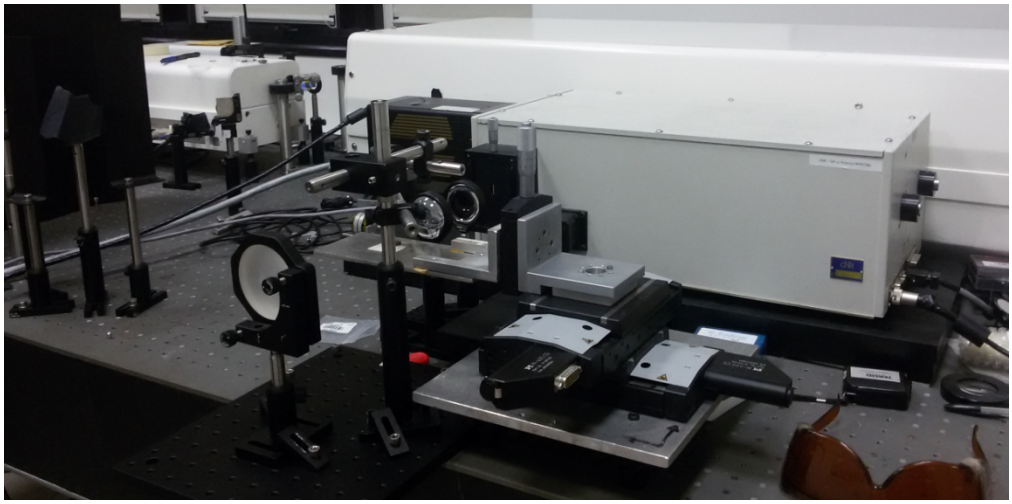

Fig. 4.2.: Picture of the experimental set up LIBS used that show: fs Nd: Glass Laser, stage holder, focusing system, duplicating mirror, spectrometer and detector

4.2.1 fs Nd: Glass Laser

Recently, the use of femtosecond lasers is becoming more frequent in LIBS [11].

In this work, the laser employed to analyze archaeological artefacts is the femtosecond Nd:Glass laser (Twinkle, Laser Conversion Ltd), showed in Fig. 4.2.

This laser is composed by two solid state active media:

- the first solid state that constitutes the oscillator (Master – Oscillator, MO),
- the second one that represents the amplifier (Regenerative Amplifier, RA).

The population inversion is reached thanks to flash lamp fed by 900 V voltage. To obtain ultra short laser pulses (ranging from picoseconds to femtoseconds), passive and active Mode – Locking combined with chirped pulse amplification (CPA) are employed.

Inside laser cavity, each longitudinal mode is forced to operate with a fixed phase through the passive Mode – Locking system.

The passive Mode – Locking is made by a saturable absorber, diluted to 90% in methanol, that allows to obtain pulses with a Full Width Half Maximum (FWHM) of 1.3 ps and 1 μJ energy.

The active Mode – Locking is made by a piezoelectric which generates a radiofrequency giving a stationary acoustic wave.

Finally, the output pulses with controlled intensity and a precise phase correlation between the longitudinal modes are given by a optical shutter.

A schematic of the principal laser components is shown in Fig. 4.3.

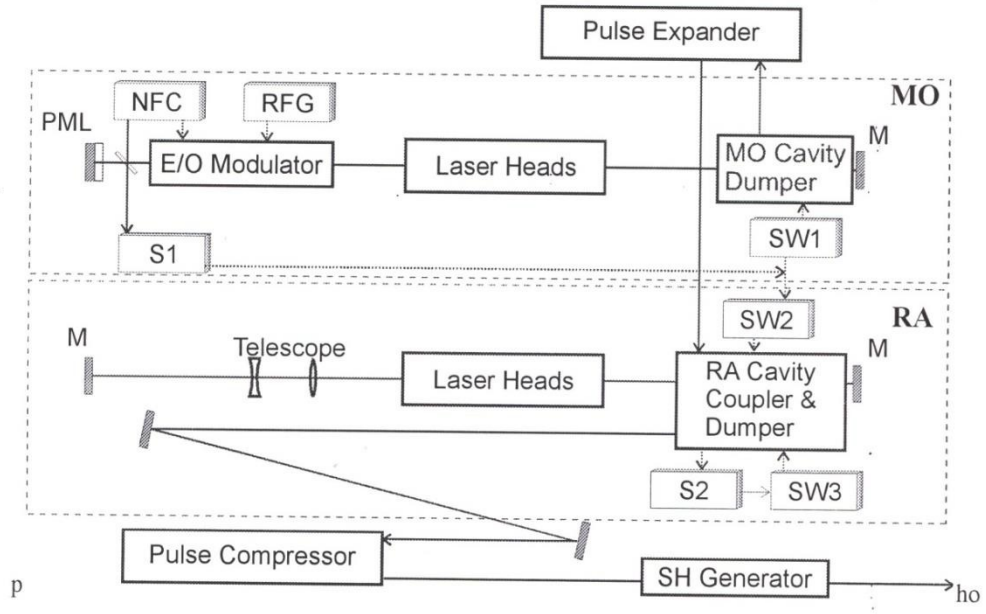

Fig. 4.3: Schematic of the fs Twinkle laser. MO: Master Oscillator; RA: Regenerative Amplifier; PML: Passive Mode – Locker; M: mirror; NFA: Negative Feedback Controller; SW1 – SW3: Q – Switch.

The ultra short laser, that has a high repetition rates, produced pulse with energy of the order of nano – Joules that are too low to allow materials processing.

Consequently, these pulses are amplified of about 4 magnitude order by Chirped Pulse Amplification technique, that can be used to amplify fs pulses without non linear pulse distortion and optical components damage.

With this technique (Fig. 4.4.), the pulse initially passed through a dispersive element, represented by a pair of gratings or prisms, which stretches the pulse temporally and reduces power and broadening laser pulse.

The pulse expander of the instrument used for experimental analysis is made by a couple of diffraction grating coated with gold and having 1800 g/mm. The output pulse is temporally expanded until 300 ps. After, the stretched pulse passes into the amplifier inside the RA cavity.

The amplified pulse is temporally compressed passing through a compressor made by two diffraction gratings similar to those employed in the pulse expander.

In this way, the different spectral components, previously separated by the pulse expander, are again time correlated.

To synchronize pulses, two Q – Switchs are employed which have a voltage of 3.5 and 6.3 KVolts.

Finally, the resulting output pulse has 1.3 ps width, 1055 nm fundamental wavelength and 8 mJ energy.

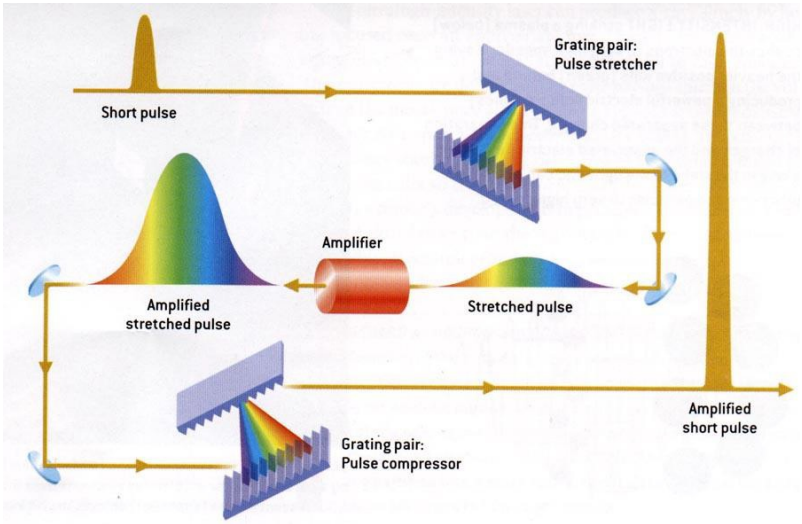

Fig. 4.4.: The process of chirped pulse amplification [11].

The fundamental radiation is duplicated by KDP (KH_2PO_4) frequency doubling crystal, obtaining wavelength in visible range, precisely of 527 nm.

To obtain 250 fs pulses, a group of optical fibers (Light Conversion Ltd) has been employed, which allows a further pulse compression.

This laser has a repetition operation rate of 50 Hz.

The experimental conditions used change for each type of analysis as well as the set up configurations. For this reason the conditions will be specified in following sections.

4.2.2. Sample holder

A great advantage of LIBS set up is the possibility of analyze sample in remote control and without any vacuum system.

In this instrument, a target holder is placed on a motorized remote controlled x,y translation stage (Physik Instrument M405CG, inc. Motion 0.1 µm) and a manual one (10 µm resolution) along the z axis.

4.2.3 Focusing and light collection system

For plasma light collection, lenses, mirrors and fiber are used.

The lens system consists of two bi-convex lenses whereas fiber consists of a circular bundle of 19 individual fibers.

The ablating fs laser beam was conveyed perpendicularly onto the target surface by placing a focusing lens.

For inverse CF LIBS set up, a duplicated mirror is also used, placed opposite to the spectrograph behind the induced plasma and away from it at twice the value of its focal length, f_{mirror} = 10 cm and d = 20 cm.

The overlapping between the original image induced by the fs laser with the image coming from the spherical mirror was always checked after each single x,y translation of the target under investigation [39].

A mechanical shutter is employed for locking the mirror duplicating path and allowing data acquisitions with and without mirror.

The following picture (Fig. 4.5) shows schematically the duplicating mirror operation:

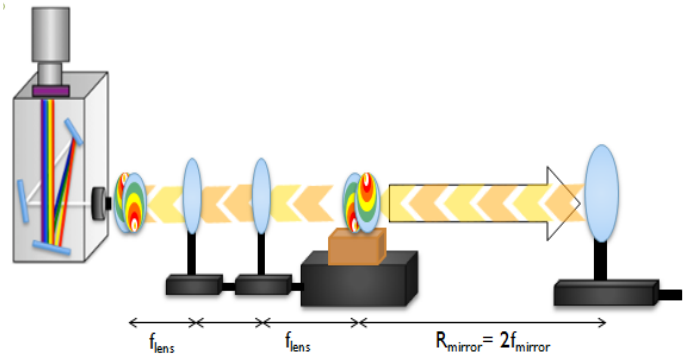

Fig. 4.5.: Schematic representation of the plasma images on the slit with and without the mirror

4.2.4. Spectrometer

Important features of a good spectrometer for LIBS detection are spectral resolution and wide band spectral range.

The Czerny-Turner spectrometers are widely used in order to disperse LIBS signal because they have a good spectral resolution but a disadvantage is the small spectral range, limited to few nanometres.

For this reason, sequential measurements, in different ranges of the spectrum, are needed to detect wide spectral ranges.

This procedure limits LIBS measurements to homogenous samples, indeed, analyzing inhomogeneous samples, plasmas may be different from one area to another, producing shot to shot variations in the analysis.

To obtain simultaneously detection over wide spectral range (200 –780 nm), it is possible to use Echelle Spectrometer, that has a excellent resolution and make possible simultaneous multi – elemental analysis practically in the complete UV – VIS spectral range avoiding spectral interferences.

In these experiments, to detect the atomic time resolved spectra, a Czerny – Turner spectrograph (Action Research Corp. 500i) is used, equipped with a turret mounting a three diffraction gratings (2400, 1200 and 150 grooves/mm) having a spectral resolution, at 500 nm, of 0.008, 0.015 and 0.17 nm/pixel, respectively.

The emission spectra are acquired by a monochromator slit aperture set at 50 μm and 2400 grooves/mm grating (resolution $\lambda/\Delta\lambda = 10000$).

Depending on the spectral range, light is dispersed with a spectral resolution of 0.04 – 0.3 nm.

4.2.5. Detector

Detection of light after its dispersion can be achieved using charge-coupled devices. In these experimental set up, space and time resolved plasma is achieved by a fast

Intensified CCD (ICCD) detection system by Princeton, equipped with a grid of 15 µm/pixel 1024 × 1024 pixels (PIMax II).

The spectral widths obtained is of about 20 nm and the gated system has a best time resolution of 2 ns.

The digital information of the ICCD detector is transferred and stored on the system of data acquisition and analysis which consists of a Personal Computer.

Through a trigger signal of the power supply it is possible to synchronize the detector system with the laser pulse, in order to avoid Bremsstrahlung and early plasma emission.

Moreover, to relate the absolute values of the emitters obtained in different spectral ranges, a radiometric calibration of the monochromator and the detecting system was performed by the use of Ocean Optic DH-2000-CAL calibration standard source.

To obtain LIBS signal for qualitative and quantitative analysis usual delay time, t_d, and gate time, t_g, were on the micro second scale. Those times scales were selected to optimize signal to background ratio (SBR) for each experiment.

Delay time and gated time for data acquisition depend on energy, sample properties and other parameters.

Typical delay time values in our experiments are about 200 ns. Gate time values for signal acquisition are between 500 – 10000ns.

4.3. Experimental methodology

The chemical composition of the seven commercial certified standards employed (TechLab – Metz – France) are reported in Table 4.1.

The composition of these standard samples varied and includes different copper – based alloys, such as low and high tin bronze and, also, low and high zinc brass.

Sample	Element	Certified wt%
B3	Cu	80.25 ± 0.03
	Ni	1.53 ± 0.02
	Pb	1.65 ± 0.01
	Sn	12.96 ± 0.03
	Zn	2.27 ± 0.03
B4	Cu	84.00 ± 0.21
	Ni	0.57 ± 0.02
	Pb	2.50 ± 0.07
	Sn	11.05 ± 0.09
	Zn	1.21 ± 0.01
B21	Cu	83.05 ± 0.07
	Ni	1.21 ± 0.02
	Pb	3.79 ± 0.08
	Sn	5.13 ± 0.10
	Zn	6.17 ± 0.09
B22	Cu	82.75 ± 0.08
	Ni	2.56 ± 0.03
	Pb	6.12 ± 0.06
	Sn	3.85 ± 0.10
	Zn	4.40 ± 0.03
L3	Cu	62.35 ± 0.11
	Ni	0.90 ± 0.02
	Pb	1.02 ± 0.02
	Sn	1.50 ± 0.05
	Zn	32.70 ± 0.17
LH1-1	Cu	66.80 ± 0.21
	Ni	2.91 ± 0.05
	Pb	1.26 ± 0.03
	Sn	0.44 ± 0.02
	Zn	26.20 ± 0.17
UZS	Cu	78.98 ± 0.24
	Ni	0.49 ± 0.01
	Pb	0.57 ± 0.01
	Sn	0.40 ± 0.02
	Zn	15.30 ± 0.11

Table 4.1: Elemental composition of the copper-based certified standards used.

The emission spectra have been acquired by using a telescope made of a pair of spherical fused silica lenses (f lens = 6.0 cm).

The 1 : 1 laser induced emitting plasma is carefully directly imaged onto the entrance slit plane of the spectrograph in order to ensuring the detection of the central part of the expanding plasma. For getting snapshots of the expanding plasma a zero order of the spectrograph and 1.4 mm slit aperture were used [12] [13].

This choice allowed the investigation of the core homogeneous and most representing part of the plasma or otherwise the one less affected by the surrounding air at atmospheric pressure background [2].

In order to limit effects due to the formation of a deep crater induced by the fs laser pulses, all data were continuously acquired moving the sample in a region not previously ablated (100 μm/s which means an average of 50 laser pulses per single laser ablated area) which means a sampling layer of about 25 – 30 μm of the material [14].

The ablating fs laser beam was conveyed perpendicularly onto the target surface by placing the fs focusing lens 1.0 mm prior to its experimentally evaluated focal point.

In table 5.2. the experimental conditions used for LIBS analysis are summarized:

Fs energy laser	3.0 ± 0.1 mJ
Fluence laser	1.5 ± 0.1 J cm^{-2}
Delay time	200 ns
Gate time	500 ns
Laser pulses	50

Table 4.2.: LIBS Experimental conditions

The electronic transitions considered as well as the Einstein coefficient of spontaneous emission for the “ul” transition, the degeneracy of the upper level, the emitted photon frequency and the energy of the upper level are reported in Table 4.3.

Element	λ(nm)	E_u (eV)	E_{ul} (eV)	g_u	A_{ul} (s^{-1})
Cu I	301.08	5.506	4.117	6	$1.298 \cdot 10^6$
	303.61	5.725	4.083	4	$2.428 \cdot 10^6$
	306.34	5.688	4.047	4	$1.550 \cdot 10^6$
	312.61	8.803	3.965	4	$7.617 \cdot 10^7$
	312.86	8.935	3.962	6	$2.213 \cdot 10^7$
Ni I	300.36	4.235	4.127	5	$6.912 \cdot 10^7$
	301.20	4.538	4.116	5	$1.340 \cdot 10^8$
	303.79	4.105	4.080	7	$2.842 \cdot 10^7$
	308.07	4.236	4.024	5	$8.661 \cdot 10^6$
Pb I	336.96	3.678	3.678	7	$1.835 \cdot 10^7$
	280.20	5.744	4.424	7	$1.081 \cdot 10^8$
	282.32	5.711	4.391	5	$3.044 \cdot 10^7$
	287.33	5.634	4.314	5	$4.151 \cdot 10^7$
Sn I	300.91	4.329	4.119	3	$3.714 \cdot 10^7$
	303.41	4.295	4.086	1	$1.513 \cdot 10^8$
	326.23	4.867	3.799	3	$3.309 \cdot 10^8$
	333.06	4.789	3.722	5	$1.584 \cdot 10^7$
Zn I	307.21	8.113	4.035	3	$1.702 \cdot 10^7$
	330.26	7.783	3.753	5	$1.072 \cdot 10^8$

Table 4.3: Spectroscopic constant of the electronic transitions employed.

In order to evaluate the line intensities of the single atomic emissions, Voigt line profile functions were adopted for their fit [15], [16].

Voigt line profiles have been used in order to take into account the asymmetries and line shape tailings occurring for the electronic transitions considered in this work. The employment of this approach has shown its usefulness in Reference [16].

With regard to the investigated transitions of the emitting species, a particular attention was made in considering their excited energy levels for avoiding self-absorption effects as well as interferences caused by other emitting elements.

All the spectroscopic data corresponding to the investigated emission lines were obtained from the Kurucz atomic spectral line database [17].

For compensation of self absorption effect for the main component, i.e. copper, the spherical duplicating mirror method is used (described in section 4.2.3.).

The correction factor, $K_{\lambda,corr}$, for measuring the peak line intensity can be calculated by this equation:

$$K_{\lambda,corr} = \frac{\ln[(R^C - 1)(R_\lambda - 1)]}{1 - \frac{(R_\lambda - 1)}{(R^C - 1)}}$$

(eq. 4.1.)

Where R^C is equal to $B^C_{\lambda 2}/B^C_{\lambda 1}$ and R_λ is equal to $B_{\lambda 2}/B_{\lambda 1}$.

The Cu self – absorption parameters, experimentally determined, for B22 sample can be, also, used for all certified standards, obtaining a good correlation.

For this reason, the procedure of evaluating correction parameter in copper based samples with unknown composition can be avoided, taking into account just that experimentally determined for the standard one.

This approximation can indeed speed up the analysis of copper based samples with unknown composition, limiting the surface damage due to longer exposition to the laser shots.

Moreover, this feature can be extremely advantageous also for depth profile analysis of archaeological artefacts, that present inhomogeneity in corrosion layers.

4.4. Inverse CF LIBS method for plasma temperature evaluation

During fs LIBS, because of the plasma recombination phenomena that are more pronounced in initial stage of expanding plasma, the first 200 ns of the expansion of the plasma generated by ultra-short laser pulses are not be taken into account, for assessing the plasma temperature.

For these reason, the ionic emitting species could not be detected and, hence, Equations 3.3. and 3.5. refer to the same value [7].

Considering only one standard bronze sample B22, it is possible to obtain an indirect evaluation of the plasma temperature.

Through Equation 3.6., the weight percentage (wt%) of each element in standard B22 has been calculated at different values of the hypothetical considered temperature, ranging between 7000 K and 11000 K (Table 4.4.).

	wt% cert	**wt% 7000 K**	**wt% 7500 K**	**wt% 8000 K**	**wt% 8500 K**	**wt% 9000 K**	**wt% 9500 K**	**wt% 10000 K**	**wt% 10500 K**	**wt% 11000 K**
Cu	82.75	82.72	83.91	84.73	85.16	85.36	85.38	85.33	85.13	84.96
Ni	2.56	1.17	1.39	1.60	1.81	2.01	2.22	2.40	2.60	2.78
Pb	6.12	4.90	4.98	5.01	5.00	4.99	4.98	4.96	4.95	4.93
Sn	3.85	2.18	2.57	2.94	3.31	3.66	4.01	4.34	4.67	4.97
Zn	4.40	8.79	6.83	5.40	4.40	3.65	3.09	2.64	2.32	2.04

Table 4.4: Comparison between the wt% certified and wt% experimentally evaluated amount of each element present in the standard sample B22 performed by the inverse CF approach at temperatures ranging between 7000 and 11000 K

The plasma temperature is indirectly determinate assuming as the correct value which minimizes the discrepancy between the composition of the certified standard and the different compositions experimentally evaluated.

This can be expressed by considering the following equations:

$$\Delta \mathrm{wt\%_i} = \left| \frac{\mathrm{wt\%_{cert,i}} - \mathrm{wt\%_{exp,i}(T)}}{\mathrm{wt\%_{cert,i}}} \right| \qquad \text{(eq. 4.2.)}$$

Where $\Delta \mathrm{wt\%_i}$ refers to the deviation in percentage of the species “i”, and reaches its minimum value when the optimal temperature is used for the calculation.

The discrepancy is obtained by averaging the number of components in the standard sample, as shown in the following equation:

$$\text{Average } \Delta \mathrm{wt\%} = \frac{\sum \Delta \mathrm{wt\%_i}}{\mathrm{N_i}} \qquad \text{(eq. 4.3.)}$$

In this work the N_i is equal to 5 because the elements taken into account are Cu, Zn, Sn, Pb and Ni.

The Fig. 4.6. reports how for the certified sample B22 the mean Δwt% value changes with T.

It is shown that the best temperature for determining the composition of the sample under investigation is obtained at T = 9500 K.

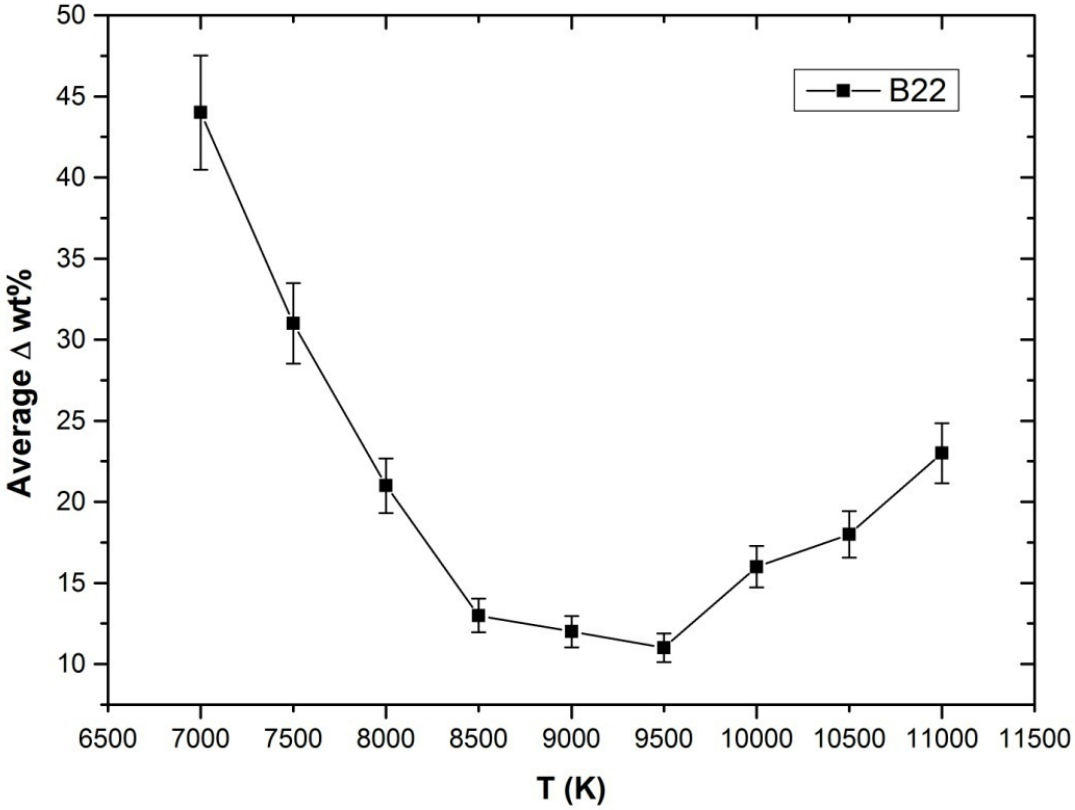

Fig. 4.6.: Mean Δwt% vs. T(K) graphical behaviour of the certified sample.
This indicates 9500 K as the optimal temperature of the plasma to be considered.

Subsequently, the method is validated using the other bronze and brass standard for taking into account possible matrix effect.

The mean Δwt% vs. T(K) graphical behaviour of all certified samples has been drawn and reported hereafter.

Figure 4.7. shows that some differences occur for the investigated sample in establishing their optimal plasma temperature. In any case these belong to the range of 8500 – 10 000 K.

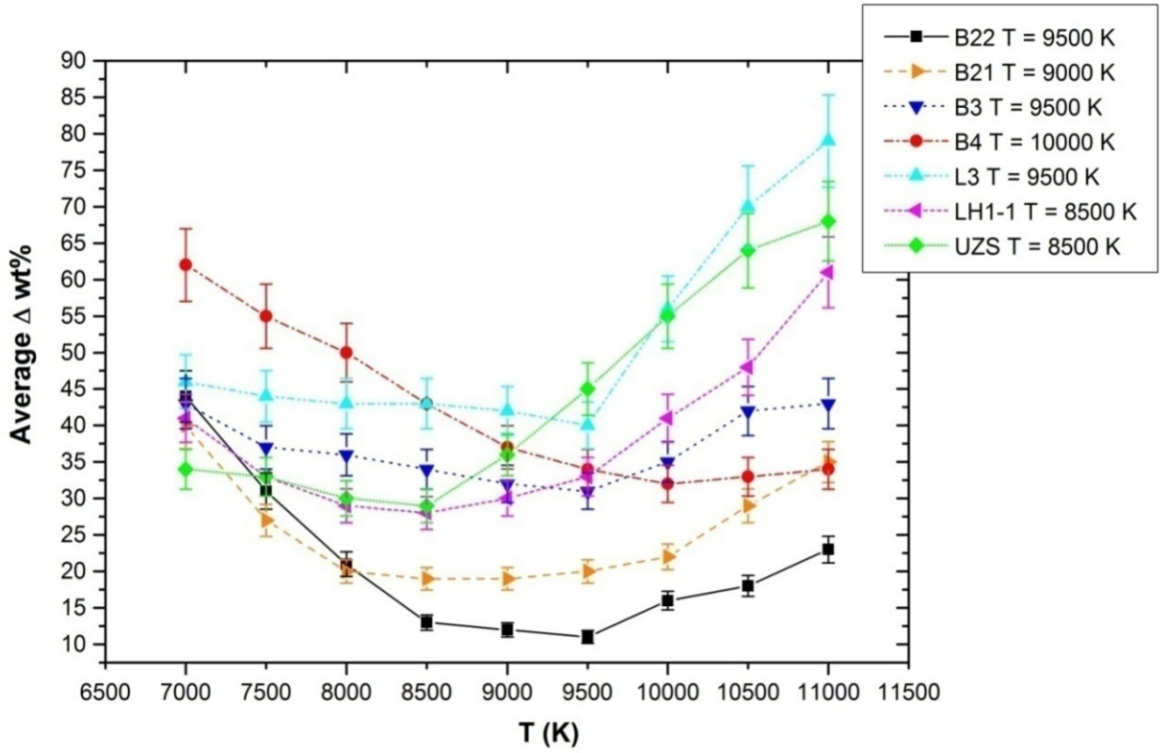

Fig. 4.7.: Mean Δwt% vs. T(K) graphical behaviours related to all the certified samples used. The embedded legend reports, for each sample, the optimal T of the relative plasma to be considered.

However, the optimum value of temperature for all standard samples can be considered equal to 9500 K.

4.5. Analysis of the copper-based certified samples

After the experimental determination of plasma temperature, the composition of all samples has been obtained using the previous eq. 3.3 and eq. 3.6.

The following Table 4.5. reports the difference between the certified value of each component and the experimentally determined one at the fixed temperature of 9500 K.

The deviation of the measured quantity of each element has been calculated through next equation:

$$\delta \mathrm{wt\%_i} = \left| \frac{\mathrm{wt\%_{cert,i}} - \mathrm{wt\%_{exp,i}(T)}}{\mathrm{wt\%_{cert,i}}} \right| \mathrm{wt\%_{exp,i}(T)}$$

(eq. 4.4.)

Table 4.5. shows that for bronzes the evaluated amount together with the relative deviation of the experimentally determined species can be out of range of the certified elemental composition of the related sample and a large percentage difference can occur.

Sample	Element	Certified wt%	Inv. CF method – experimental wt%
B3	Cu	80.25 ± 0.03	86 ± 6
	Ni	1.53 ± 0.02	1.9 ± 0.6
	Pb	1.65 ± 0.01	2 ± 1
	Sn	12.96 ± 0.03	7 ± 3
	Zn	2.27 ± 0.03	1.1 ± 0.6
B4	Cu	84.00 ± 0.21	90 ± 6
	Ni	0.57 ± 0.02	0.9 ± 0.6
	Pb	2.50 ± 0.07	2.1 ± 0.4
	Sn	11.05 ± 0.09	6 ± 3
	Zn	1.21 ± 0.01	1.2 ± 0.5
B21	Cu	83.05 ± 0.07	84 ± 1
	Ni	1.21 ± 0.02	1.7 ± 0.6
	Pb	3.79 ± 0.08	2.8 ± 0.9
	Sn	5.13 ± 0.10	4.5 ± 0.6
	Zn	6.17 ± 0.09	4 ± 1
B22	Cu	82.75 ± 0.08	85 ± 2
	Ni	2.56 ± 0.03	2.22 ± 0.3
	Pb	6.12 ± 0.06	5.0 ± 0.9
	Sn	3.85 ± 0.10	4.0 ± 0.2
	Zn	4.40 ± 0.03	3.1 ± 0.9
L3	Cu	62.35 ± 0.11	72 ± 10
	Ni	0.90 ± 0.02	0.97 ± 0.07
	Pb	1.02 ± 0.02	1.9 ± 0.9
	Sn	1.50 ± 0.05	2.2 ± 0.9
	Zn	32.70 ± 0.17	18 ± 8

LH1-1	Cu	66.80 ± 0.21	77 ± 10
	Ni	2.91 ± 0.05	2.6 ± 0.3
	Pb	1.26 ± 0.03	1.1 ± 0.1
	Sn	0.44 ± 0.02	0.7 ± 0.4
	Zn	26.20 ± 0.17	17 ± 0.6
UZS	Cu	78.98 ± 0.24	82 ± 3
	Ni	0.49 ± 0.01	0.8 ± 0.6
	Pb	0.57 ± 0.01	1.0 ± 0.6
	Sn	0.40 ± 0.02	0.8 ± 0.9
	Zn	15.30 ± 0.11	8 ± 4

Table 4.5.: Comparison between the wt% certified and wt% experimentally evaluated of each element present in the single standard sample used performed by the inverse CF-LIBS. The temperature of 9500 K has been considered for both brass and bronze type of samples.

As a matter of example, for bronzes the Zn and Sn composition difference can reach 52% and 46%, respectively for B3, or 26%, 12% and 35% for the Pb, Sn and Zn amount in B21, respectively.

For brasses this behaviour is quite marked for Zn where differences of 47%, 44% and 35% are obtained for UZS, L3 and LH11 samples.

These large deviations can be due to three approximations: 1) the self-absorption effect which should not be ruled out even for minor components; 2) the matrix effects that can be involved so that the assumption in considering one plasma temperature for brass and bronzes represents an approximation; 3) plasma features where the excitation de-excitation processes taking place due to electron collisions could induce departures from LTE conditions.

Although, some more investigations would be beneficial in determining the whole parameters which could induce the approximation of the method, it should be kept in mind that, compared to other approaches, the single pulse fs-LIBS can be extremely advantageous for high spatial depth profiling analysis.

For this, a good approximation of the compositional data here shown, can be still accepted if one considers that the assumed working temperature of the plasma has been obtained by the use of one single standard and that the self-absorption effect has just been determined for the main component and not for the other variable ones.

4.6. Correction with calibration curve method: hybrid method

However, in order to reduce the observed differences between the certified and experimental wt% values of the analyzed elements a correction using calibration curves has been introduced.

In this way the correlation between the experimentally evaluated and certified composition of the standards here used has been straightforwardly retrieved through the linearity of the reported calibration curves.

The calibration curves of the certified copper-based-alloy minor constituents (i. e. Sn, Pb, Ni and Zn) have been drawn.

Since the self-absorption effect determined for the major Cu component is assessed through the spherical duplicating mirror method, experimentally acquired signals of Cu have been considered as an internal standard.

With this purpose the following plots of the experimentally detected intensities of Zn/Cu, Sn/Cu, Pb/Cu, and Ni/Cu vs. the certified wt% of Zn, Sn, Pb and Ni respectively, have been reported in Fig. 4.8.

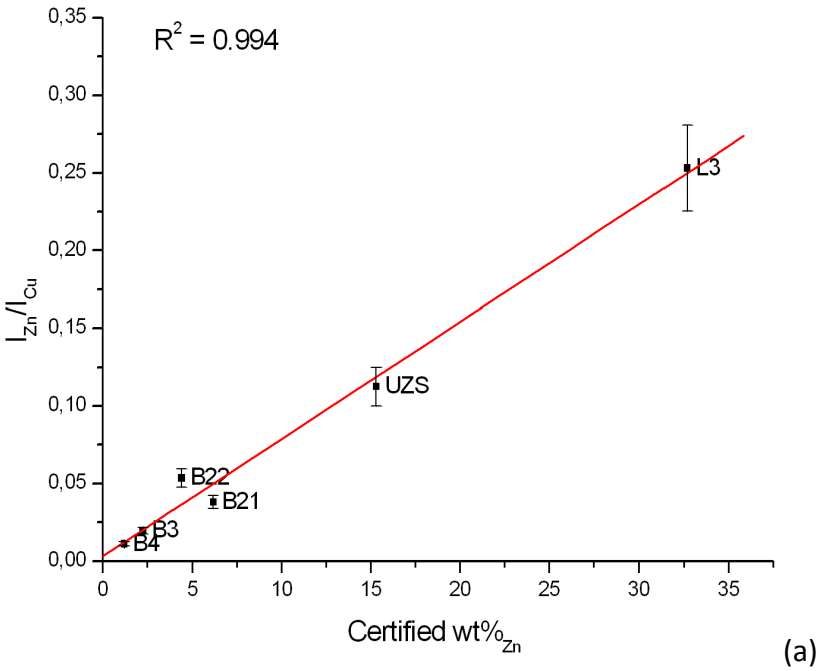

(a)

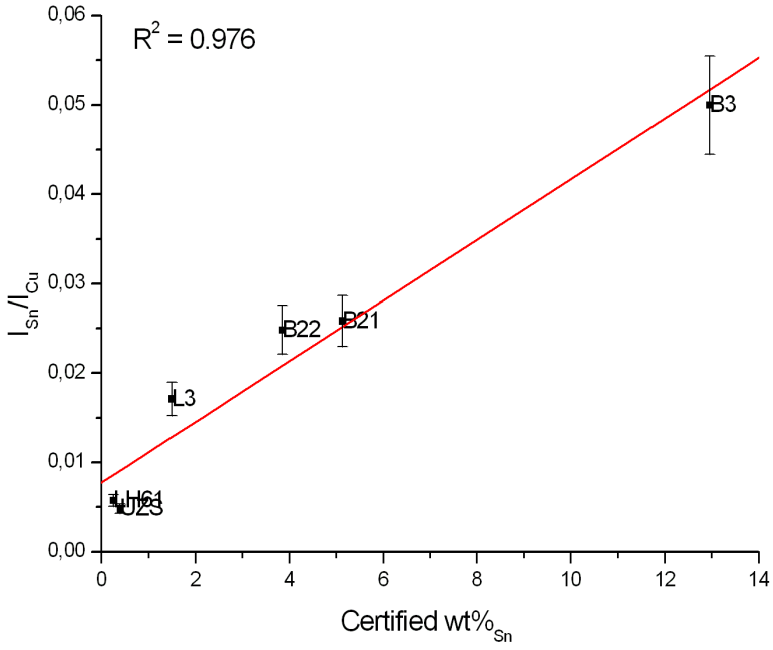
R² = 0.976
B3
B22
B21
L3
LH61
UZS
I_Sn/I_Cu
Certified wt%_Sn
0,00
0,01
0,02
0,03
0,04
0,05
0,06
0
2
4
6
8
10
12
14

(b)

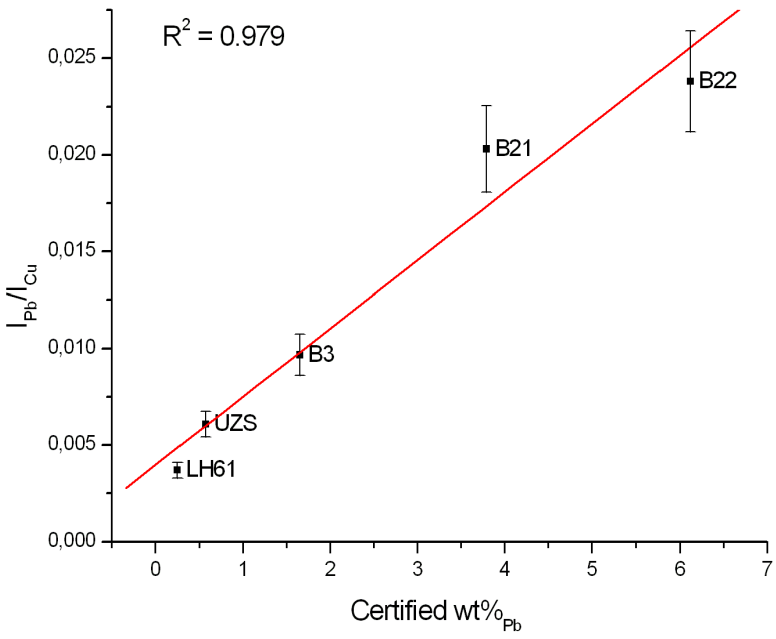
R² = 0.979
B22
B21
B3
UZS
LH61
I_Pb/I_Cu
Certified wt%_Pb
0,000
0,005
0,010
0,015
0,020
0,025
0
1
2
3
4
5
6
7

(c)

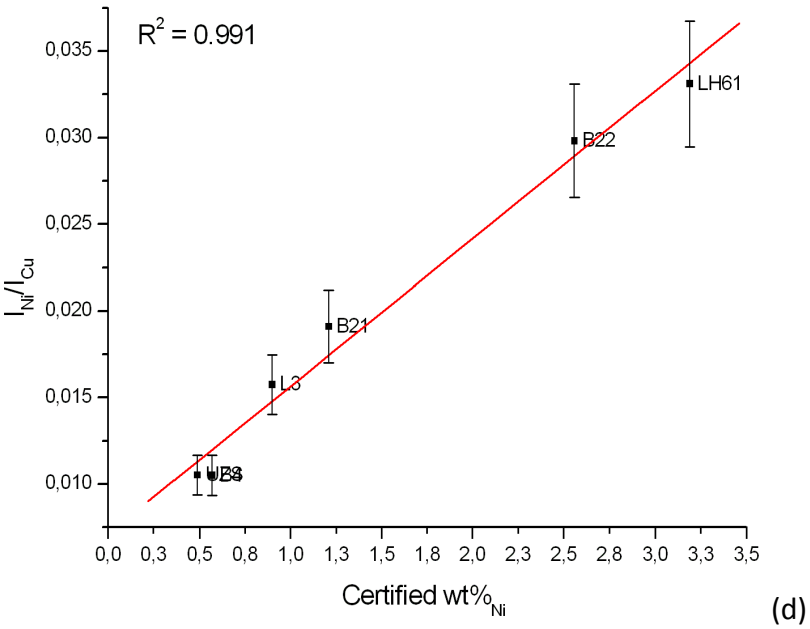

Fig. 4.8.: Calibration curves of the single species where Cu has been taken as the internal standard. The ratios of signal intensities vs. the relative wt% of each species is reported. a) Zn/Cu vs. certified wt% of Zn, b) Sn/Cu vs. certified wt% of Sn, c) Pb/Cu vs. certified wt% of Pb, and d) Ni/Cu vs. certified wt% of Ni. An average of the following emission line intensities Zn λ=307.21 nm, Sn λ=300.91 nm and λ=303.41 nm, Pb λ=280.20 nm and λ=282.32 nm, Ni λ=300.36 nm, λ=301.20 nm and λ=303.79 nm and Cu λ=301.08 nm and λ=303.61 nm have been taken into account.

The linearity of these plots confirms that no preferential evaporation of species occurs and, consequently that the target composition is retained.

These behaviours lead us in considering that fractionation effects, and therefore change in stoichiometry of the emitting plasma, can be neglected.

Furthermore, if more certified standards are available the unknown composition of a copper-based sample can be determined using the parameters of the linear fits of Fig. 4.8.

In this case the wt% of the missing Cu amount can be determined by difference of the wt% of the other species with 100%.

$$\mathrm{wt\%_{Cu}} = \sum_{\mathrm{Cu,Ni,Pb,Sn,Zn}} \mathrm{wt\%_{certif}} - \sum_{\mathrm{Ni,Pb,Sn,Zn}} \mathrm{wt\%_{exper}} \qquad \text{(eq. 4.5.)}$$

Table 4.6. reports a comparison between the compositional evaluation of the copper-based alloys here used obtained by this hybrid method.

Sample	Element	Certified wt%	Hybrid method – experimental wt%
B3	Cu	80.25 ± 0.03	80.6 ± 0.4
	Ni	1.53 ± 0.02	1.7 ± 0.2
	Pb	1.65 ± 0.01	3 ± 2
	Sn	12.96 ± 0.03	12 ± 1
	Zn	2.27 ± 0.03	1.6 ± 0.5
B4	Cu	84.00 ± 0.21	86 ± 2
	Ni	0.57 ± 0.02	0.52 ± 0.04
	Pb	2.50 ± 0.07	2.0 ± 0.4
	Sn	11.05 ± 0.09	8 ± 2
	Zn	1.21 ± 0.01	2 ± 1
B21	Cu	83.05 ± 0.07	83.06 ± 0.01
	Ni	1.21 ± 0.02	1.3 ± 0.1
	Pb	3.79 ± 0.08	3.3 ± 0.4
	Sn	5.13 ± 0.10	5.9 ± 0.9
	Zn	6.17 ± 0.09	5.7 ± 0.4
B22	Cu	82.75 ± 0.08	82.82 ± 0.07
	Ni	2.56 ± 0.03	2.08 ± 0.4
	Pb	6.12 ± 0.06	6.3 ± 0.1
	Sn	3.85 ± 0.10	4.2 ± 0.4
	Zn	4.40 ± 0.03	4.3 ± 0.1
L3	Cu	62.35 ± 0.11	66 ± 3
	Ni	0.90 ± 0.02	0.7 ± 0.1
	Pb	1.02 ± 0.02	2 ± 1
	Sn	1.50 ± 0.05	2.1 ± 0.8
	Zn	32.70 ± 0.17	28 ± 4
LH1-1	Cu	66.80 ± 0.21	67.3 ± 0.5
	Ni	2.91 ± 0.05	3.3 ± 0.4
	Pb	1.26 ± 0.03	0.6 ± 0.5
	Sn	0.44 ± 0.02	0.2 ± 0.1
	Zn	26.20 ± 0.17	27 ± 1
UZS	Cu	78.98 ± 0.24	83 ± 4
	Ni	0.49 ± 0.01	0.57 ± 0.09
	Pb	0.57 ± 0.01	0.2 ± 0.1
	Sn	0.40 ± 0.02	0.26 ± 0.09
	Zn	15.30 ± 0.11	12 ± 4

Table 4.6.: Comparison between the experimentally evaluated amount of each element present in the single standard sample used performed by the Hybrid methods.

It can be pointed out that although the calibration curves method can improve the quality of the compositional analysis some differences from the certified amounts are still present.

Anyway, plotting the wt% determinate by hybrid method as function of wt% certified for all standard sample (Fig. 4.9.), the correlation is good, confirming that when ablating similar matrices in the same conditions, plasmas is characterized by the same parameters.

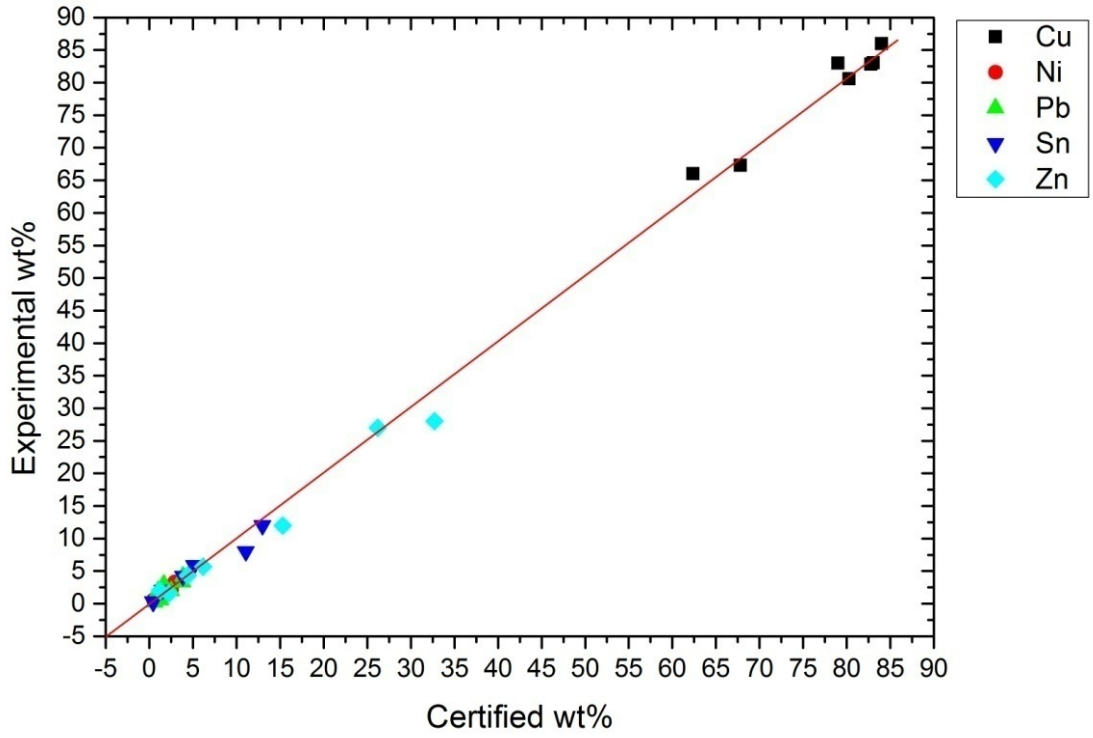

Fig. 4.9. Correlation between the certified compositions of Sn, Pb, Cu, Zn and Ni in bronze and brass standard samples, UZS and the compositions determined with hybrid method at the temperature T=9500 K (obtained for the B22 sample with the inverse method)

The estimated temperatures occurring during the process provide a good figure of merit between the certified and the experimentally determined composition of the bronze and brass materials, here employed, although further correction procedure, like the use of calibration curves, can be demanded.

4.7. Conclusions

The inverse CF method here employed for evaluating the temperature of the plasma induced by fs-LIBS of different copper-based materials has been demonstrated to provide a good approximation of the composition of all samples used.

Inverse CF method for the evaluation of the plasmas' temperature generated during fs-LIBS of seven copper-based certified standards has been used. The retrieved temperatures were in the range of 8500–10 000 K. Assuming that the LTE condition is hold and taking into account the plasma temperature value of 9500 K occurring, for example, for B22, the sample composition of all other samples has been determined. The method shows a good estimation of the single species composition unless one standard sample is available for retrieving the plasma working temperature.

Taking into account the peculiar features of fs laser pulses in avoiding thermal processes within the exposed material, it follows that the combination of this approach with fs-LIBS can be extremely valuable for depth profiling analysis.

In case of different certified standard are available the use of calibration curves can provide more accurate analysis although this could limit the straightforward employment of the technique.

As a consequence of the encouraging results obtained from this preliminary survey further studies on the fs-LIBS process and the role of self-absorption effects of minor constituents can be envisaged for optimising the inverse CF method here presented.

4.8. References

[1] R. Gaudiuso, M. Dell'Aglio, O. De Pascale, S. Loperfido, A. Mangone, and A. De Giacomo, "Laser-induced breakdown spectroscopy of archaeological findings with calibration-free inverse method: Comparison with classical laser-induced breakdown spectroscopy and conventional techniques," *Anal. Chim. Acta*, vol. 813, pp. 15–24, 2014.

[2] R. Gaudiuso, M. Dell'Aglio, O. De Pascale, A. Santagata, and A. De Giacomo, "Laser-induced plasma analysis of copper alloys based on local thermodynamic equilibrium: An alternative approach to plasma temperature determination and archeometric applications," *Spectrochim. Acta - Part B At. Spectrosc.*, vol. 74–75, pp. 38–45, 2012.

[3] C. Momma, B. N. Chichkov, S. Nolte, F. von Alvensleben, A. Tünnermann, H. Welling, and B. Wellegehausen, "Short-pulse laser ablation of solid targets," *Opt. Commun.*, vol. 129, pp. 134–142, 1996.

[4] V. Margetic, M. Bolshov, A. Stockhaus, K. Niemax, and R. Hergenröder, "Depth profiling of multi-layer samples using femtosecond laser ablation," *J. Anal. At. Spectrom.*, vol. 16, pp. 616–621, 2001.

[5] J. A. Varela, J. M. Amado, M. J. Tobar, M. P. Mateo, A. Yañez, and G. Nicolas, "Characterization of hard coatings produced by laser cladding using laser-induced breakdown spectroscopy technique," *Appl. Surf. Sci.*, vol. 336, pp. 396–400, 2015.

[6] R. Glaus and D. W. Hahn, "Fiber-coupled laser-induced breakdown and Raman spectroscopy for flexible sample characterization with depth profiling capabilities," *Spectrochim. Acta - Part B At. Spectrosc.*, vol. 100, pp. 116–122, 2014.

[7] A. De Giacomo, M. Dell'Aglio, A. Santagata, and R. Teghil, "Early stage emission spectroscopy study of metallic titanium plasma induced in air by femtosecond- and nanosecond-laser pulses," *Spectrochim. Acta - Part B At. Spectrosc.*, vol. 60, pp. 935–947, 2005.

[8] A. Santagata, R. Teghil, A. De Giacomo, M. Dell'Aglio, G. P. Parisi, A. De Bonis, and A. Galasso, "Optical emission spectroscopy investigation of an ultra-short laser induced titanium plasma reheated by a ns laser pulse," *Appl. Surf. Sci.*, vol. 253, pp. 7792–7797, 2007.

[9] P. Stavropoulos, C. Palagas, G. N. Angelopoulos, D. N. Papamantellos, and S. Couris, "Calibration measurements in laser-induced breakdown spectroscopy using nanosecond and picosecond lasers," *Spectrochim. Acta - Part B At. Spectrosc.*, vol. 59,

pp. 1885–1892, 2004.

[10] A. Elhassan, A. Giakoumaki, D. Anglos, G. M. Ingo, L. Robbiola, and M. A. Harith, “Nanosecond and femtosecond Laser Induced Breakdown Spectroscopic analysis of bronze alloys,” *Spectrochim. Acta - Part B At. Spectrosc.*, vol. 63, pp. 504–511, 2008.

[11] “Chirped Pulse Amplification,” *Michigan Engineering Centre for Ultrafast Optical Science*. .

[12] A. Guarnaccio, G. P. Parisi, D. Mollica, A. De Bonis, R. Teghil, and A. Santagata, “Fs-ns double-pulse Laser Induced Breakdown Spectroscopy of copper-based-alloys: Generation and elemental analysis of nanoparticles,” *Spectrochim. Acta - Part B At. Spectrosc.*, vol. 101, pp. 261–268, 2014.

[13] H. Y. Moon, K. K. Herrera, N. Omenetto, B. W. Smith, and J. D. Winefordner, “On the usefulness of a duplicating mirror to evaluate self-absorption effects in laser induced breakdown spectroscopy,” *Spectrochim. Acta - Part B At. Spectrosc.*, vol. 64, pp. 702–713, 2009.

[14] A. De Bonis, B. De Filippo, A. Galasso, A. Santagata, A. Smaldone, and R. Teghil, “Comparison of the performances of nanosecond and femtosecond Laser Induced Breakdown Spectroscopy for depth profiling of an artificially corroded bronze,” *Appl. Surf. Sci.*, vol. 302, pp. 275–279, 2014.

[15] M. S. S. Doniach, “Many-electron singularity i n x-ray photoemission andx-ray line spectra from metals,” *Phys. C Solid State*, vol. 3, pp. 285–291, 1969.

[16] F. Colao, R. Fantoni, V. Lazic, A. Morone, A. Santagata, and A. Giardini, “LIBS used as a diagnostic tool during the laser cleaning of ancient marble from Mediterranean areas,” *Appl. Phys. A Mater. Sci. Process.*, vol. 79, pp. 213–219, 2004.

[17] http: // www. cfa. harvard. edu/amp/ampdata. kurucz23/sekur. htm. Kurucz Atomic Spectral Lines Database.

Chapter 5

LIBS analysis for Cultural Heritage

5.1 Archaeometric study

The modern approach for a complete characterization of archaeological artefacts involves the combined use of various analytical methods and techniques [1], [2].

In addition to typological and archaeological characteristics, these scientific studies, known as archaeometric studies, can give information regarding the classification, dating and provenance of an object and are based on the integration of morphological and chemical analyses.

It is possible to distinguish different production processes that characterized ancient artefacts, for example from use of specific alloys, depending both on the historical period and on the typology of artefacts.

For a metallic archaeological finding, the archaeometric studies allow to acquire knowledge on alloys composition (major, minor and if possible trace elements), metallographic features and corrosion products, in order to formulate hypotheses on the production area, e.g. on the basis of raw materials supply or to classify the analysed objects [3], [4].

Moreover, for a complete analysis of the objects, also corrosion processes and degradation phenomena can be studied in order to make possible the more adequate strategies of restoration and conservation for these metallic artefacts [2].

However, when fragile and rare artefacts are analyzed, more attention have to be take during an experiment because of their fragile structures and it is necessary to use more appropriate techniques, that alone or in combination, can provide as much as possible exhaustive information, preserving their integrity and minimizing their damage.

Laser techniques are becoming more popular because they allow to overcome these problems and offer both practical and analytical advantages [5].

LIBS has been successfully employed to the analysis of painting, pigments, metals and ceramics, and also to monitor the laser cleaning procedure and to remove corrosion and dirt patina on sample surface [3]–[18].

From this point of view, the minimal destructiveness of a femtosecond laser can be very useful for archaeological rare and precious samples because their integrity must be preserved.

However, an archaeological material should be analyzed very carefully because of inhomogeneities in chemical composition, due to alterations related to the burial conditions that, leading to very rough surface, can make measurements more difficult because, in that way, the signal of plasma is disturbed.

On the contrary, flat sample surfaces are always preferable in LIBS analysis due to advantages when the plasma is created on materials.

In this work femtosecond LIBS with CF inverse method, is applied to the study of various sets of archaeological findings, among which bronze findings and silver jewels, coming from three archaeological sites in Basilicata, Southern Italy.

The performance of this method is tested by comparing its results with those obtained by XRF, that is a conventional technique for compositional analysis [19]–[24].

Furthermore, integrating the LIBS compositional data with other analytical techniques interesting results from both the archaeometric and scientific points of view has been obtained [2].

More detailed archaeological information about the silver and bronze findings investigated will be reported in next sections.

5.1.1. Indirect dating and provenience study

Typological and dating studies are of great importance for historical and archaeological studies and are based on compositional analysis, principally on the basis of the presence of specific elements related to a technologic development.

In particular, in metallic artefacts, the correct identification of alloys, mainly the presence of some elements, may mark the progress of metallurgy and allows an indirect dating.

Additionally the presence of trace elements may reveal the use of particular raw material or may be associated to characteristic contaminants on surface layers prior to restoration [5].

Provenance studies can be useful to identify specific quarries or mines utilized since a know period or reachable only after proper development of travelling facilities and related trades.

Moreover, chemical analyses can provide useful information on the original composition and on possible successive treatments.

For the archaeologists, conservators and archaeometrical scientists, the determination of the chemical composition may help to elucidate the evolution of manufacture technology and the knowledge at ancient time.

5.1.2. Corrosion study

The study of the chemical degradation phenomena of the ancient metallic objects can provide useful information for the evaluation of the state of conservation of objects and for the understanding of degradation mechanisms, allowing to select the better methods for conservation approach.

SEM and micro-Raman analyses are used to determine both the elemental composition and surface morphology of the patina, highlighting the correlation between patina nature and composition of the burial context.

The corrosion phenomena are redox processes that cause the deterioration and degradation of the material properties and modify the chemical composition of the sample by introducing elements coming from the burial context.

In particular, the bronze artefacts present generally greenish blue or brownish green layers on the surface due principally to copper (II) compounds.

This degradation products usually cover a inner cuprous oxide layer that is directly in contact with the metal surface.

The red layer composed of cuprous oxide, known as cuprite, is responsible for the initial formation of surface patina on the archaeological bronzes which starting from the grain boundaries reaches the core of the metal alloy and causes the weakening of the artefact.

This first degradation phenomenon is related to the decuprification process [25] that consists in the selective dissolution of copper compound in the environment and, as a consequence, to a strong tin enrichment in the external surface (associated with presence of cassiterite (SnO_2)) due to the low solubility and high stability of the tin species.

This migration processes of the elements create a concentration gradient through the corrosion layer of the bronze alloys.

Furthermore, the type of the burial environment influences the type of the copper compounds that are formed in the outermost layers of the patina.

For example the outermost green degraded layer consists of Cu(II) carbonate malachite ($Cu_2(OH)_2CO_3$) that is formed in soil, Brochantite ($CuSO_4 \cdot 3Cu(OH)_3$) in the atmosphere and Atacamite ($Cu_2Cl(OH)_3$) in the seawater.

Unfortunately the bronze disease is a cyclic and autocatalytic phenomenon, increased by the air and environmental pollutants exposure.

This degradation phenomenon is very dangerous for the conservation of metal artefacts and must be take into account also during the removal of surface encrustations and corrosion product layers (especially cuprite) in order to avoid further exposure of the object to external humidity and corrosive environments, that may irremediably damage the object.

For this reason, a multidisciplinary approach, that includes LIBS, scanning electron microscopy and micro Raman spectroscopy, allows to understand the whole corrosion process.

LIBS can be useful for stratigraphic studies and for the chemical characterization of degradation compounds that are formed as successive layers at different depths.

Finally, it has been observed that, generally, the copper-alloy objects, worked via mechanical treatments are affected by more intense degradation phenomena because of the crystallization and segregation of impurities that are induce along grain boundaries.

5.2. Complementary analytical techniques

By applying complementary analytical techniques, it was possible to find out the correct alloy composition, to highlight the manufacturing process employed for each object and to increase the amount of knowledge about degradation mechanisms.

In this work the LIBS data are integrated with results from other methods, principally X-Ray Fluorescence (XRF) technique.

The comparison between LIBS and XRF techniques, here used, is particularly useful in the study of cultural heritage since their results are complementary in terms of both thickness and composition of the investigate surfaces.

Finally, the archaeological samples under study have been examined with different complementary techniques, namely: Scanning Electron Microscopy (SEM) with Energy Dispersive X Ray (EDX) and micro-Raman Spectroscopy.

The experimental methodologies applied in the various experiments and a brief description of other techniques used are outlined in the next sections.

5.2.1. X – Ray fluorescence (XRF)

The XRF technique allows qualitative and quantitative elemental analysis by measuring the X-ray fluorescent emitted from a sample when it is excited by a primary X ray

source is an extremely useful tool in the field of Cultural Heritage because allows non-invasive and rapid analysis without any damage of sample. Moreover, with portable instrument, it allows in situ measures and instant elemental analysis.

The disadvantages of this technique are the low measurement depth and the impossibility to detect light elements.

In this work, the XRF measurements are carried out using a highly performing portable device, developed at the Institute for Technologies Applied to Cultural Heritage (ITABC) of National Research Council [19].

The system is equipped with an X-ray tube, working at 60 kV, 1.5 mA, the detector is Peltier-cooled a Si-Drift produced by Ketek (area = 10 mm^2, thickness= 450 μm, FWHM = 165 eV at 5.9 keV) and the spot diameter at the measurement point is about 2 mm.

Quantitative analysis are carried out by the fundamental parameter software package PyMCA [26], using the K-lines of Cu and Ag and the L-lines of Pb.

In the usual working conditions of the tube (60 kV, 1.5 mA), the detection limits are about 30 ppm for Ag, Sn and Sb and 200 ppm for Pb and Bi at 95% confidence level.

Figure 5.1 shows the lay-out of the instrument and Figure 5.2. shows a picture of set up used.

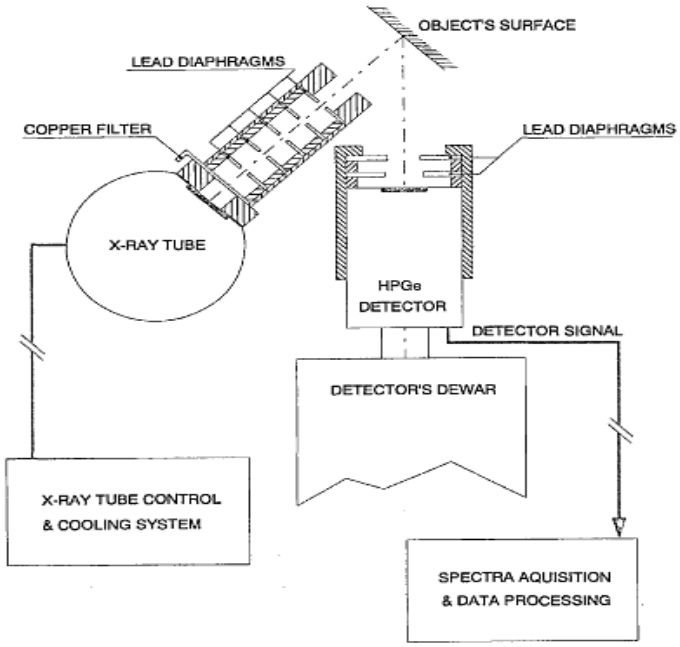

Fig. 5.1.: Scheme of XRF set up [23]

Fig. 5.2.: Picture of XRF set up used for archaeometric analysis

5.2.2. micro – Raman spectroscopy

The Raman spectroscopy is a non – destructive technique that does not require a complex sample preparation. This technique is based on the interaction between a laser source and a sample. After this interaction, the scattered radiation is measured through a detector positioned at 90° or 180° with respect to the optical path along the sample. The scattered radiation can have the same energy (Rayleigh scattering), less energy (Stokes scattering) or more energy (anti – Stokes scattering) with respect to the incident radiation. The Rayleigh radiation is due to an elastic scattering; the Stokes signal is due to an interaction which determines the energy transfer from the radiation to the sample molecules, which are so involved in an energetic transition to a more excited state. The anti – Stokes radiation is determined by the energy transfer from the molecule which passes from an excited energy level to a less energetic one. The molecular levels involved in the transition are the vibrational – rotational levels. The micro – Raman spectroscopy is an analytical technique which allows to study a localized area of the sample: thanks to an optical microscope it is possible analyze a sample area of the order of the square microns, allowing to investigate sample obtained from micro – sampling or to characterize heterogeneous structures with a

high spatial resolution. In this work, it was used an integrated micro – Raman spectrophotometer LabRam HR, HORIBA JobinYvon.

In this instrument, the radiation source is a He – Ne laser having a wavelength of 632.8 nm and a power of 20 mW. The detector is a CCD device, which was cooled exploiting the Peltier effect. The system is equipped by a x, y motorized translation stage.

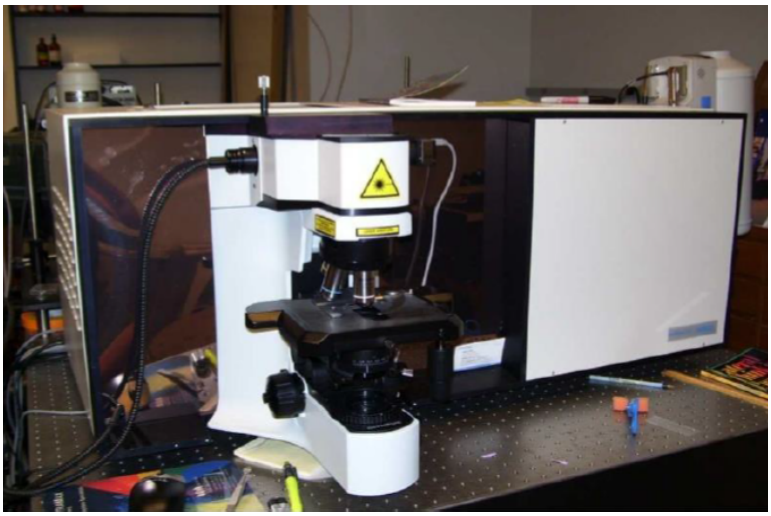

Fig. 5.3.: LabRam HR, HORIBA JobinYvon

5.2.3. Energy dispersive X-Ray Spectroscopy (EDX)

The EDX system employed was the INCA 300 Oxford (figure 5.4).

Energy Dispersive X – ray Spectroscopy (EDX) is an analytical technique which can be coupled with several imaging tools as SEM and TEM. With EDX analysis it is possible to have elemental information about an area of the order of nanometers. This technique is based on the interaction between an electron beam and the sample, which determines the ejection of X-rays which are characteristic of the elements present in the sample.

The x-ray intensity is proportional to the amount of emitting atoms of the same species. For this reason, EDX analysis allows to obtain both qualitative and quantitative information.

Fig. 5.4.: EDX INCA 300 Oxford.

5.3. Torre di Satriano site

5.3.1 Archaeological samples

The archeometric studies are carried out on six bronze objects, coming from Torre di Satriano site, that is a very important archaeological site in Southern Italy [27].

The “Torre di Satriano” archaeological site is situated in Basilicata in an area between the towns of Tito and Satriano di Lucania, in the heart of the Lucanian Apennine.

The name derives from the Norman tower of Medieval Satrianum, that is located in a strategic position for the control and defense of the land.

Since 2000, thank to archaeological studies carried out in the territory surrounding the hilltop centre, with the collaboration of scholars from various disciplines, it has been possible both to reconstruct the development of the settlement and to perform stratigraphic excavations.

Underneath the Medieval settlement there are much earlier remains, including traces of human frequentation which date back as early as the Bronze age.

During the Bronze Age, the first colonization, defined “pre-lucanian period”, has showed the presence of different settlements, basically linked with seasonal groups, that are organized in nuclei of huts and near burials.

After this period, the area has showed the existence of another ancient settlement, dating from middle of VIII century B.C. to II century B.C. described as "lucanian period". An archaic monumental building has been discovered in 2008 and can be interpreted as the centre of power within the local community.

This particular building presents exceptionally characteristics for size, construction technique as well as for the objects found inside, that testify its extraordinary importance. Not far from the building a small necropolis and a manufacture area have been brought to light.

This building was suddenly destroyed, most likely due to a seismic event, but returned extraordinary interior decoration, preserved in an exceptional way.

After a long time off, during the Lucanian period, the settlement pattern has showed up a substantial modification in the organization.

On the one hand, the hilltop of Torre di Satriano becomes a fortified central place, whereas, in the surrounding areas, there are a number of farmsteads.

Thanks to the favorable geographical position, this site had a central role in commercial trade and was an ideal place for agriculture.

Finally, the third stage of the settlement concerns the ancient medieval city of Satrianum, of which the "tower" represents only one of the buildings of an impressive complex, including medieval houses and a cathedral situated on the summit.

The intense archaeological research, involving both “Basilicata Archaeological Bureau” and University of Basilicata, has been brought to light the original structure of the archaic monumental building (Fig.5.5.) of the VII century B.C. and a double wood door of about 2.30 mt high (Fig.5.6.), which was placed inside the large central hall [28].

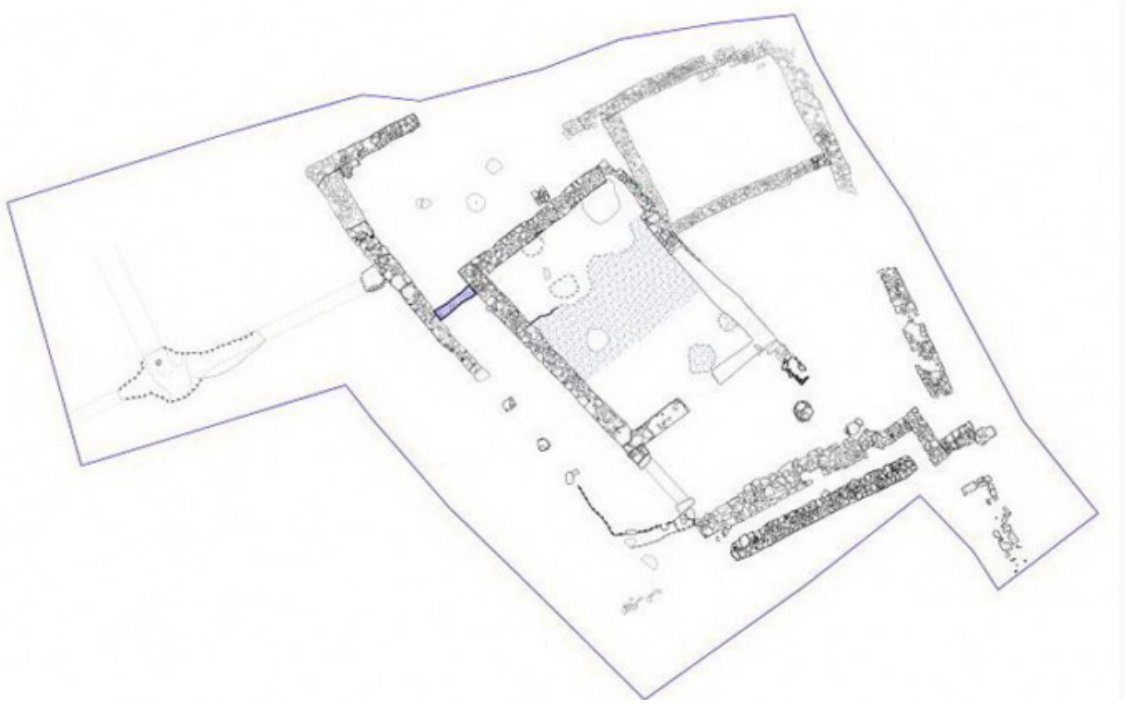

Fig. 5.5.: Planimetry of the ancient building

From the archaeological reconstruction, this door presents sumptuous bronze applications: a large bronze cast iron handle, a leonine protome shutter with open wide jaws, and finally a gryphone's protome of fused bronze with wings in cantilever plate and iron fixing pin.

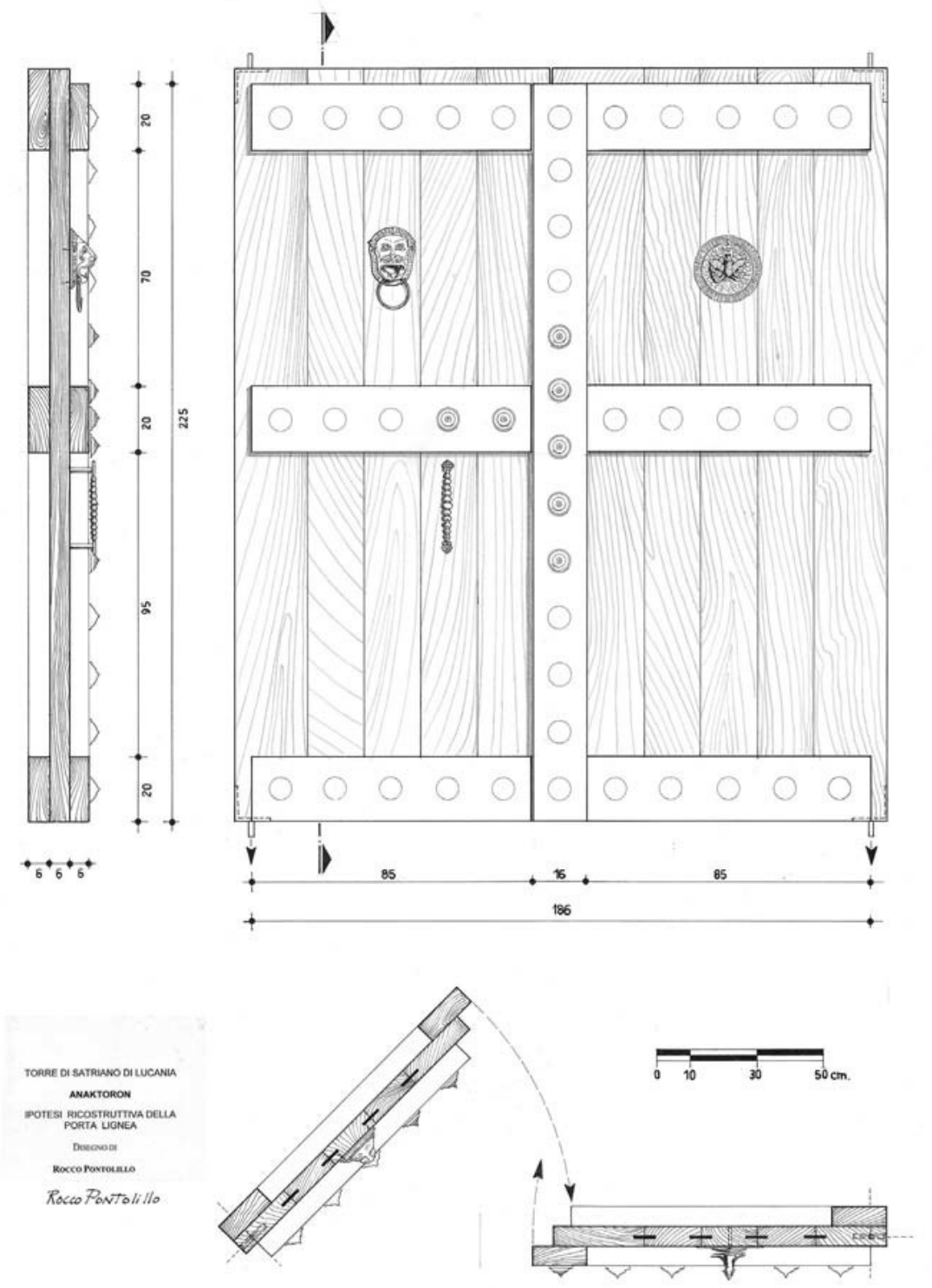

Fig. 5.6.: The double door reconstruction hypothesis

Fragments from these decorations and from bronze baskets are analyzed in this work.

These samples present a very thick corrosion patina and appear strongly inhomogeneous.

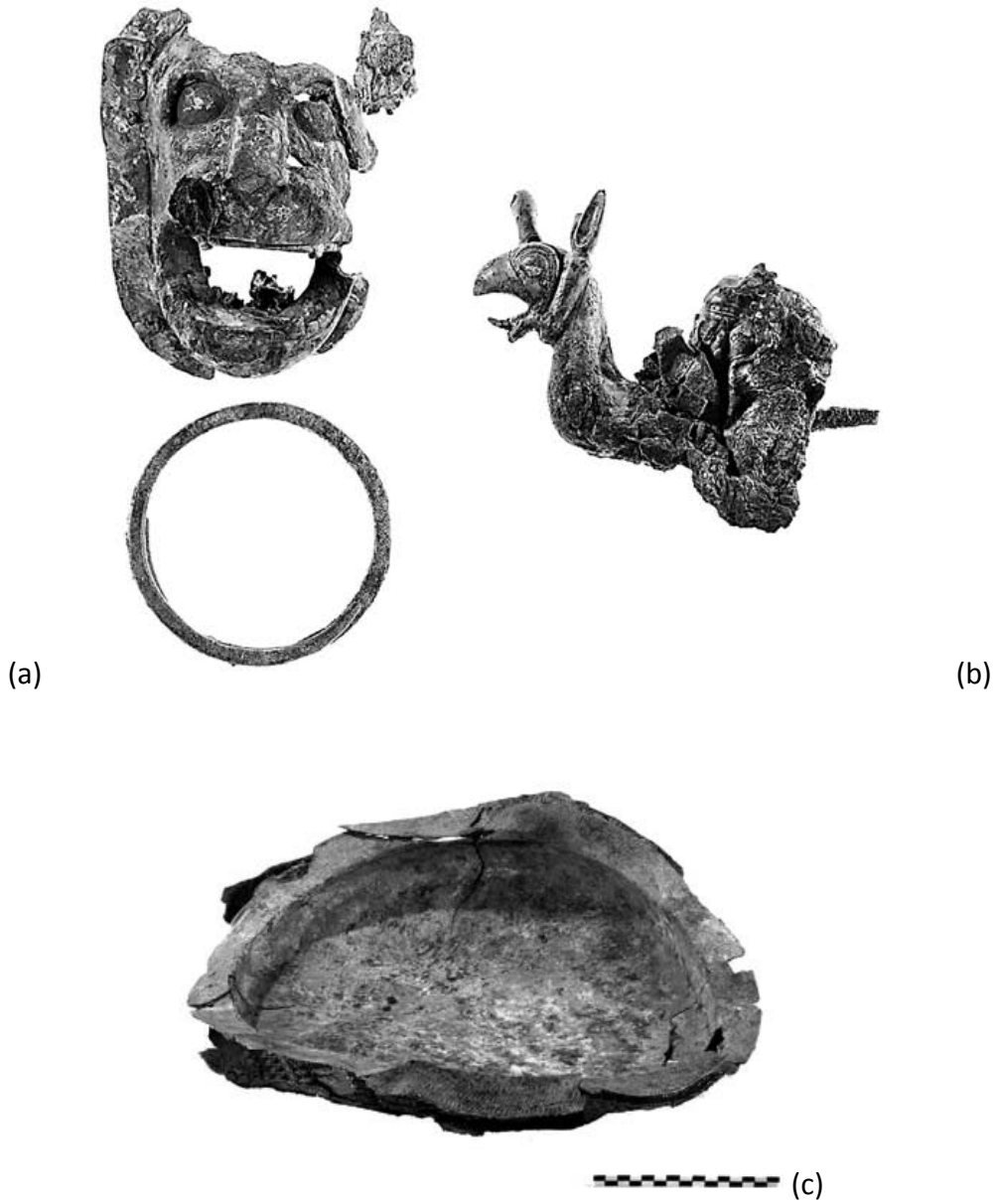

Fig 5.7.: leonine protome (a) Griffon's protome (b) and Basin (c)

In Fig. 5.8. the pictures of the archaeological samples, dating VI century B.C., are show.

Sample 1 – Griffon – n. 410000

Sample 2 – Griffon – n. 1349

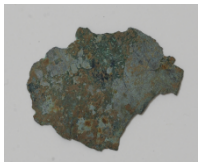

Sample 3 – Basin – n. 409695

Sample 4 – basin - 410001

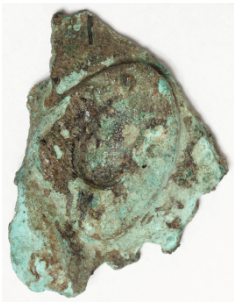

Sample 5 – Lion – n. 1370

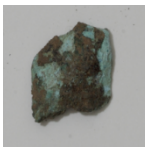

Sample 6 – Lion – n. 409909

Fig. 5.8.: Archeological finding analyzed coming from Torre di Satriano site

5.3.2. Experimental methodology

The aim of this work is applying the CF inverse LIBS method to the analysis of a set of ancient bronze samples in order to confirm the validity of method.

One of the advantages of LIBS in archaeological field is the simple or no sample preparation, compared to conventional techniques, that generally does not require additional chemical compounds or solvents and, consequently, the analysis remains environmentally friendly.

In this case, the analysis on archaeological samples are made without any type of preparation.

The approach used in chapter 4 has demonstrated that the temperature determined for a standard bronze sample can be assumed also for unknown samples with similar matrix, using obviously the same experimental conditions.

For this reason the ablation conditions have been replicated for the analysis of these archaeological samples.

The parameters of the laser are the same whereas the number of laser pulses are incremented in order to remove the external layers of the corrosion patina and to ablate a sample layer as representative as possible of the sample bulk.

In Table 5.1. the LIBS experimental condition for quantitative analysis are reported:

Fs energy laser	3.0 ± 0.1 mJ
Fluence laser	1.5 ± 0.1 J cm^{-2}
Delay time	200 ns
Gate time	500 ns
Laser pulses	150

Table 5.1.: LIBS Experimental conditions (Torre di Satriano site)

The archaeological samples are kept fixed to limit their damage, but, in order to take into account the possible composition inhomogeneity, each experiment is carried out by averaging acquisitions from five different points on each sample.

In this case, the emission spectral lines are choose among those used for standard samples, reducing the number, in order to limit damage, and selecting the most appropriate on the base of spectral characteristic (Table 5.2.).

ELEMENT	λ(nm)	E_u (eV)	E_{ul} (eV)	g_u	A_{ul} (s^{-1})
Cu I	301.08	5.506	4.117	6	$1.298 \cdot 10^6$
	303.61	5.725	4.083	4	$2.428 \cdot 10^6$
Ni I	300.36	4.235	4.127	5	$6.912 \cdot 10^7$
	301.20	4.538	4.116	5	$1.340 \cdot 10^8$
	303.79	4.105	4.080	7	$2.842 \cdot 10^7$
Pb I	280.20	5.744	4.424	7	$1.081 \cdot 10^8$
	282.32	5.711	4.391	5	$3.044 \cdot 10^7$
Sn I	300.91	4.329	4.119	3	$3.714 \cdot 10^7$
	303.41	4.295	4.086	1	$1.513 \cdot 10^8$
Zn I	307.21	8.113	4.035	3	$1.702 \cdot 10^7$

Table 5.2.: Spectroscopic constant of the electronic transitions employed

Also in this case, the spectral assignment are performed using the atomic spectral NIST database or the Kurucz database [29], [30]. Data processing and area measurements are made with Origin Pro software (Origin Pro 6 1991–2007 Origin Lab Corporation) using Voight fit, after subtracting the background emissions from the integrated line intensity.

An example of LIBS spectrum of the bronze sample including labelling of the analyzed peaks is shown in Fig. 5.9.

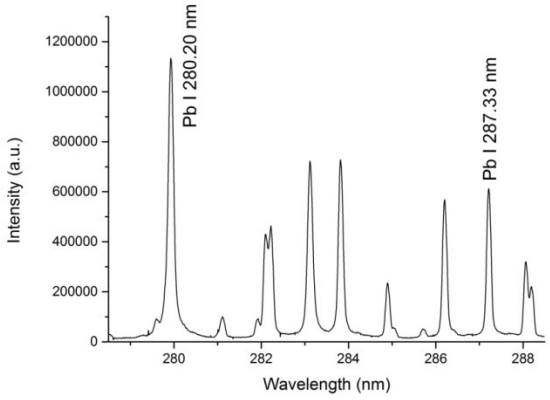

Fig. 5.9.: LIBS spectrum between 278,5 nm and 288,5 nm

The LIBS compositional analyses are compared with another elemental analyses, performed by XRF using a X ray current of 1.5 mA and a Voltage of 60 kV.
In this case, three different spots are analyzed for each sample.

5.3.3. Results and discussion

The data obtained using the CF inverse method are showed in the following Table 5.3.

	Element	Experimental wt%
Sample 1 – Griffon n. 410000	Cu	85 ± 4
	Pb	1.0 ± 0.3
	Sn	14 ± 4
Sample 2 – Griffon n. 1349	Cu	88 ± 4
	Pb	0.5 ± 0.1
	Sn	12 ± 3
Sample 3 – Basin n. 409695	Cu	91 ± 4
	Pb	0.17 ± 0.05
	Sn	9 ± 3
Sample 4 – Basin n. 410001	Cu	92 ± 4
	Pb	0.8 ± 0.2
	Sn	8 ± 2
Sample 5 – Lion n. 1370	Cu	84 ± 4
	Pb	0.19 ± 0.05
	Sn	16 ± 4
Sample 6 – Lion n. 409909	Cu	73 ± 4
	Pb	1.2 ± 0.3
	Sn	26 ± 7

Table 5.3.: wt% experimentally evaluated of each element present in bronze archaeological samples

Comparing LIBS results with XRF ones, all samples show a great disagreement, indeed in the latter case, tin appears strongly overestimated (Fig. 5.10.).
However, because of bad state of conservation and a complete mineralization present in some objects analyzed, the compositional XRF data are not representative and differ completely from the bulk concentration.

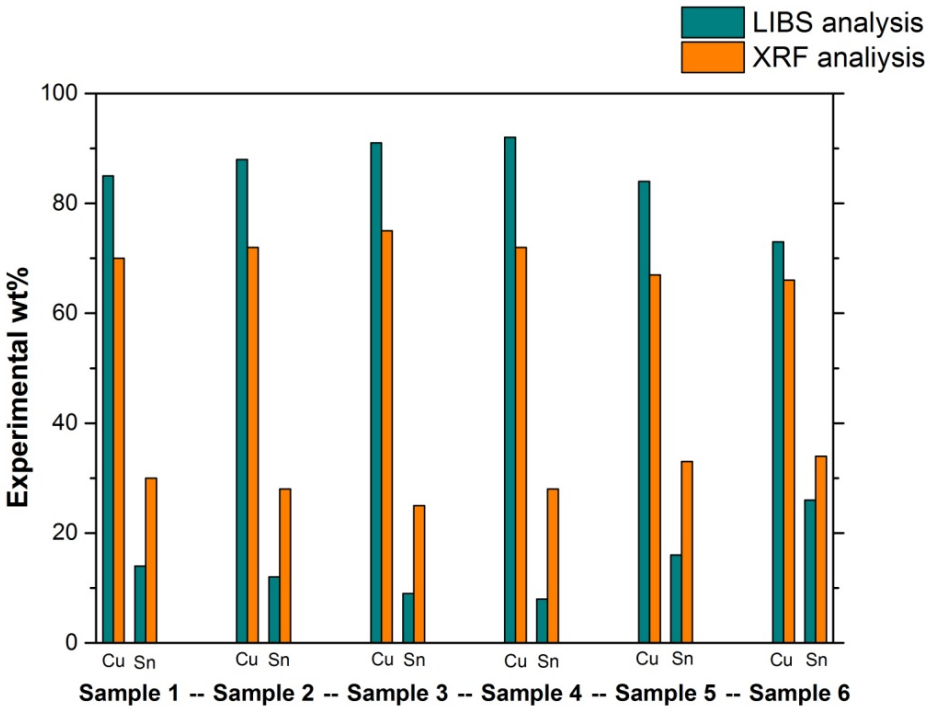

Fig. 5.10.: Comparison between wt% of copper and tin in bronze archaeological samples performed by LIBS and XRF analysis

For all samples, the tin concentration, obtained with XRF analysis, is in the range between 25 – 30% weight percentage.

These values are completely out of the range of validity for the bronze alloys [31] and are linked to the copper selective dissolution that cause its content reduction, and consequent a tin enrichment in the outermost layers of the coating.

The difference between XRF and LIBS analysis can be correlated with different sampling depth of these two techniques.

The analytical XRF signal, namely the characteristic X-rays of the constituent elements, originate mostly from a thin surface layer extending to about 10 µm, depending on the matrix composition and the detected X-ray energy so, for corroded samples like these, only information about degraded surfaces can be obtained.

In this case, it has been tested that XRF technique is not useful for compositional analysis.

On the contrary, LIBS allows to make analysis layer by layer and, consequently, it is possible to obtain measurements of composition profiles up to the real composition of the bulk sample.

Anyway, with combination of LIBS and XRF results, very interesting archaeological data have been obtained.

LIBS quantitative analysis have showed difference in tin concentration that can be correlated with different manufacturing processes, classifying the fragments into two groups: samples from the basins in which tin is less than 10% and the samples of lion and griffon in which tin is more than 12%.

This information can be used to assert the high technical and metallurgical technology of that ancient period.

Also it is very interesting to note the compositional information obtained by XRF: basin and lion present the same pattern of trace elements which would suggest a common origin of raw copper.

The chemical composition of this set of bronze objects, including both major and trace elements, is reported in Table 5.4.

		Major and minor elements	**Trace elements**
Griffon	Cu	86 ± 4	Pb
	Sn	12 ± 3	
	Pb	0.5 ± 0.1	
Lion	Cu	78 ± 4	Fe, As, Ag, Sb, Pb
	Sn	16 ± 4	
	Pb	0.19 ± 0.05	
Basin	Cu	91 ± 4	As, Ag, Sb, Pb
	Sn	9 ± 3	
	Pb	0.17 ± 0.05	

Table 5.4.: Compositional analysis of bronze archaeological samples

From an archaeometrical point of view, the determination of the chemical composition may help to elucidate the evolution of manufacture technology and the knowledge at ancient time so these analysis allow to affirm a good manufacturing knowledge for the

ancient period: different manufacturing techniques (melting and/or hammering processes, annealing and cold working) have been used for obtaining artefacts with desired shape.

The increase of tin concentration improve the ductility and malleability of the alloy so a higher tin percentage has allowed casting working methods for lion and griffon, whereas a lower tin content has been used for basins that are worked by forging with cold hammering.

As said previously, one feature that is unique to LIBS is the possibility of performing depth profile analysis of multilayered samples.

In this work depth profile analysis are performed by femtosecond LIBS on a fragment of basin sample, comparing the results with those obtained with nanosecond one.

From data obtained, it is noted that, using fs laser, also the presence of the external copper layers on the surface can be detected, confirming the advantage of fs depth profiling [32].

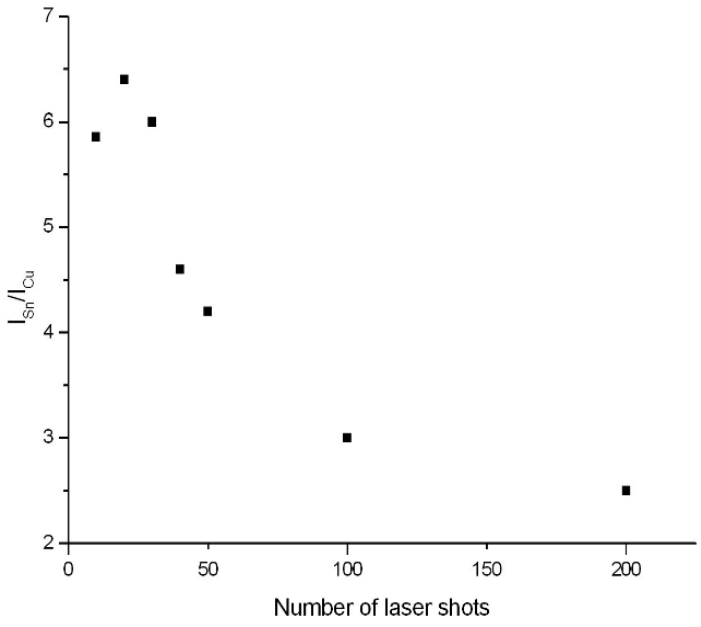

(a)

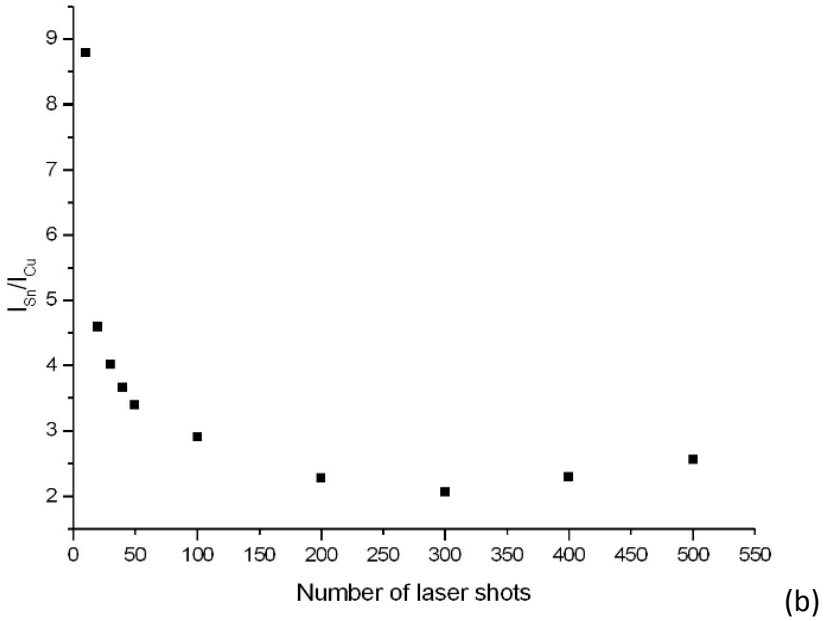

(b)

Fig. 5.11.: Depth profile performed by fs laser (a) and ns laser (b) on bronze sample n. 410001

Nevertheless, for the fs depth profiling more than 200 laser shots cannot be revealed probably due to lower intensity of plasma signals and its confinement within the crater. Moreover, the different laser – matter interaction induced by the different time duration of the laser pulses is confirmed also in the following images (Fig. 5.12.) that show two OM magnification of the crater obtained by 100 fs laser shots and one by 100 ns laser shots on sample n. 410001.

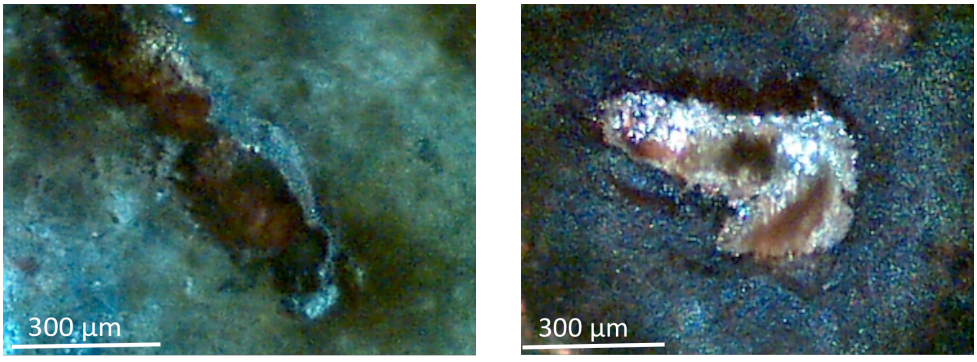

(a) (b)

Fig. 5.12.: OM magnification of crater obtained by 100 fs laser shots (a) and one by 100 ns laser shots (b) on sample n. 410001.

Using fs laser, trace of melting are not present around the crater, instead with ns laser the patina has been removed around crater because the interaction is based on heat diffusion, as explained in chapter 1.

Finally, in order to complete the description of these samples, the corrosion surface patinas are studied by micro Raman spectroscopy for distinguish the type of corrosion patina.

Because of inhomogeneity of sample surfaces, the patina can be different for the various objects and may change even within the same object.

The presence of several copper corrosion products on the artefacts surface has been revealed and it has been proved that different colours on the patina correspond to different corrosion products.

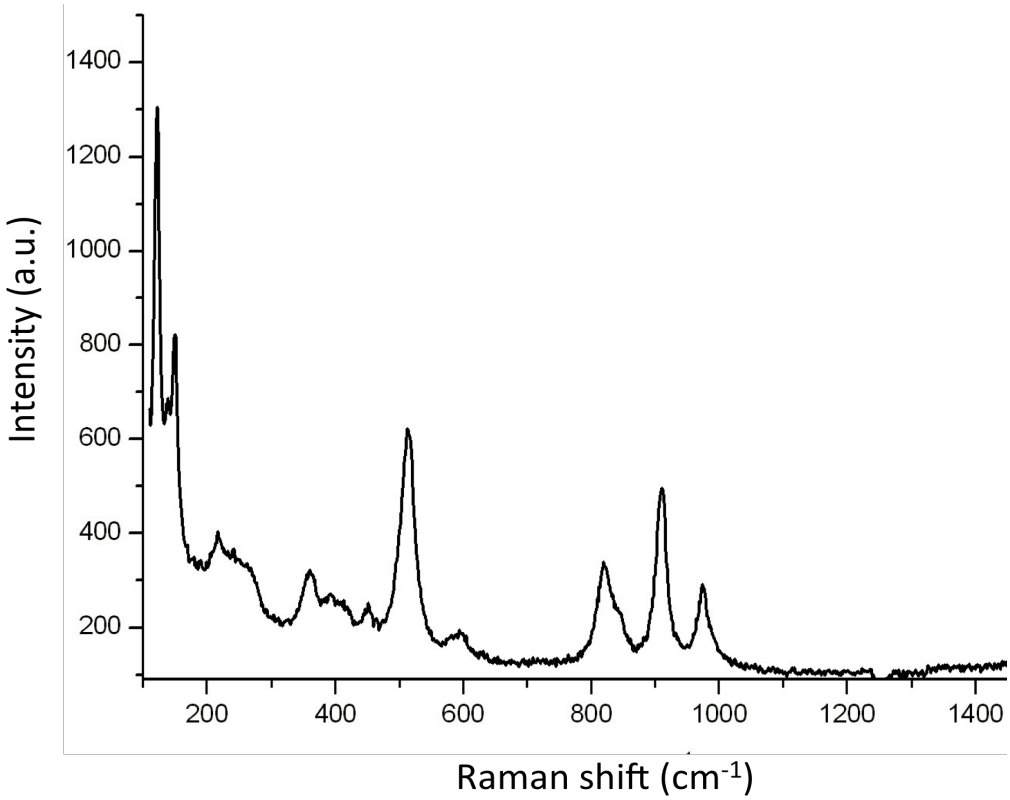

Fig. 5.13.: Raman spectrum of atacamite – light green area – sample n. 409695

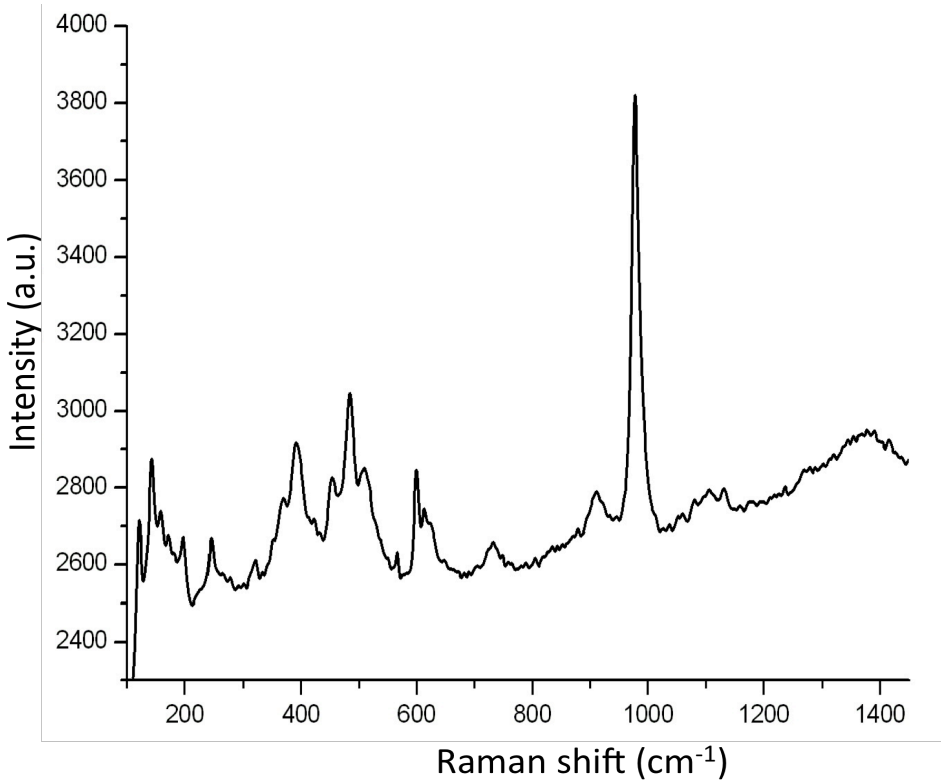

Fig. 5.14.: Raman spectrum of brochantite – dark green area – sample n. 409695

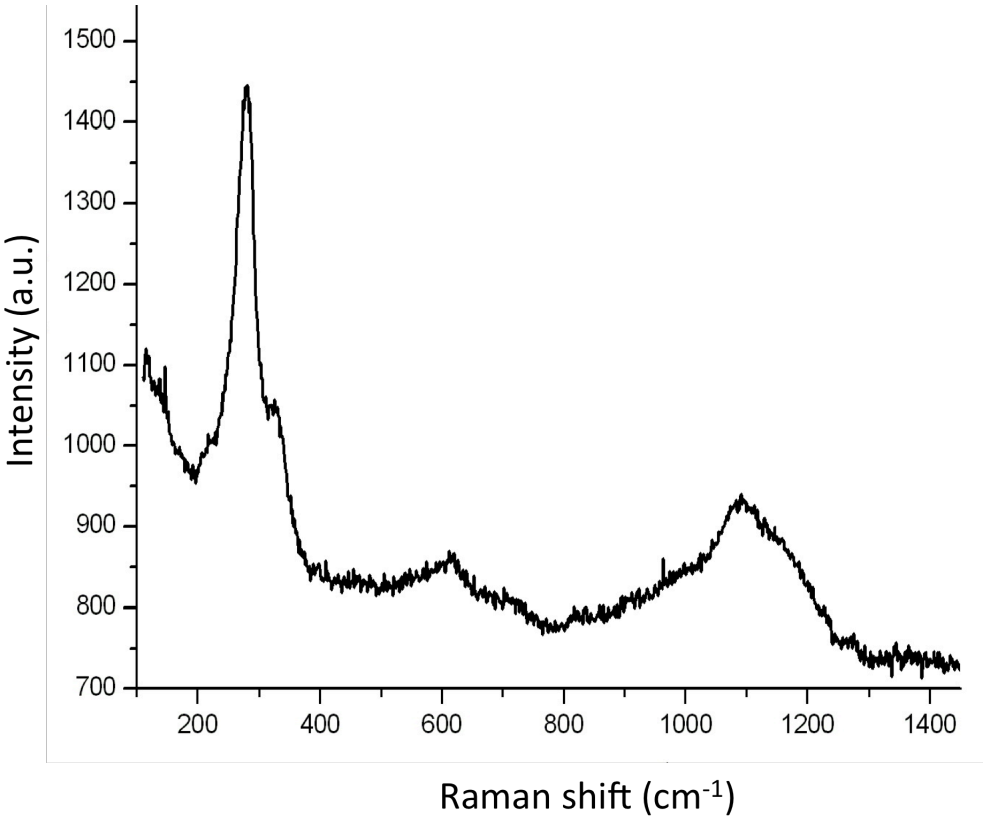

Fig. 5.15.: Raman spectrum of cuprite – brown red area – sample n. 409695

Moreover a greater damage from corrosion has been observed where the stress from hammering is more concentrated.

In conclusion CF IM LIBS appears as a suitable candidate for archaeological samples as a fast micro-destructive method for quantitative determination of major and minor elements.

On the contrary, the XRF analysis do not allow to get good compositional data for corroded ancient copper alloys.

However, the use of integrated technologies allowed us to determine both the elemental composition and surface morphology.

5.4. Corleto Perticara site

5.4.1. Archaeological samples

During the works for oilfield construction in Corleto Perticara, Basilicata, some interesting archaeological sites have been discovered.

The archaeological researches have been carried out since 2009 and over 500 fragments have been found in three different necropolis, including some bronze headgear, many precious objects like amber necklaces and votive statues

However, the site is still object of study so no archaeological papers are available in literature.

The following pictures show the bronze samples analyzed (Fig.5.16.)

Sample 1 – Situla;

Sample 4-5 –Stamnos;

Sample 10 – patera;

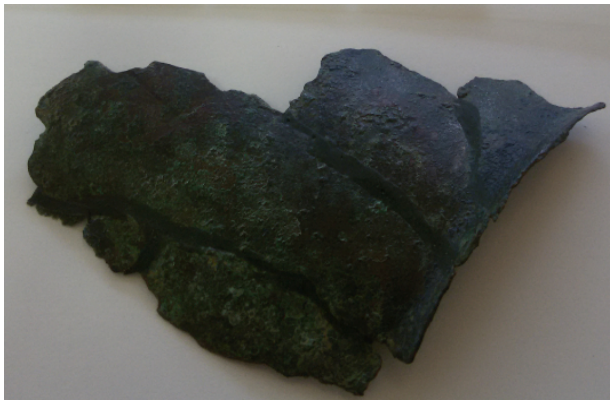

Sample 12 - unknown sample;

Sample 33 - basin;

Fig. 5.16.: set of bronze samples analyzed coming from Corleto Perticara site

5.4.2. Experimental methodology

The same multi techniques approach used previously has been adopted for this set of archaeological bronze, that, unlike those from Torre of Satriano site, present a better state of conservation and have undergone restorative treatments.

LIBS spectroscopy is used to determine the main components of alloys, i.e. Cu, Sn and Pb while the XRF spectroscopy for trace components.

The feasibility of CF inverse LIBS approach is demonstrated by comparing its results with those obtained by classical LIBS and again by independent analysis, performed by XRF technique.

The micro-Raman spectroscopy is used to analyze the composition of bronze corrosion patina.

The LIBS experimental conditions used are the same exposed in Table 5.1., the emission lines considered for LIBS analysis are reported in Table 5.2. and the value of 9500 K is used as electron temperature.

Also for XRF analysis are used the same experimental conditions exposed in section 5.3.2.

5.4.3. Results and discussion

- **Archaeological finding 1**

From the LIBS analysis, this object consists of an alloy containing 89.1% copper and 10.9% tin. The lead is present in quantities below the limit of quantification (LOQ) of the technique (0.01%).

The XRF has show the presence, as trace elements, of antimony, arsenic, silver and lead. In the micro-Raman analysis, the patina is formed by malachite (Fig.5.17).

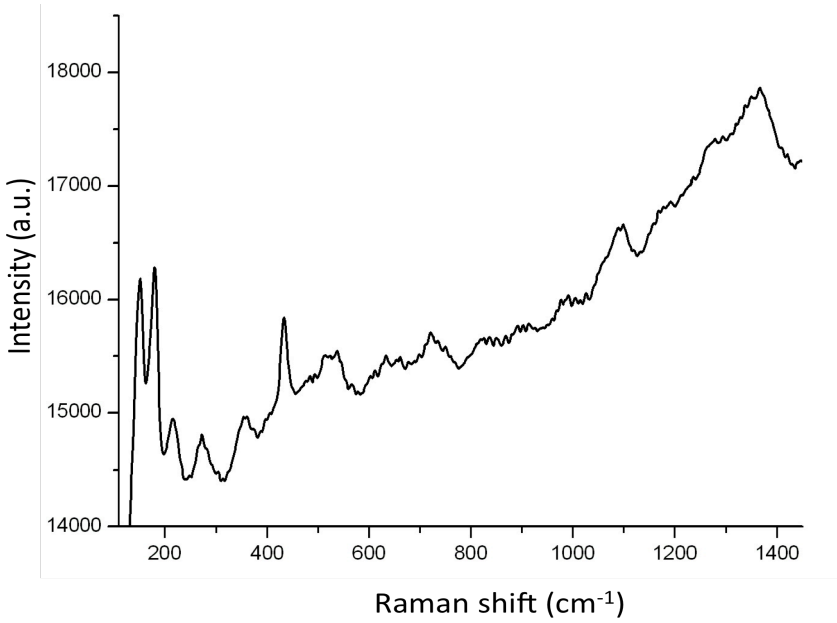

Fig. 5.17.: Raman spectrum of malachite – dark green area – sample n.1

- **Archaeological finding 4-5**

From the LIBS analysis, the findings 4-5 are composed of a alloy containing 89.8% copper and 10.2% tin. Again, lead is present in quantities below the limit of quantification.

The trace elements, detected by XRF analysis (Fig.5.18), are antimony, arsenic, silver, lead and iron. The patina, analyzed by micro-Raman, shows the presence of malachite and azurite.

Furthermore, It should be noted that the Raman analysis show also the presence of hostasol green pigment (Fig. 5.19), a commercial synthetic product, clearly related to restoration treatment.

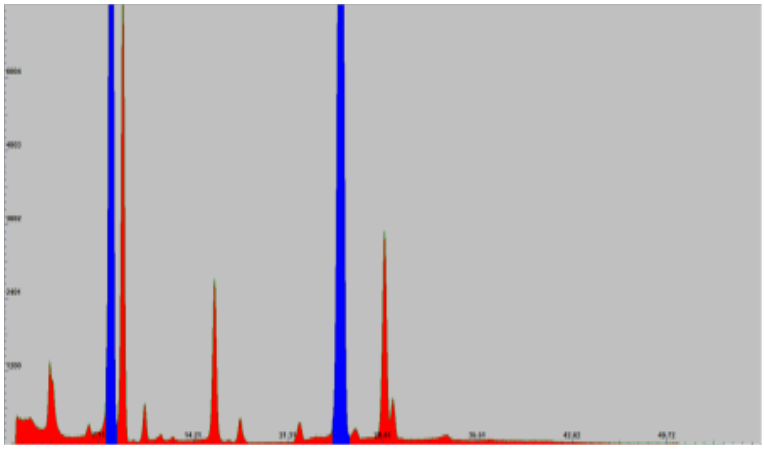

Fig. 5.18.: XRF spectrum of sample n. 4-5

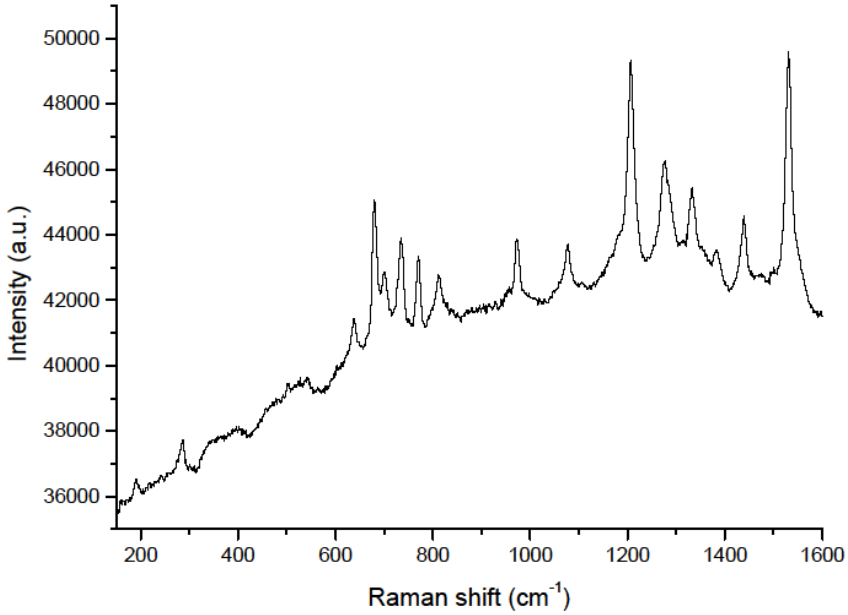

Fig. 5.19.: Raman spectrum of hostasol green – brown red area – sample n. 4-5

- **Archaeological finding 10**

From the LIBS analysis, the alloy of sample 10 contains 82.2% copper and 17.8% tin. Again, lead is present in quantities below the LOD.

The trace elements detected by XRF are antimony, arsenic, silver and lead.

Also in this case, the patina is formed by malachite.

- **Archaeological finding 12**

This sample represents an exception respect to the set because results in an alloy containing 88.6% copper and 11.4% tin without the pattern of trace elements found in the other samples.

The lead is completely absent and only arsenic has been found as a trace element by XRF (Fig.5.20). The micro-Raman analysis has reveal the present malachite on the sample surface.

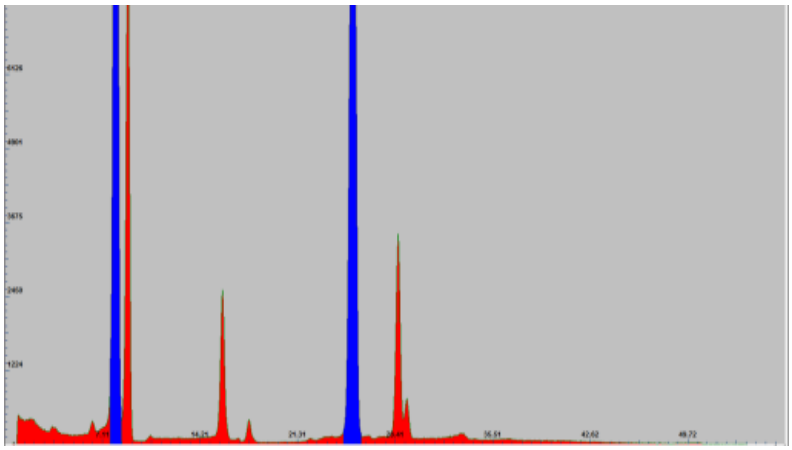

Fig. 5.20.: XRF spectrum sample n. 12

- **Archaeological finding 33.**

From the LIBS analysis, the chemical composition of finding 33 is made of 85.7% copper, 12.7% tin and a greater concentration of lead, about of 1.6%.

The XRF has recorded the presence, as trace elements, of silver and bismuth. In the micro-Raman analysis, the patina is formed by malachite.

The LIBS data, obtained by CF inverse method are compared with classical LIBS and XRF analysis. In the following table (Table 5.5.) are summarized the data obtained:

		CF – IM LIBS	CC LIBS	XRF	Trace elements (XRF)
REP 1	**Cu**	90 ± 4	89 ± 2	84.2	Sb, As, Ag, Pb
	Sn	9 ± 2	11 ± 2	15.4	
	Pb	0.5 ± 0.1	0.2 ± 0.1	0.4	
REP 4 – 5	**Cu**	93 ± 4	90 ± 1	88.3	Sb, As, Ag, Pb, Fe
	Sn	7 ± 3	10 ± 1	11.4	
	Pb	0.4 ± 0.1	< LOQ	0.25	
REP 10	**Cu**	88 ± 4	82 ± 3	87.7	Sb, As, Ag, Pb
	Sn	12 ± 3	18 ± 2	11.9	
	Pb	0.4 ± 0.2	< LOQ	0.3	
REP 12	**Cu**	91 ± 3	89 ± 1	89.5	As
	Sn	9 ± 2	11 ± 1	10.5	
	Pb	-	-	-	
REP 33	**Cu**	88.5 ± 3	86 ± 1	82.2	Ag, Pb, Bi
	Sn	10 ± 1	12.7 ± 2	12.9	
	Pb	1.5 ± 0.5	1.3 ± 0.4	4.9	

Table 5.5.: Compositional results obtained with CF inverse and CC LIBS and XRF on bronze archaeological sample

From these analyses some preliminary archaeometric considerations can be drawn.

All the samples have a tin percentage in the order of 10-12%, compatible with the typical bronze worked by hammering.

Only the sample 10 has a higher percentage of tin (17.8%) probably due to migration processes related to corrosion.

Consistent with the type of bronze examined, lead is present in small quantities or completely absent (object 12).

Furthermore, the analysis of the trace elements performed by XRF shows the same trace elements (antimony, arsenic, silver, lead) for findings 1, 4-5, and 10. This result seems to indicate a common copper origin of the three alloys (probably the presence of iron may be due to contamination).

The other two samples show remarkable differences. In the case of sample 12 the only trace element present is arsenic, while the sample 33 contains the bismuth, an element not frequent in the copper alloys.

These features clearly differ from the last two findings that are likely to come from copper pieces of different origin than the findings 1, 4-5, and 10. The sample 12 represents an exception in the set since it seems to derive from of high purity copper alloy.

From analytical point of view, the quantitative measurements on the three main elements Cu, Sn, and Pb show a satisfactory agreement between the two series of LIBS data for all the samples, confirming the validity of the CF inverse method and also the agreement between the LIBS and XRF technique appears good.

In order to highlight the correlation between three different data sets, the quantitative results are presented also in plot, comparing the XRF data with those of two LIBS method.

The weight percentages obtained with the XRF analysis are plotted as function of the CF inverse LIBS wt% and, also of CC LIBS one (Fig.5.21).

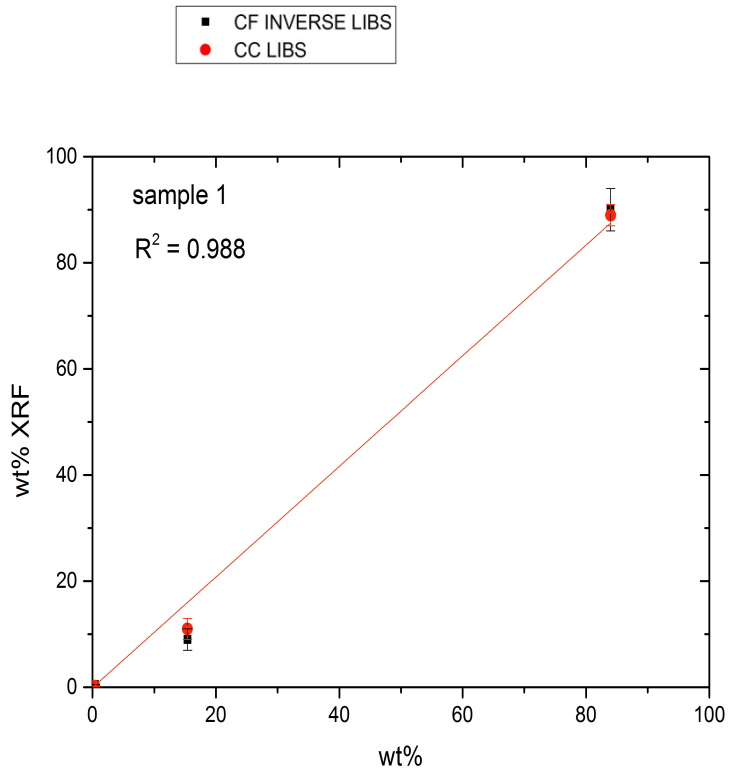

(a)

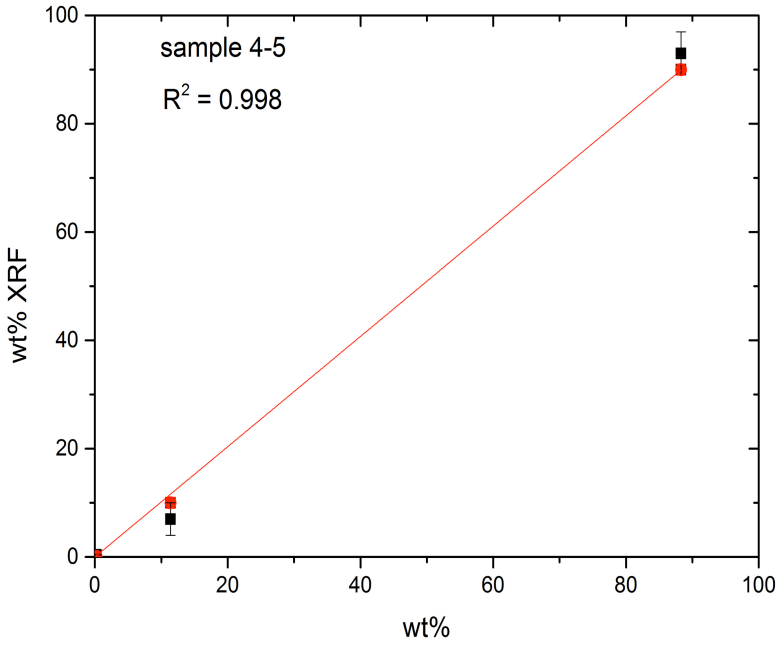
sample 4-5
R2 = 0.998
wt% XRF
wt%
0
20
40
60
80
100

(b)

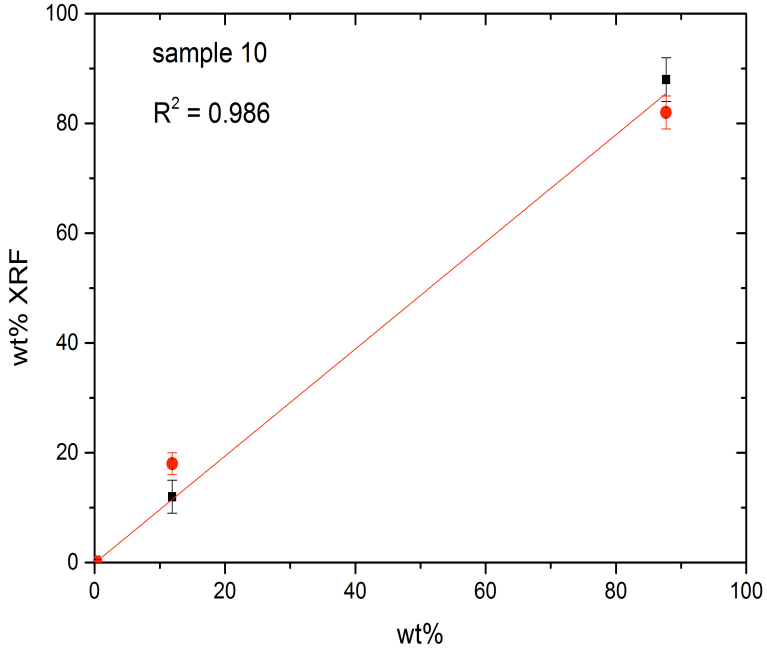
sample 10
R2 = 0.986
wt% XRF
wt%
0
20
40
60
80
100

(c)

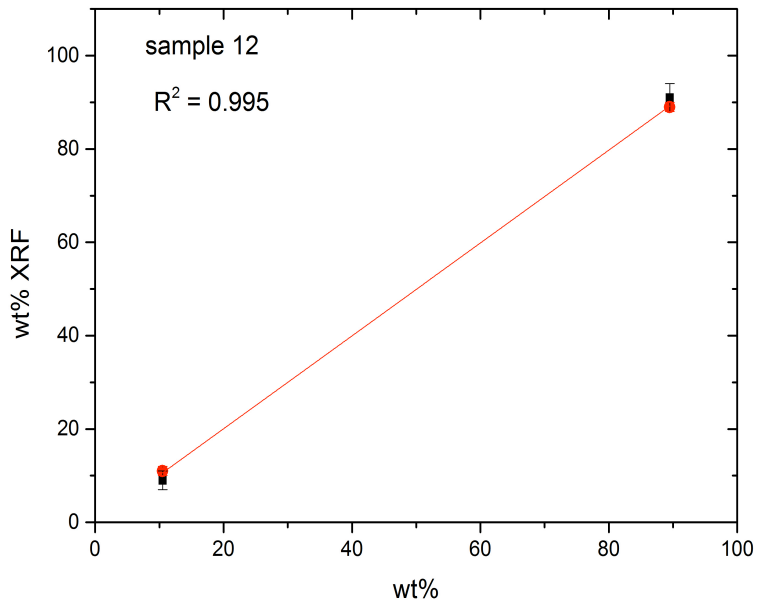

(d)

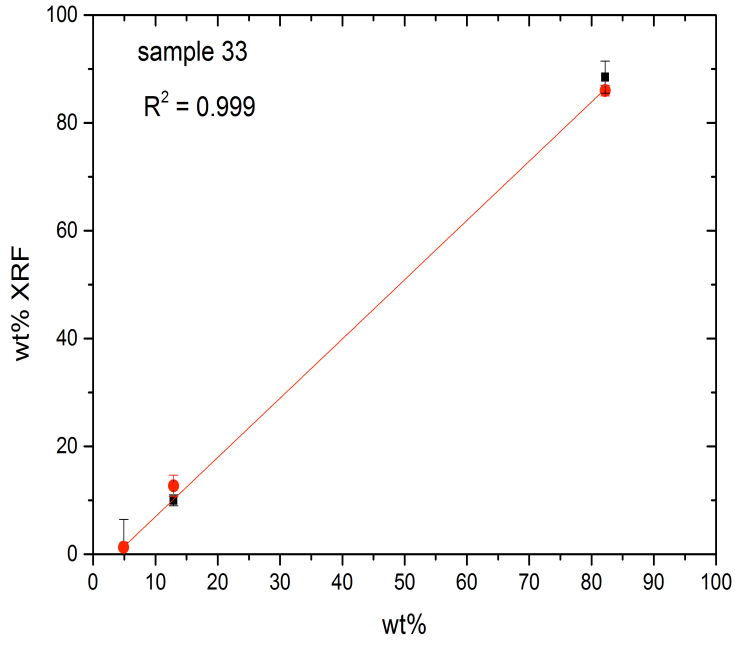

(e)

Fig. 5.21.: Correlation plots between XRF and CF Inverse LIBS and CC LIBS for sample 1 (a), sample 4-5 (b), sample 10 (c), sample 12 (d), sample 33 (e)

All the correlation plots show high correlation coefficient, very close to unity, confirming the validity of LIBS methods.

5.5. Chiaromonte site

5.5.1. Archaeological samples

Recent activities by the Archaeological Bureau of Basilicata have led to the excavation of many sites containing precious materials.

From the archaeological site of Chiaromonte, in Southern Basilicata, a sumptuous feminine parure from a necropoleis dated VI century B.C has been found, which documents the complex cultural relationships and exchanges through the fluvial valley of the Agri and the Sinni rivers.

The study of these tombs have showed a strong group organization within the community: the big tombs with a rich inventory can be defined princely, evidencing the presence of chiefs who affirm their power over family and community.

The warrior role of men is underlined by weapons while the family rank of women is emphasized with ostentation by the richness of jewellery.

The social hierarchization is manifested through rich funeral inventories and can be found in other close regions of the Mediterranean zone.

The circulation of objects coming from outside the region evidences the function of circulation between Campania, Basilicata and Calabria.

In is well-known that silver is not native to the geographical sector of Basilicata. For this reason, it is necessary to state that the raw metal has been imported, probably from Calabria's mines.

Therefore it is possible to suppose that, due to the fact that the metal necessary for production of these jewelleries had to be imported, complex relationship between different communities already existed over the course of VI century B. C.

The Fig. 5.22. show the pictures of two silver necklaces that are analysed in this work.

Both necklaces are made of a lace formed by braided threads on a cylindrical pattern and are complemented by elaborate pendants.

On the first necklace there is a silver plated pendant shaped like a scarab whereas the second presents a bud-shaped pendant with decorated leaves.

There is no know comparison for these two items, except for the construction technique used for necklace and similar items are also found in the Greek necropolis of eastern Sicily.

An important issue about these objects is the difficulty to determine a precise origin due to the lack of evidence of jewellery makers at that time from near necropolis.

Another silver object from Chiaromonte site is a fibula with pendent (Fig. 5.22).

The pictures of samples from Chiaromonte site are presented [33].

Necklace - n. 205496

Necklace - n. 211227

Fibula - n. 213149

Fig. 5.22.: Set of silver sample analyzed coming from Chiaromonte site

These precious samples are compared with a finding coming from a near archaeological site, specifically Torre di Satriano (Fig. 5.23.).

Fibula - n. 409925

Fig. 5.23.: Silver sample analyzed coming from Torre di Satriano site

The archeological sample presents similar typology and may be classified as belonging to the same group, so, by identifying similarities and/or differences, the hypothesis about the same processing can be confirmed or not.

In addition to this comparative study, also provenience studies have been also performed in order to answers the question about provenience of mineral sources.

This type of study can be conducted from evaluating the pattern of trace elements, that can be transported into the alloys in form of impurities and can be offer information related to the source of the metal used.

5.5.2. Experimental methodology

The aim of this work is to compare two types of silver objects, three coming from Chiaromonte and one from Satriano archaeological site.

Fs energy laser	2.8 ± 0.1 mJ
Fluence laser	1.4 ± 0.1 J cm^{-2}
Delay time	400 ns
Gate time	2000 ns
Laser pulses	50

Table 5.6: LIBS Experimental conditions (Chiaromonte site)

In this case, only qualitative analyses are carried out, because, sometimes, the investigation on these archaeological objects is only the comparison between material, without measuring exactly the composition [19].

It is therefore possible to identify an alloy by the signal intensity that results from repeating the measurement on different points of its surface and to compare it with other alloys by considering the difference of the data sets in terms of relative intensity

The emission lines considered for major and minor elements analysis are: λ= 309.99 nm and λ= 324,75 nm for Cu I, λ= 328.06 nm for Ag I, λ=267.60 nm for Au I.

The trace elements analyzed by LIBS are: As I (λ=245.65 nm), Sb I (λ=231.15 nm and λ=252.8 nm), Bi I (λ=306.77 nm), Br I (λ=452.55 nm), Mn I (λ=325.79 nm), Ni I (λ=301.20 nm), Pb I (λ=283.30 nm and λ=405.78 nm), Te I (λ=276.96 nm), Zn I (λ=307.59 and λ= 328.23 nm) and Al I (λ= 308.21 nm and λ=309.27 nm) [15], [34] [31].

5.5.3. Results and discussion

- **Necklace n. 205496**

The compositional analysis of necklace has been performed on the entire object, in particular, all three main components of it were analyzed: the lace, the tubular pendant and the central lamina.

The image of Fig. 5.24. shows the areas analyzed.

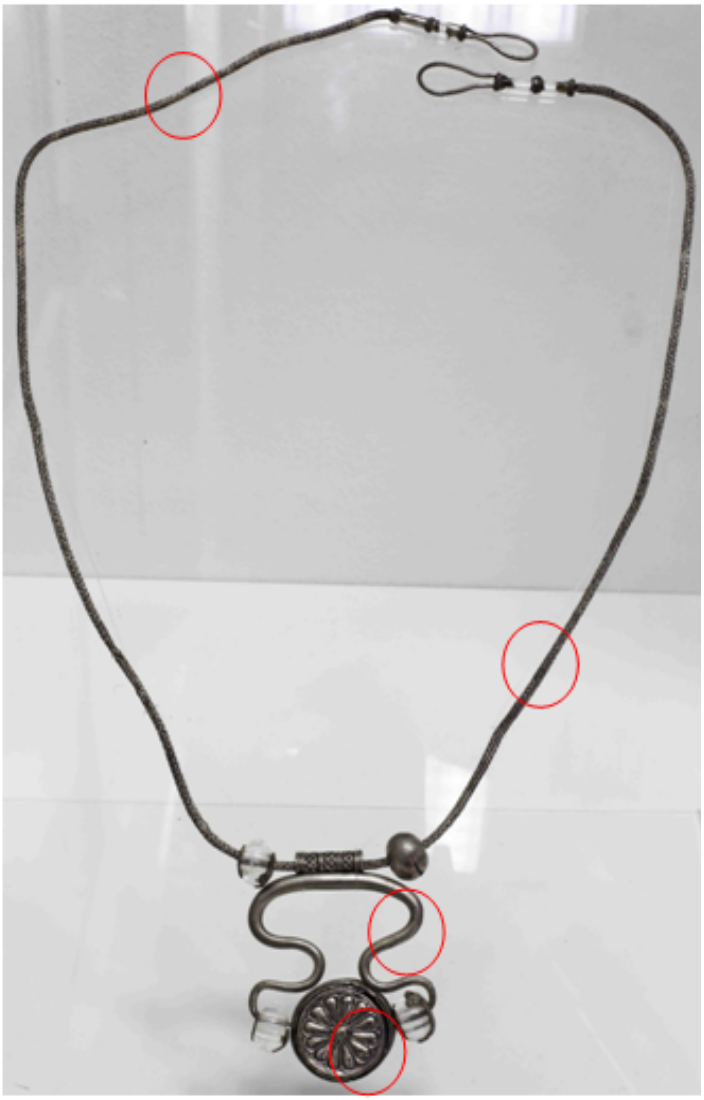

Fig. 5.24.: Necklace 205496 - areas analyzed by LIBS

The qualitative analysis shows that the ancient sample is made of a silver alloy, containing copper and gold as a minor element.

In all analyzed areas has been highlighted the presence of these three elements and, the comparable intensity of the emission signals seems to suggest that the various parts of the necklace derive from the same alloy.

- **Necklace n.211227**

The compositional analysis of this necklace also concerned the whole object, both the lace and the silver and the golden part of the elaborate pendant.
Fig. 5.25. shows the areas examined in detail.

Fig. 5.25.: Necklace 211227 - areas analyzed by LIBS

The analysis of the lace and the silver sheet revealed the presence of a silver alloy containing copper whereas the gold is present as minor elements.
The analysis of the gold leaf sheet reveals the presence of a gold alloy with silver and copper as minor elements.
Even in this case, no particular difference in compositional alloy is detected between the lace and the pendant, therefore it can be conclude that the object has been made from a unique alloy.

- **Fibula n.213149**

The Fig. 5.26. shows the another archaeological finding and the respective areas that are analyzed.

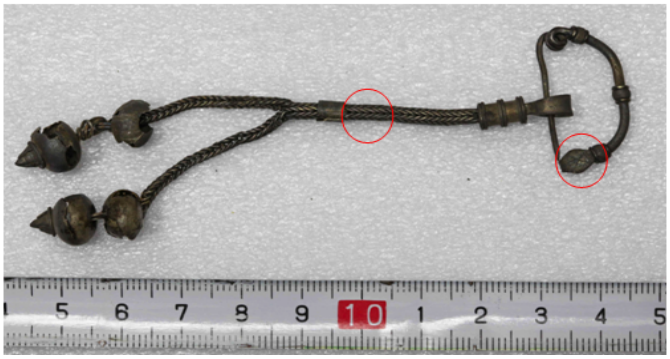

Fig. 5.26.: Fibula 213149 - areas analyzed by LIBS

The qualitative analysis showed the presence of a silver alloy containing copper whereas gold as minor element.
Although only the qualitative analysis has been made, comparing the signal intensities, it is possible to affirm by that the amount of copper in this object is greater than the other silver alloy archaeological findings.

- **Fibula n. 409925 (Torre di Satriano)**

The intensity signals of the Chiaromonte jewelleries have been compared with fibula coming from Tower of Satriano site and it is possible to exclude the same provenience for all these silver objects and to affirm that they have been processed from different alloys.
Also in this case, the LIBS analysis has been performed in various sample zone, in particular on sheet and on bracket (Fig. 5.27.).

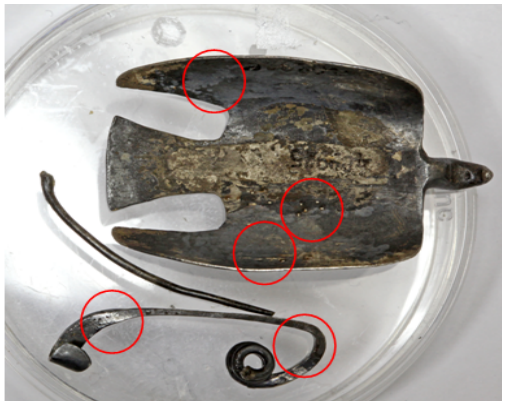

Fig. 5.27.: Fibula 409925 - areas analyzed by LIBS

In order to limit an evident damage of a precious object like this, all the measurement involved the bottom of the fibula.

The metal sheet has made of a silver and copper alloy, with silver as major element.

Furthermore, on the bracket, it has been revealed a considerable tin concentration surface, probably due to an ancient welding process.

The confirmation that the tin is not an alloy component has been obtained by performing a depth profiling analysis (Fig. 5.28.) which show initially a high tin concentration that rapidly drops until zero, as well as the layers are removed from the laser pulses.

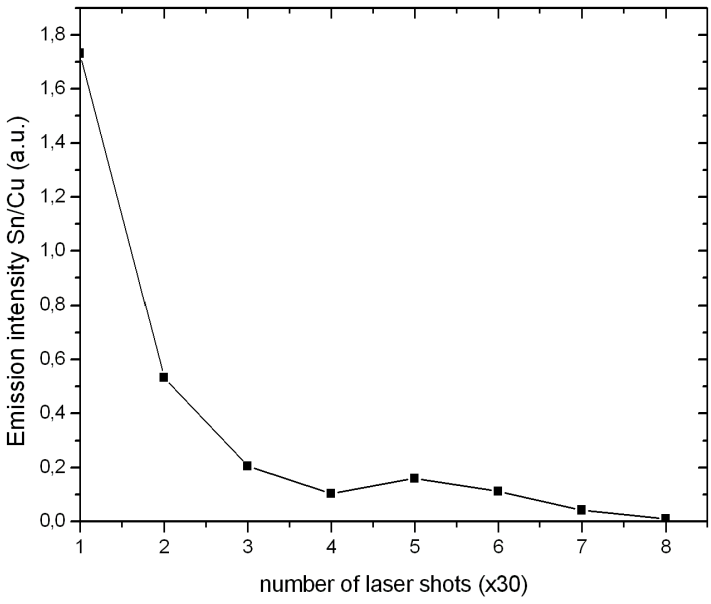

Fig 5.28.: Sn/Cu composition profile obtained by LIBS

Regarding the analysis of trace elements, the absence of all trace element searched, lead to exclude that this set of silver alloys coming from the particular mine of Longobucco, located in Calabria [35].

The aluminium and calcium are the only trace elements detected in all samples and are related to a surface contamination due to burial environment.

To confirm this hypothesis, another depth profile analysis is performed which point out that the aluminium intensity decreases during laser ablation (Fig. 5.29.).

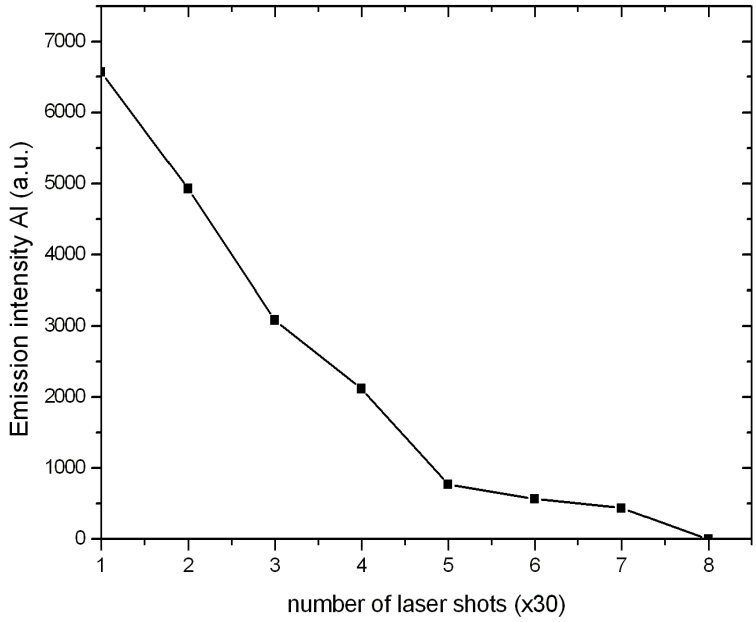

Fig 5.29.: Al composition profile obtained by LIBS

Furthermore, the other trace elements revealed are tin, for lotus flower shaped necklace, and gold for fibula from Torre di Satriano.

To conclude, these jewels are probably linked to different productive processes or different productive areas because the compositional analysis confirm the use of different sources for raw materials, suggesting a different provenance for these objects. In particular the fibula from Tower of Satriano site contains gold only as trace element whereas in the other three objects gold is present in a higher percentage.

In the following table are summarized the data obtained (Table 5.7.).

	Major element	Minor elements	Trace elements
Necklace REP. 211227	Ag	Cu, Au	Ca, Al
Fibula REP. 213149	Ag	Cu, Au	Ca, Al
Necklace REP. 205496	Ag	Cu, Au	Ca, Al
Fibula REP. 409925	Ag	Cu	Au, Sn, Ca, Al

Table 5.7. compositional analysis of silver findings analyzed by LIBS

5.6. References

[1] L. C. Giannossa, S. Loperfido, M. Caggese, G. E. De Benedetto, R. Laviano, L. Sabbatini, and A. Mangone, "A systematic characterization of fibulae from Italy: from chemical composition to microstructure and corrosion processes," *New J. Chem.*, vol. 37, p. 1238, 2013.

[2] A. Arafat, M. Na'es, V. Kantarelou, N. Haddad, A. Giakoumaki, V. Argyropoulos, D. Anglos, and A. G. Karydas, "Combined in situ micro-XRF, LIBS and SEM-EDS analysis of base metal and corrosion products for Islamic copper alloyed artefacts from Umm Qais museum, Jordan," *J. Cult. Herit.*, vol. 14, pp. 261–269, 2013.

[3] A. Nevin, G. Spoto, and D. Anglos, "Laser spectroscopies for elemental and molecular analysis in art and archaeology," *Appl. Phys. A Mater. Sci. Process.*, vol. 106, pp. 339–361, 2012.

[4] M. Corsi, G. Cristoforetti, M. Giuffrida, M. Hidalgo, S. Legnaioli, L. Masotti, V. Palleschi, A. Salvetti, E. Tognoni, C. Vallebona, and A. Zanini, "Archaeometric analysis of ancient copper artefacts by laser-induced breakdown spectroscopy technique," *Microchim. Acta*, vol. 152, pp. 105–111, 2005.

[5] V. Spizzichino and R. Fantoni, "Laser Induced Breakdown Spectroscopy in archeometry: A review of its application and future perspectives," *Spectrochim. Acta - Part B At. Spectrosc.*, vol. 99, pp. 201–209, 2014.

[6] K. Melessanaki, M. Mateo, S. C. Ferrence, P. P. Betancourt, and D. Anglos, "The application of LIBS for the analysis of archaeological ceramic and metal artifacts," *Appl. Surf. Sci.*, vol. 197–198, pp. 156–163, 2002.

[7] M. Kuzuya, M. Murakami, and N. Maruyama, "Quantitative analysis of ceramics by laser-induced breakdown spectroscopy," vol. 58, pp. 957–965, 2003.

[8] A. J. López, G. Nicolás, M. P. Mateo, A. Ramil, V. Piñón, and A. Yáñez, "LIPS and linear correlation analysis applied to the classification of Roman pottery Terra Sigillata," *Appl. Phys. A Mater. Sci. Process.*, vol. 83, pp. 695–698, 2006.

[9] A. Khedr and M. A. Harith, "In-depth micro-spectrochemical analysis of archaeological Egyptian pottery shards," *Appl. Phys. A Mater. Sci. Process.*, vol. 113, pp. 835–842, 2013.

[10] A. K. Jahromi, "Highly-sensitive stoichiometric analysis of YAG ceramics using laser-

induced breakdown spectroscopy (LIBS)," 2014.

[11] S. Guirado, F. J. Fortes, and J. J. Laserna, "Elemental analysis of materials in an underwater archeological shipwreck using a novel remote laser-induced breakdown spectroscopy system," *Talanta*, vol. 137, pp. 182–188, 2015.

[12] A. J. López, G. Nicolás, M. P. Mateo, V. Piñón, M. J. Tobar, and A. Ramil, "Compositional analysis of Hispanic Terra Sigillata by laser-induced breakdown spectroscopy," *Spectrochim. Acta - Part B At. Spectrosc.*, vol. 60, no. 7–8, pp. 1149–1154, 2005.

[13] V. Lazic, F. Colao, R. Fantoni, A. Palucci, V. Spizzichino, I. Borgia, B. G. Brunetti, and A. Sgamellotti, "Characterisation of lustre and pigment composition in ancient pottery by laser induced fluorescence and breakdown spectroscopy," *J. Cult. Herit.*, vol. 4, pp. 303–308, 2003.

[14] J. Anzano, S. Sangüesa, J. Casas-González, M. Á. Magallón, M. Escudero, J. Anwar, and U. Shafique, "Analysis of Roman-Hispanic Archaeological Ceramics using Laser-Induced Breakdown Spectroscopy," *Anal. Lett.*, vol. 48, no. 10, pp. 1638–1643, 2015.

[15] L. E. García-Ayuso, J. Amador-Hernández, J. M. Fernández-Romero, and M. D. Luque De Castro, "Characterization of jewellery products by laser-induced breakdown spectroscopy," *Anal. Chim. Acta*, vol. 457, pp. 247–256, 2002.

[16] K. K. Herrera, E. Tognoni, N. Omenetto, B. W. Smith, and J. D. Winefordner, "Semi-quantitative analysis of metal alloys, brass and soil samples by calibration-free laser-induced breakdown spectroscopy: recent results and considerations," *J. Anal. At. Spectrom.*, vol. 24, p. 413, 2009.

[17] F. Colao, L. Caneve, R. Fantoni, A. Giardini, V. Lazic, and V. Spizzichino, "LIBS as a diagnostic tool during the laser cleaning of copper based alloys: experimental results," *J. Anal. At. Spectrom.*, vol. 19, no. 4, p. 502, 2004.

[18] F. Colao, R. Fantoni, V. Lazic, and V. Spizzichino, "Laser-induced breakdown spectroscopy for semi-quantitative and quantitative analyses of artworks—application on multi-layered ceramics and copper based alloys," *Spectrochim. Acta Part B At. Spectrosc.*, vol. 57, pp. 1219–1234, 2002.

[19] M. Ferretti, C. Polese, and C. Roldán García, "X-ray fluorescence investigation of gilded and enamelled silver: The case study of four medieval processional crosses from central Italy," *Spectrochim. Acta - Part B At. Spectrosc.*, vol. 83–84, pp. 21–27, 2013.

[20] B. Constantinescu, R. Bugoi, E. Oberländer-Târnoveanu, and K. Pârvan, "Medieval silver coins analyses by pixe and ED-XRF techniques," *Rom. Reports Phys.*, vol. 54, pp. 481–

490, 2009.

[21] L. Pardini, A. El Hassan, M. Ferretti, A. Foresta, S. Legnaioli, G. Lorenzetti, E. Nebbia, F. Catalli, M. A. Harith, D. Diaz Pace, F. Anabitarte Garcia, M. Scuotto, and V. Palleschi, "X-ray fluorescence and laser-induced breakdown spectroscopy analysis of Roman silver denarii," *Spectrochim. Acta - Part B At. Spectrosc.*, vol. 74–75, pp. 156–161, 2012.

[22] A. G. Karydas, D. Kotzamani, R. Bernard, J. N. Barrandon, and C. Zarkadas, "A compositional study of a museum jewellery collection (7th-1st BC) by means of a portable XRF spectrometer," *Nucl. Instruments Methods Phys. Res. Sect. B Beam Interact. with Mater. Atoms*, vol. 226, pp. 15–28, 2004.

[23] M. Ferretti, L. Miazzo, and P. Moioli, "The application of a non-destructive XRF method to identify different alloys in the bronze statue of the Capitoline horse," *Stud. Conserv.*, vol. 42, pp. 241–246, 1997.

[24] A. Vasilescu, B. Constantinescu, D. Stan, M. Radtke, U. Reinholz, G. Buzanich, and D. Ceccato, "Studies on ancient silver metallurgy using SR XRF and micro-PIXE," *Radiat. Phys. Chem.*, vol. 117, pp. 26–34, 2015.

[25] C. F. L.Robbiola, J.M.Blengino, "Morphology and mechanisms of formation of natural patinas on archaeological Cu-Sn alloys," *Corros. Sci.*, vol. 40, pp. 2080–2111, 1998.

[26] V. A. Solé, E. Papillon, M. Cotte, P. Walter, and J. Susini, "A multiplatform code for the analysis of energy-dispersive X-ray fluorescence spectra," *Spectrochim. Acta - Part B At. Spectrosc.*, vol. 62, pp. 63–68, 2007.

[27] A. F. B. Baglivo, A. Bottini, A. De Siena, G. Ferreri, A. M. M. G. Greco, P.G. Guzzo, F. Lembo, F.P.R. Marino, and M. V. M. Osanna, *Segni del potere - Oggetti di lusso dal Mediterraneo nell'Appennino lucano di età arcaica*, Osanna Edi. 2013.

[28] B. Torre, M. Osanna, M. Fabbri, F. Sogliani, D. Mallardi, and G. Loiudice, "Basilicata. Torre di Satriano (PZ).," pp. 1–42, 2012.

[29] "NIST Database, National Institute Of Standard and Tecnology, Gaithersburg Md, USA, 2003, http://www.nist.gov," *NIST Database, National Institute Of Standard and Tecnology, Gaithersburg Md, USA, 2003, http://www.nist.gov*. .

[30] http: // www. cfa. harvard. edu/amp/ampdata. kurucz23/sekur. htm. Kurucz Atomic Spectral Lines Database.

[31] P. T. Craddock, "Metallography and microstructure of ancient and historic metals," *Endeavour*, vol. 16, p. 152, 1992.

[32] A. De Bonis, B. De Filippo, A. Galasso, A. Santagata, A. Smaldone, and R. Teghil,

"Comparison of the performances of nanosecond and femtosecond Laser Induced Breakdown Spectroscopy for depth profiling of an artificially corroded bronze," *Appl. Surf. Sci.*, vol. 302, pp. 275–279, 2014.

[33] Skira, *Tesori dell'Italia del Sud catalogo della Mostra Greci e Indigeni in Basilicata 25 giugno - 24 agosto 1999*. 1999.

[34] S. Pandhija and A. K. Rai, "Laser-induced breakdown spectroscopy : A versatile tool for monitoring traces in materials," vol. 70, pp. 553–563, 2008.

[35] P. M. Dattola, Luigi, Trocino A, "Primi dati sulle miniere nel territorio di Longobucco e considerazioni di salvaguardia ambientale," 2008, 2015.

Chapter 6

Plasma features and application to material science

6.1. Introduction

LIP and laser ablation have found applications in several fields such as analytical spectroscopy and pulsed laser deposition of thin film.

As analytical technique, LIBS has demonstrated great versatility and adaptability to different practical problems.

Furthermore, the optical emission spectroscopy (OES) of LIP has become a powerful tool for the fundamental studies of the interaction between laser beam and material [1].

The study of LIP properties from emission spectra, such as expansion rate of species, temperature and number density, is useful for a detailed knowledge of LIP since it depends strongly on the experimental conditions in which the ablation is carried out, for example of state of aggregation of target and background environment pressure (atmospheric, reduced or high pressure) [2].

The physical chemical study of the ablated material allows to monitor the ablation process and improves the knowledge of dynamic of plasma formation [3]–[10].

As previously said, the laser ablation can be performed on any type of material, so, in this work, the ablation mechanism of a new complex material is investigated.

The analysis are carried out on an active material for Lithium Ion Batteries (LIBs), i.e. lithium cobalt-phosphate doped to 10% iron, $LiCo_{0.9}Fe_{0.1}PO_4$ (FeLCP).

This chapter is divided into two parts, at first, the characteristics of FeLCP plasma are studied by optical emission spectroscopy and ICCD fast imaging in order to obtain information about its temporal and spatial evolution.

A nanosecond laser Nd: YAG is used for ablation and the effect of different gaseous environment (vacuum, oxygen and argon) on plasma produced are evaluated.

In the second part, utilizing the Pulsed Laser Deposition (PLD) technique, a set of FeLCP thin films are fabricated in order to clarify the correlation between different pressures conditions and the structures deposited.

In addition to different gas pressures, the influence of another deposition parameters, e.g., substrate types (stainless steel and silicon) and post-annealing treatment on the crystallinity and morphology of thin films has been investigated.

The crystallinity and morphology of these thin films have been analyzed by X-Ray Diffraction and Scanning Electron Microscopy, while the first steps of the films growth have been characterized by Transmission Electron Microscopy.

As a final point, the activity of thin films of FeLCP grown on S316 steel foils have been tested as positive electrode materials in lithium cells to demonstrate their reversible electrochemical activity.

6.2. Lithium Ion Batteries and $LiCo_{0.9}Fe_{0.1}PO_4$ (FeLCP)

The material studied in this work is lithium cobalt-phosphate doped to 10% iron, that is a promising cathode material for LIBs because of its high theoretical capacity [11]. Thanks to characteristics of high – energy and high power density, the Lithium Ion Batteries have become very important, especially in the field of portable electronics, power devices and electric vehicles [1] [12].

The recent developments of these technological devices, consequently, led to research of new materials with better electrochemical features [13]

In the most typical formulation both positive and negative electrode materials are intercalation compounds which allow the reversible insertion of Li^+ guest ions (Fig. 6.1.).

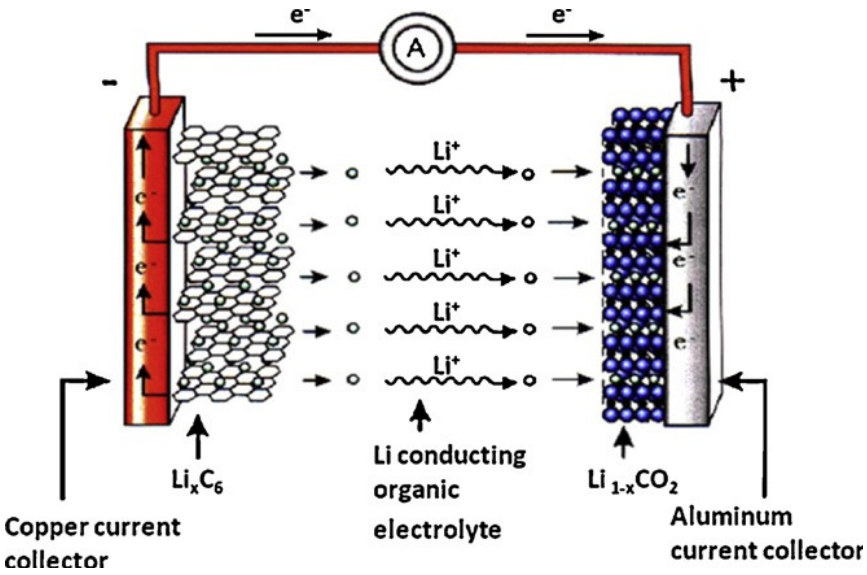

Fig. 6.1.: Scheme of a common lithium ion battery [1].

Several materials can be used as cathodes in Li-ion batteries, including transition metal oxides ($LiMO_2$ with M = Co, Ni, Mn) or polyanion compounds ($(XO_4)^{3-}$ with X = S, P, Si, As, Mo, W).

The $LiMPO_4$ (M = Fe, Co, Mn) olivine – type transition metal orthophosphate are particularly attractive for the use as cathode materials (Fig. 6.2.).

The most used material is Lithium Iron Phosphate LFP, that is characterized of high thermal stability and low costs, and has been widely studied and its characteristics have been largely optimized [14].

Recently, the isostructural $LiCoPO_4$ (LCP) olivine lithium seems to be a good candidate, due to his high working potential and promising theoretical capacity, though costs are higher than the previous one .

On the other hand, disadvantages of this material are small Li – ion mobility in the lattice, a quite low capacity, rapidly decreasing in case of structure deterioration, and poor electronic conductivity.

Experimentally, it has been found that, doping $LiCoPO_4$ with other transition metals, in particular with iron, the capacity fading decreases, the electronic and ionic conductivity increase and, consequently, galvanostatic cycling performances improve[15]–[17].

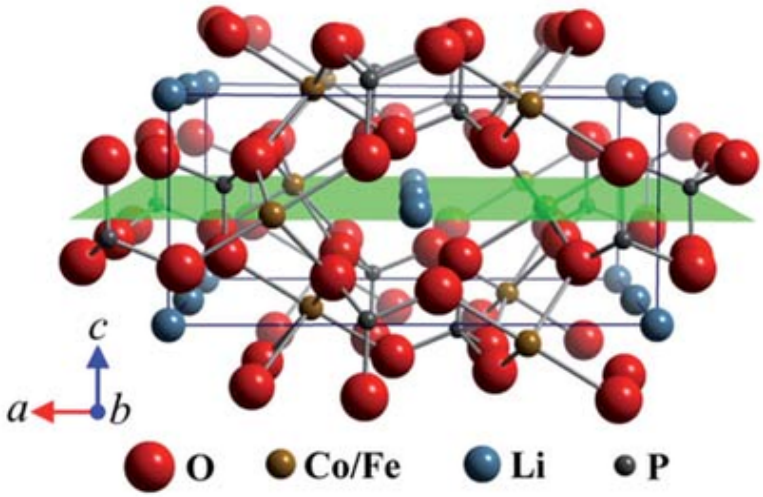

Fig. 6.2.: Olivine Structure of lithium cobalt phosphate doped with iron [17]

$$CoPO_4 + 0.7\ Li^+ + 0.7\ e^- \leftrightarrow Li_{0.7}CoPO_4 \quad \text{(step 1)}$$

$$Li_{0.7}CoPO_4 + 0.3\ Li^+ + 0.3\ e^- \leftrightarrow LiCoPO_4 \quad \text{(step 2)}$$

In the first step, the 70% of cobalt ions are reduced from Co^{+3} to Co^{+2} and the 70% of Li^+ ions insert in olivine lattice, leading to the $Li_{0.7}CoPO_4$ phase formation.

in the second step the remaining 30% Co^{3+} reduce to Co^{2+}, the remaining 30% of Li^+ ions insert in olivine lattice, forming the $LiCoPO_4$ phase.

These two consecutive biphasic processes are visible as two plateau in galvanostatic cycles [15], [18].

Another important factor for that has been increase the attention on Lithium Ion Batteries is the possible applicability in micro batteries, in which cathode and anode materials are inserted in the form of thin films with thickness < 10 μm [19], [20].

The rise of use of miniaturized devices has significantly increased the production of micro-scale power sources, that can be useful in a variety of fields, such as medical devices, smart cards or micro-sensor systems.

6.2.1 FeLCP synthesis

FeLCP is synthesized by a solvothermal route, where two water solutions are prepared.
First, a solution containing lithium hydroxide monohydrate ($LiOH \cdot H_2O$) LiOH into 5 ml H_2O is added, under vigorous stirring, to ethylene glycol (EG – 20 ml).
After complete dissolution, another water solution (5 ml), containing LiH_2PO_4, $CoSO_4 \cdot 7H_2O$ and $FeSO_4 \cdot 7H_2O$, is added drop to drop to the previous solution (EG:H_2O v/v ratio 2:1, final volume 30 ml).
The obtained purple suspension is sealed into a Teflon-lined stainless steel autoclave and heated in oven at 220 °C for 20 h. The product is filtered, washed with H_2O/ethanol and dried in oven [21]. Finally, it is annealed at 400°C for 2 h under air flow.

6.3. Pulsed Laser Deposition of thin film

Thin films of different materials suitable for application in Li-ion cells as high potential cathodes have been successfully deposited using different deposition methods [22].
Laser based techniques are certainly suited to fabricate and optimize these electrochemical energy storage components for micropower systems.
Among these techniques, Pulse Laser Deposition (PLD) is useful for the deposition of thin films of materials with a complex stoichiometry [13], [23].
Regarding the cathode materials deposition, PLD has been used for thin film deposition of $LiCoO_2$ [16], [23], [24], $LiMn_2O_4$ [25]–[31] and $LiFePO_4$ [27], [32]–[39] and also for other more complex materials including $LiNi_{0.5}Mn_{0.5}O_2$ [40], $LiNi_{0.8}Co_{0.2}O_2$ [41], $LiCo_{1-x}Al_xO_2$ [42], $TiNb_2O_7$ [43], $Li_{1.2}Mn_{0.54}Ni_{0.13}Co_{0.13}O_2$ [44] and Li_4SiO_4-Li_3PO_4 [11], depositing with laser of different wavelengths and in different environmental conditions.
A PLD experiment is surprisingly simple (Fig. 6.3.) but the physical processes, from the initial light absorption by a target to the film deposition, are very complex.
A target in a vacuum chamber is irradiated by a laser with nanosecond pulses such that the material is removed from the target.

This ablation of material, during high intensity laser irradiation, leads to the formation of a plasma which expands in a flow perpendicular to the surface and is collected on a suitable substrate, placed in an appropriate distance from the target.

Using a large number of pulses, the material accumulates and a film grows on the substrate, with thickness in the range between nanometers and micrometers.

An important feature of PLD is that the stoichiometry of the target can be often retained in the deposited films. This is due to strong interaction of the target surface with the laser irradiation.

If the laser fluence is low, the laser pulse simply heats the target and evaporates the target species. In this case, the evaporative flux from a multicomponent target can be determined by the vapor pressures of its constituents.

As the laser fluence is increased, the ablation threshold is reached where the absorbed laser energy is higher than that needed for evaporation. In this case, the flux of vaporized species is not dependent on the vapor pressures of the constituent cations. This non-equilibrium process leads to the congruent evaporation of the target. This stoichiometric transfer between target and substrate is difficult to achieve with other physical vapor deposition techniques.

In PLD, different experimental parameters can be chosen for each deposition, such as substrate temperature, gas pressure, type of substrate, but, if this possibility offers a high flexibility, it can also be difficult to identify the best conditions for the production of a specific type of film.

In addition to the possibility to obtain films of correct stoichiometry, the PLD method has other advantages.

First of all, the initial laser – target interaction is completely decoupled from environmental conditions such as type and pressure of background gas or type and temperature of substrate [45]. Moreover, choosing the deposition time and the laser fluence, PLD technique allows to control the number of particles arriving at the substrate, obtaining a layer by layer growth of thin film.

6.4. FeLCP laser ablation and thin film deposition

The aim of this work is to describe the characterization of FeLCP plasma by spectroscopy study in order to evaluate the physical chemical parameters in different surrounding atmospheres.

For studying the effect of gas on plasma evolution, the experiments are performed at a range of pressures from vacuum (10^{-4} Pa) to a pressure of 100 Pa in both inert Argon gas and reactive Oxygen atmosphere.

Moreover, because no papers reporting data about the characteristics of thin film of FeLCP are present in literature, the second part of this work is focused on their production in order to fabricate micro lithium ion batteries.

6.4.1. PLD experimental set up

The FeLCP target is prepared by cold pressing of its powder into a pellet.

The films are deposited at room temperature, varying the gas pressure ($1.5 \cdot 10^{-4}$ Pa, 100 Pa Argon and 100 Pa O_2) and the type of substrate (Si (100) and S316 steel).

The distance between the target and the substrate is kept at 1 cm and the laser beam is incident at an angle of 45° on the target surface.

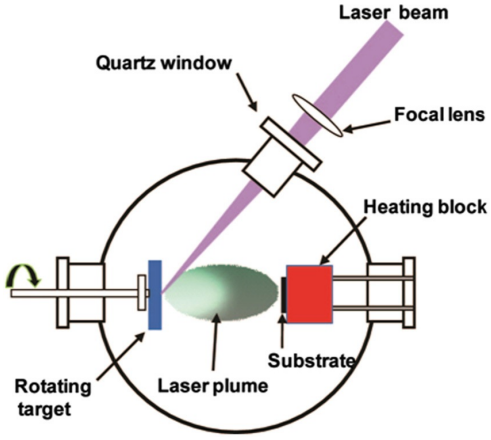

Fig. 6.3.: Schematic illustration of the pulsed laser deposition (PLD) setup

In the next sections, the set-up components are described in details.

6.4.1.1. ns Nd:YAG Laser

The ablation source used for PLD experiments is a Quanta System Q-switched Nd:YAG laser (Fig.6.4.), that is the most common solid state laser source.

The active medium is constituted by a neodymium-doped yttrium aluminium garnet crystal ($Nd:Y_3Al_5O_{12}$) that is optically pumped using flash lamps.

The Q-switching mode is used to obtain high energy short (ns) pulses, through modulation of intra-cavity losses.

Control of the cavity losses is obtained with active Q-switching method, that requires the use of a modulating device which is triggered by an external source (outside the cavity).

The output radiation has typical pulse widths in the range 6 – 15 ns and a fundamental wavelength at 1064 nm, which is converted onto in 532 in the same way of other laser system.

The Nd:YAG lasers are commercially available with a relatively high output pulse energies (from mJ to J), broad repetition operation rate (1 – 50 Hz) and in abroad range of sizes allowing both robust laboratory and portable LIBS systems.

In this work, all PLD experiments are performed with a frequency doubled of 532 nm, a pulse duration of 10 ns and a repetition rate of 10 Hz. The laser fluence is kept at 10 Jcm^{-2} and the deposition time is 2 hours.

Fig. 6.4.: Quanta System Q-switched Nd:YAG laser

6.4.1.2. Ablation chamber

For deposition of thin films in vacuum condition, a stainless steel vacuum chamber (Fig. 6.5.) is used, that is equipped with several input windows, each with different uses: two of these are used for the entry of the laser beam (at 45° and 90° with respect of target), one for connection with the pumping system, two for the positioning of the target and the substrate, one for the measuring of vacuum, one for a gas inlet, and one for the in situ analysis of the luminescence emitted by the plume.

The pumping system is formed by a scroll-pump, which forms a pre-vacuum (10^{-1} Pa), and a turbomolecular pump, for obtaining the working pressure of the order of 10^{-4} Pa.

The pre-vacuum pressure is monitored by a thermal conductivity vacuum gauge (Pirani) whereas for high-vacuum pressure is used a cold cathode ionization vacuum gauge (Penning) is used.

The target is mounted on a rotating holder, that is connected to a synchronous motor.

Indeed, if the laser beam hits always the same area, deep craters on the surface target can be formed.

In this way, the plasma could be remain confined into the crater and would not be free to expand, changing the plasma characteristics.

The continuous rotation is needed to minimizes the formation of craters and, also to prevent excessive damage of the target. The chamber is also equipped with a heatable substrate support, that allows to obtain deposition at high temperatures.

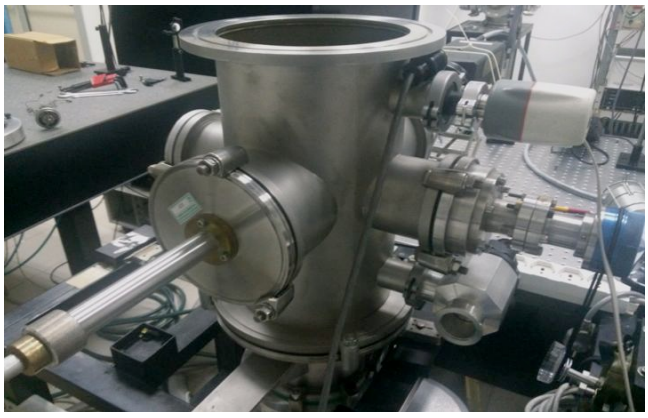

Fig. 6.5.: Stainless steel chamber ablation

6.5. FeLCP plasma analysis

The gaseous phase obtained by ablating the cathode material $LiFeCoPO_4$ target has been characterized at different experimental conditions, by optical emission spectroscopy.

As said in section 6.2., FeLCP is a promising candidate for the production of Lithium Ion Batteries so it is important to understand the plasma plume formation and expansion process.

In order to perform this evaluation, the space and time resolved emission spectra have been acquired by the employment of an optical multichannel analyzed (OMA).

In this way the plasma plume species distribution and their physical proprieties can be assessed.

Moreover other information about the plasma flow dynamics can be achieved by Intensified Charge Coupled Devise (ICCD) fast imaging (Fig. 6.6.).

In the next sections the details of experimental apparatus are described.

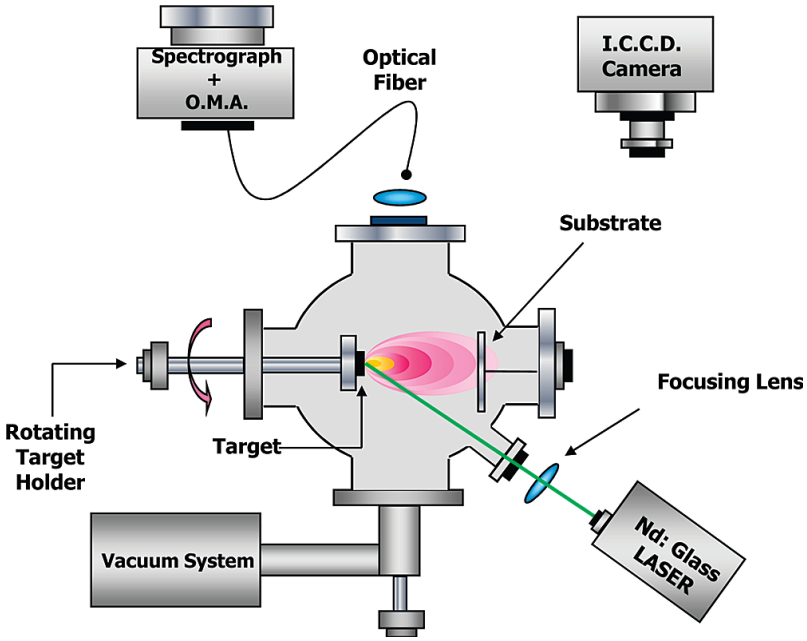

Fig. 6.6.: Scheme of experimental set up

6.5.1. Optical Multichannel Analyzed (OMA) and ICCD fast imaging

The spectroscopy system OMA is the same employed for LIBS analysis, already described in paragraph 4.2.5.

In this case, the luminescence emitted by the plume both in low and high pressure conditions is focalized on an optical fibre through a couple of quartz biconvex lenses with focal length of 7.5 cm.

This optical fibre is made of a bundle of 19 fused silica fibers with a diameter of 0.6 mm that is linked to the spectrograph (ARC 500i).

In order to increase the signal to noise ratio, it is possible acquired a spectrum obtained with multiple laser pulses.

Also, the space-resolved emission spectra can be acquired at different distances from the target by varying the position of the optical fibre using a micrometric translation stage.

The technique of fast photography by Intensified Charge Coupled Device detector is used to obtain information about dynamic and expanding plasma.

The ICCD devise (the same used for OMA experiments) is connected to a 105/35 mm quartz Nikkor photographic lens, which has quartz lenses and observable area of 7 cm^2.

The luminescence emitted by the plasma is observed at 90° with respect of the target for acquiring gated lateral view images of the overall plasma emission (200-800 nm) induced by a single laser pulse.

The image acquisition can be obtained by only one laser pulse but, in order to increase the signal to noise ratio, it is useful to integrate on a great number of acquisitions.

The spatial resolution achieved by this system is 25 μm and the resolving power of is 5 ns.

The images are processed with a software that gives a plasma represented by a series of contour lines which correspond to different emission intensities.

The acquisitions are performed by accumulating up to 5 shots, thereby avoiding previously irradiated surfaces.

Both ICCD fast imaging and time-resolved spectra have been accomplished by delaying the data acquisition of the plasma emission with respect to the laser pulse.

6.5.2. FeLCP plasma composition

The optical emission spectra are detected both in vacuum and in presence of surrounding gases (100 Pa Ar and 100 Pa O_2).

The grating employed is 1200 grooves/mm thus the spectral width obtained is of about 20 nm.

The gate system used has a time resolution of 10 ns and each acquisition is integrated on 30 laser shots in order to increase the signal to noise ratio.

From analytical point of view, all spectra obtained show the presence of the same components: neutral lithium, iron and cobalt (Li I, Fe I, Co I) and singly ionized phosphorus P II.

The two main spectral regions are in the range from 600 to 619 nm for neutral lithium (Li I) signal and from 333 to 354 nm for neutral iron and cobalt (Fe I and Co I) signals.

By delaying the data acquisition of the plasma emission in the range of 10-350 ns with respect to the laser pulse, the time resolved spectra (also known as kinetic series) are obtained.

The acquisition is performed by accumulating 20 laser shots, moving continuously the target. An example of kinetic series is reported in Fig.6.7. that shows the temporal evolution of spectral lines measured at pressure of 10^{-4} Pa on the Co I and Fe I region:

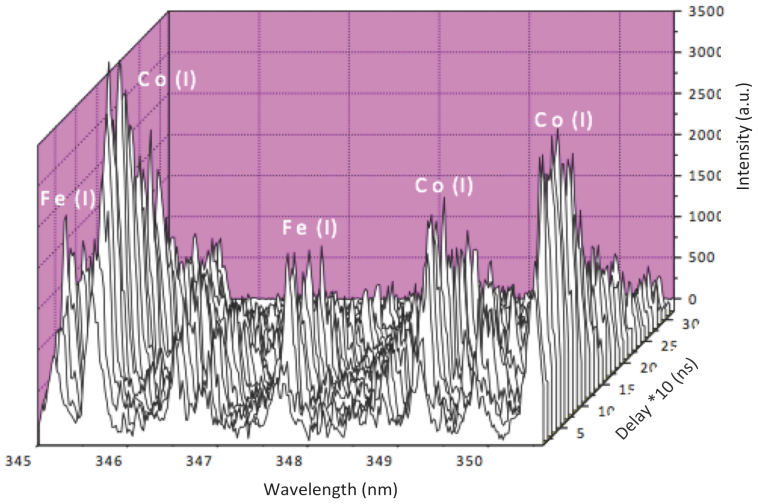

Fig. 6.7.: Temporal evolution of Co I and Fe I emission lines at 10^{-4} Pa pressure

From the spectra acquired at various delay time, appears that the intensity of the species present in plasma overcome the continuum emission soon after the laser shot and, after, the line emissions evolve regularly in time by increasing during the first 100 ns and subsequently decreasing.

On the other hand, for ion P(II) specie, the kinetic series has not been detected due to the weak intensity of the signal.

6.5.3. Temperature and electron density measurement

The OES data can be also used for evaluating plasma parameters such as excitation temperature and electron density.

The plasma temperature (T_e) is determined using Boltzmann plot method (section 2.8.1.), assuming that the local thermodynamic equilibrium (LTE) condition is fulfilled.

Different spectral series, obtained by a fixed detection gate of 10 ns, and starting at a delay of 30 ns, are accomplished.

For drawing Boltzmann plot, a set of transitions lines of neutral cobalt Co I is considered.

The spectroscopic data of these emission lines are taken from the NIST and the Kurucz database [46] [47] and are listed in the following table (Table 6.1.):

λ (nm)	**A (s^{-1})**	**E_2 (cm^{-1})**	**g_u**
339.53	$2.87 \cdot 10^7$	34133.6	8
340.91	$4.22 \cdot 10^7$	33466.8	8
341.26	$1.19 \cdot 10^7$	29294.5	8
341.70	$3.22 \cdot 10^7$	33946.0	6
345.35	$1.12 \cdot 10^8$	32430.6	12
348.94	$1.29 \cdot 10^8$	36092.4	6

Table 6.1.: Spectroscopic constant of the electronic transition employed

The LTE condition seems to be satisfied by the good linearity of all Boltzmann plots obtained in the temporal delay used (30-250 ns).

Two Boltzmann plots obtained in different pressure condition at the same delay time of 150 ns are shown as example in Fig.6.8.

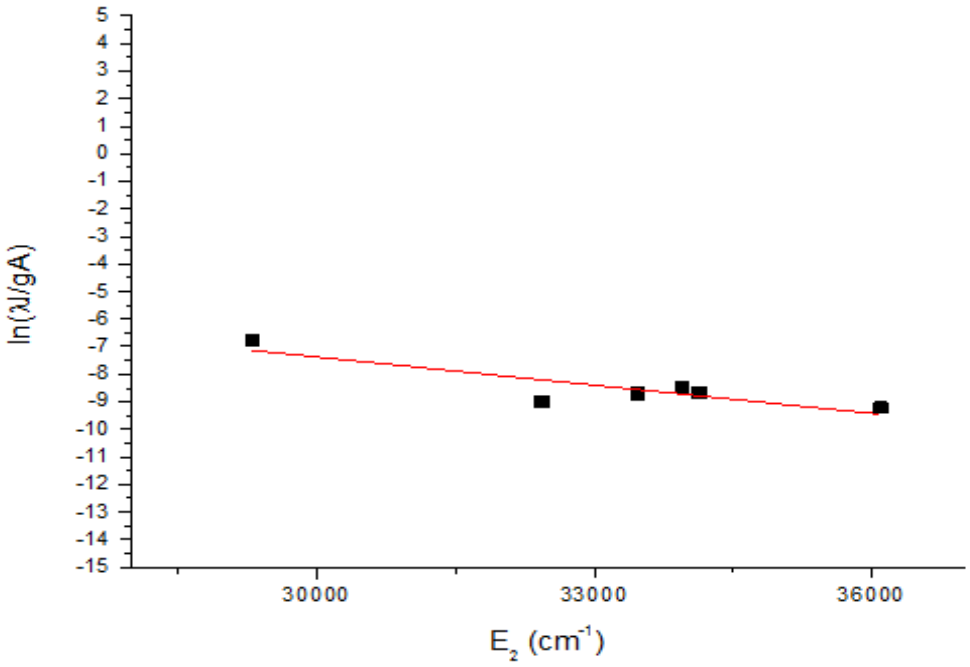

(a)

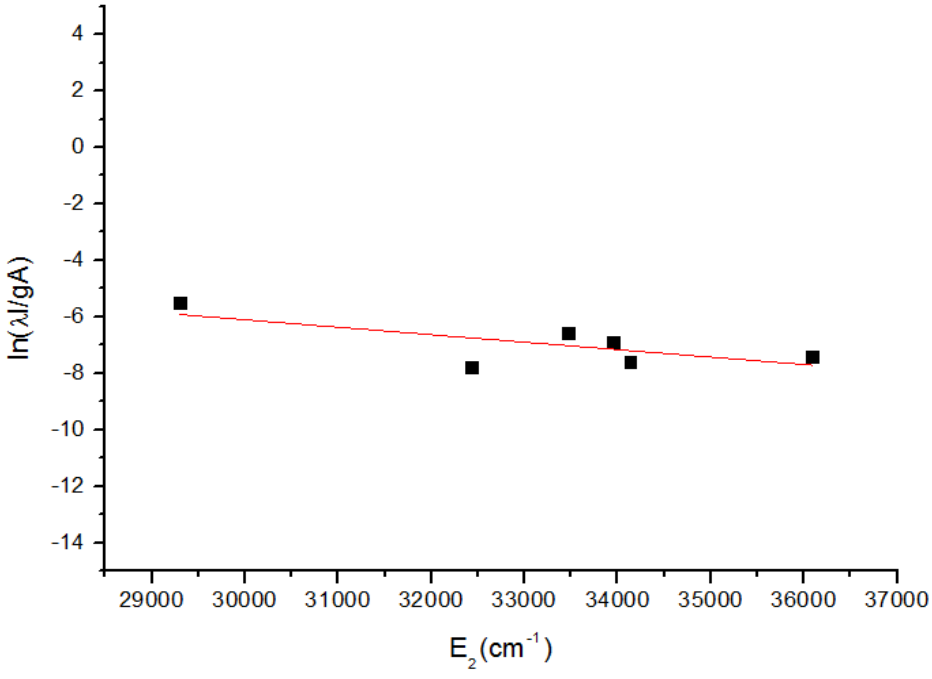

(b)

Fig. 6.8.: Co Boltzmann plots obtained at delay time of 150 ns (a) at pressure of 100 Pa O_2 and (b) in vacuum condition

The Fig. 6.9. reports the temporal evolution of the excitation temperature in vacuum condition and at Argon pressure of 10^2 Pa.

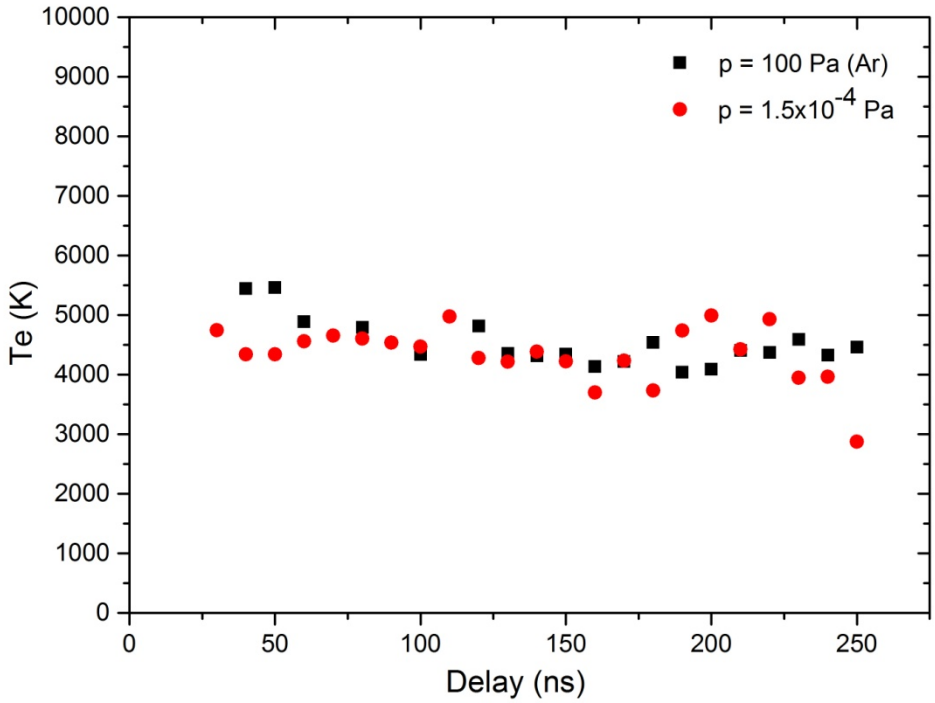

Fig. 6.9.: Temporal evolution of the electron temperature of the FeLCP plasma plume expanding in vacuum condition e in presence of gas buffer

It is evident that T_e does not change significantly with the environment pressure and also remains almost constant with the delay time increase.

The data obtained in oxygen atmosphere show the same trend and values.

Furthermore, the temporal electron densities behaviours induced by different gas condition can be evaluated from the same OES data.

Also in this case, the spectral series are recorded with fixed gate time of 10 ns and starting at delay time of 30 ns (range 30 – 270 ns).

The Full Width at Half Maximum (FWHM) Stark broadening of the neutral Li I line centred at 610.40 nm is used, according to the equation 2.10 and fitting experimental curves with symmetrical Voigt profiles.

The temporal evolution of the electron density both for vacuum condition and pressure of 100 Pa of Argon and Oxygen is shown in Fig. 6.10.

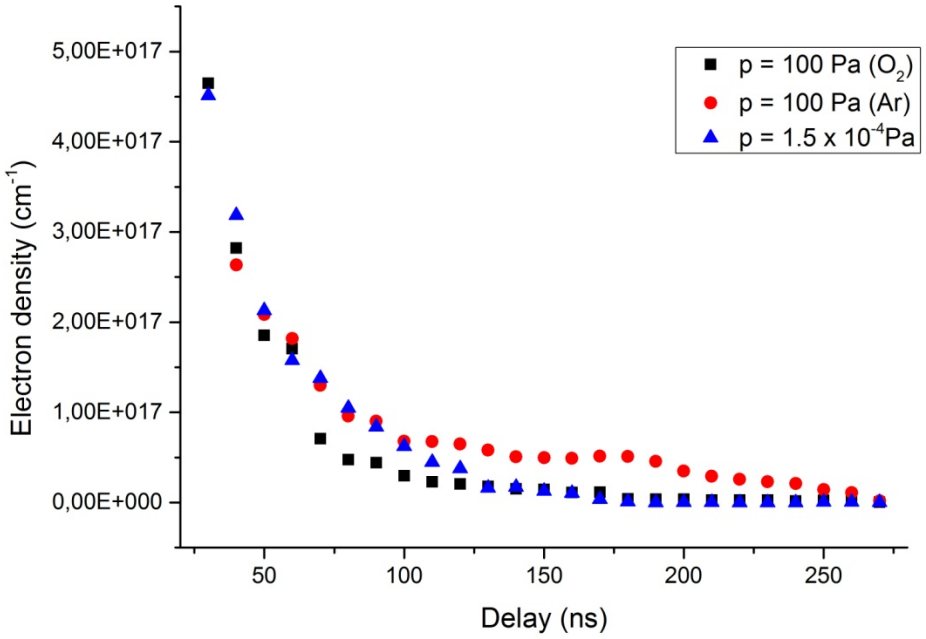

Fig. 6.10.: Temporal evolution of the electron density of the FeLCP plasma plume expanding in vacuum condition e in presence of gas buffer (O_2 and Ar)

Also in this case no remarkable differences have been detected with different pressure conditions and the data obtained in oxygen atmosphere show the same trend and values. In vacuum condition the electron density changes from $4.5 \cdot 10^{17}$ cm^{-3} to $2.6 \cdot 10^{14}$ cm^{-3}, at 100 Pa of buffer gas Argon it change $2.6 \cdot 10^{17}$ cm^{-3} to $1.7 \cdot 10^{15}$ cm^{-3} and at 100 Pa of Oxygen it change $4.6 \cdot 10^{17}$ cm^{-3} to $2.7 \cdot 10^{14}$ cm^{-3}.

Anyway, taking into account the calculated n_e values and the McWhirter criterion, the LTE assumption can be strengthened for any delay time examined because it should be fulfilled for n_e values greater than 10^{16} cm^{-3}.

6.5.4. Angular distributions and front velocities

The vacuum and the pressure regime give origin to plasma plumes different in shape and velocity.

The ICCD fast imaging is utilized to determine plasma front velocity and angular distributions and the data from ablation in vacuum are compared with those obtained at

100 Pa Ar. From the intensity contour patterns, it evident the main difference in plasma shapes (Fig. 6.11.).

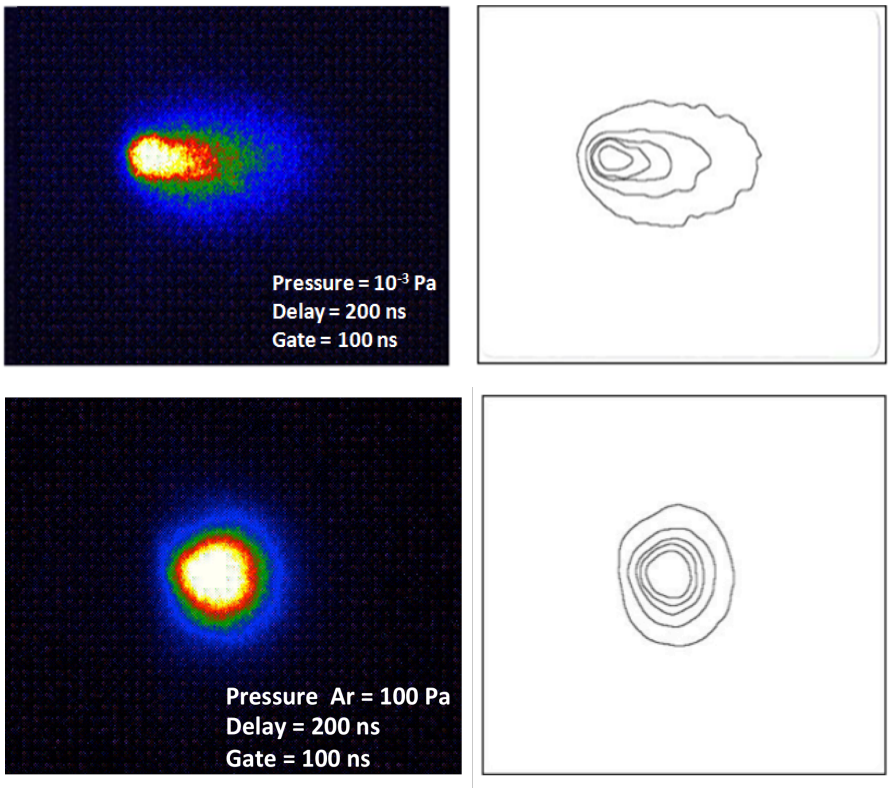

Fig. 6.11.: Plasma plume fast imagining induced in different pressure conditions, associated with the intensity contour patters

The images are measured through a software which allows to have contours depending on the intensity with an interval of 20%.

From these images it is possible to obtain a parameter n, which represents the anisotropy of the angular distribution. Indeed, the angular distribution of the plume can be described by the following expression:

$$I(\theta) = I_0 \cos^n(\theta) \qquad \text{(eq. 6.1.)}$$

where I(θ) is the flux intensity along a direction forming an angle θ with the perpendicular to the target surface and I_0 is the intensity corresponding to θ = 0.

The parameter n is obtained using the following equation:

$$n = \frac{2\ln 2}{\ln(1 + x^2)} - 1$$

(eq. 6.2.)

where x = b/a is the ratio between the minor axis “b” and the major axis “a” of the plume, considered elliptical (Fig. 6.12.).

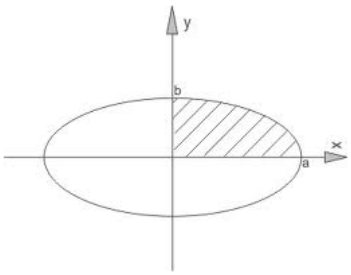

Fig. 6.12.: Schematic shape of an elliptical plume

In vacuum condition, the plasma form is elliptical and the value of n is equal to 3.8.

With values greater than 1, the plume is elongated in perpendicular direction respect to the target, as is confirmed by ICCD image.

For pressure of 100 Pa Argon, the value obtained is 0.9, indeed, values close to 1 indicate spherical angular distribution, as shown in the previous image.

Furthermore, from ICCD images, recorded at different time delays from the laser shot, it is possible to calculate the velocity of the different plumes.

The velocity changes depending on the pressure conditions, decreasing of one order of magnitude from the $6.7 \cdot 10^6$ cm s^{-1} in vacuum condition to $5.0 \cdot 10^5$ cm s^{-1} at 100 Pa of Argon (Table 6.2.).

This difference is related to plasma confinement accomplished by the gas molecules.

Pressure (Pa)	Velocity (cm s^{-1})	n
10^{-4}	$6.7 \cdot 10^6$	3.8
10^2	$5.0 \cdot 10^5$	0.9

Table 6.2.: Velocity of FeLCP plumes and parameters n obtained at different pressure conditions

6.5.5. Space and time plasma evolution

Comparing the images acquired at different delay times and gate time of 100 ns (Fig.6.13.), it is possible to note that in vacuum condition the plasma plume expands and cools very quickly in the first microsecond from the laser shot whereas, with the buffer gas, the plasma expansion slows down and the its shape is modified.

Indeed, as confirmed by angular distribution measurement, in vacuum condition plasma has the characteristic plume shape, whereas in gas pressure it has more rounded shape.

On the other hand, independently from the buffer gas pressure, the target remains hot even at high delay times.

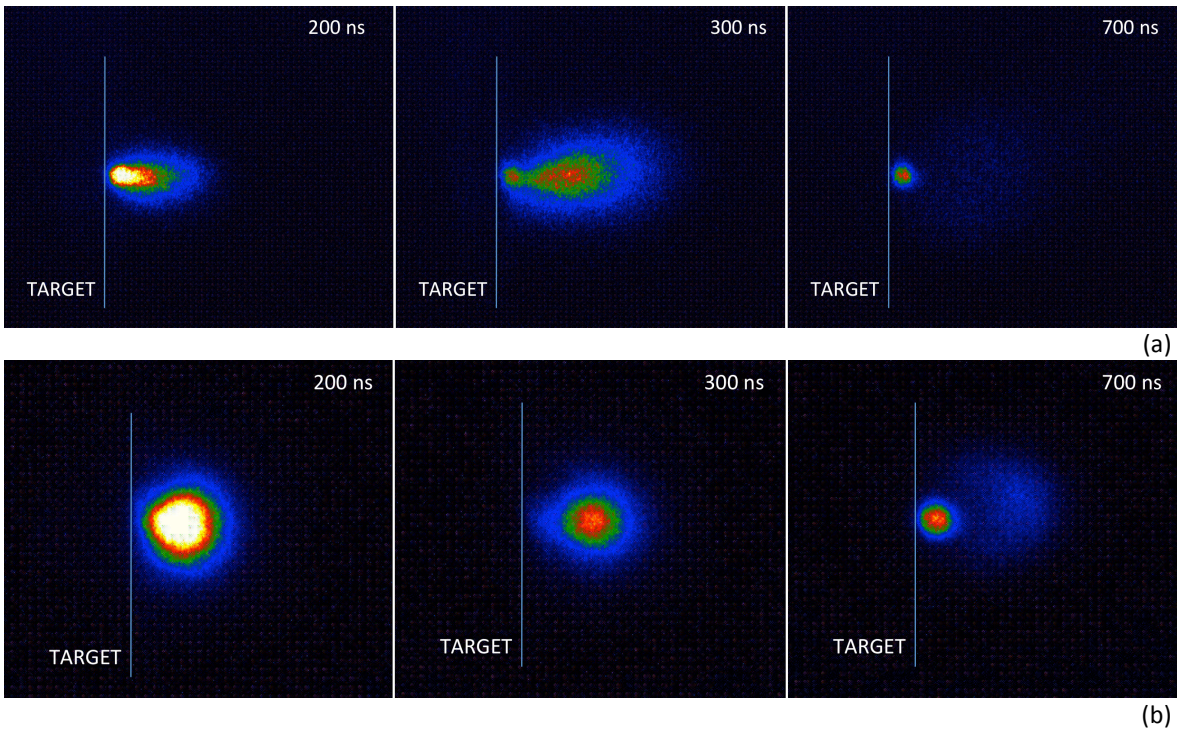

Fig. 6.13.: The plasma evolution of FeLCP in vacuum condition (a) and at 100 PA argon (b) acquired at different delay time, with gate of 100 ns

Furthermore, in both cases, a second emission from the target can be detected at longer delays from the laser pulse. Using a higher gate (10 μs), indeed, a second plasma emission is visible, due to the expulsion of small fragments or particulate in the form of molten droplets from the target.

The following images (Fig. 6.14.) refer to the evolution of the plume in vacuum and at 100 Pa of Ar obtained by varying the delay times and gate time of 10 µs:

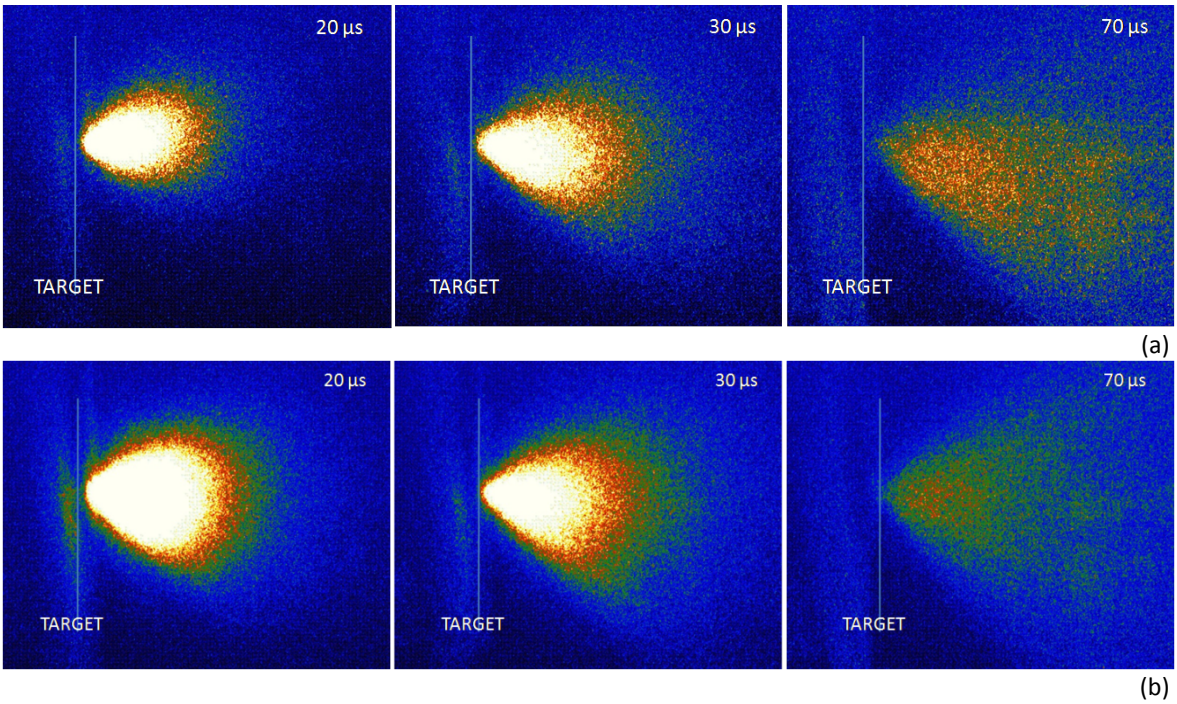

Fig. 6.14.: The plasma evolution of FeLCP in vacuum condition (a) and at 100 Pa Ar (b) acquired at different delay time, with gate of 10 µs

This type of ejection is often associated to a black body-like continuous emission spectrum [48] but in our case such a spectrum has not been detected, probably due to the relatively low temperature of the particles.

In addition, observing the evolution of plume in the presence both of the gaseous environment and the substrate, it was possible to clarify some aspects of the deposition and growth mechanism of thin films.

For this reason ,the images of plumes are acquired in the exact deposition condition, i.e. in the presence of the stainless steel substrate at a distance of 1 cm.

In vacuum, after a few hundred nanoseconds (around 300 ns) the plasma already hits the steel substrate and settles on it. The emission lasts some microseconds after laser pulse (2/3 µs).

With buffer gas, the plasma takes much longer to reach the substrate because of plasma confinement.

After 500 ns, indeed, the plasma has not yet encountered steel but, once reached it, remains stuck for a long time, cools down and then heats again to a very high delay (15 μs).

Thus the presence of gas lead to a much longer lasting plasma emission than that obtained at 10^{-3}Pa.

In vacuum conditions, the plume has a free expansion whereas, in the case of a buffer gas, the free expansion lasts until the pressure of the plume decreases significantly because of the background gas, that acts as a piston.

In a background gas the high plume pressure initially drives the ablated atoms away from the target as a free expansion towards the background gas, but subsequently the plume is slowed down by the background gas.

The slowing down of the plume leads to a pronounced shock-wave behavior in and outside the contact front between the ablation plume and the background gas [45].

In this case, the plume slows down and is confined in the background gas as a sphere stopping its motion for a tens of microseconds.

In addition to the pressure confinement, the plasma plume is strongly locked in substrate direction as a result of the close presence of steel foil, fixed at 1 cm.

In this way, the plume blocked may be slowly mixed with the background gas.

At the end, some of the plume atoms are collected on a substrate and grow as a film.

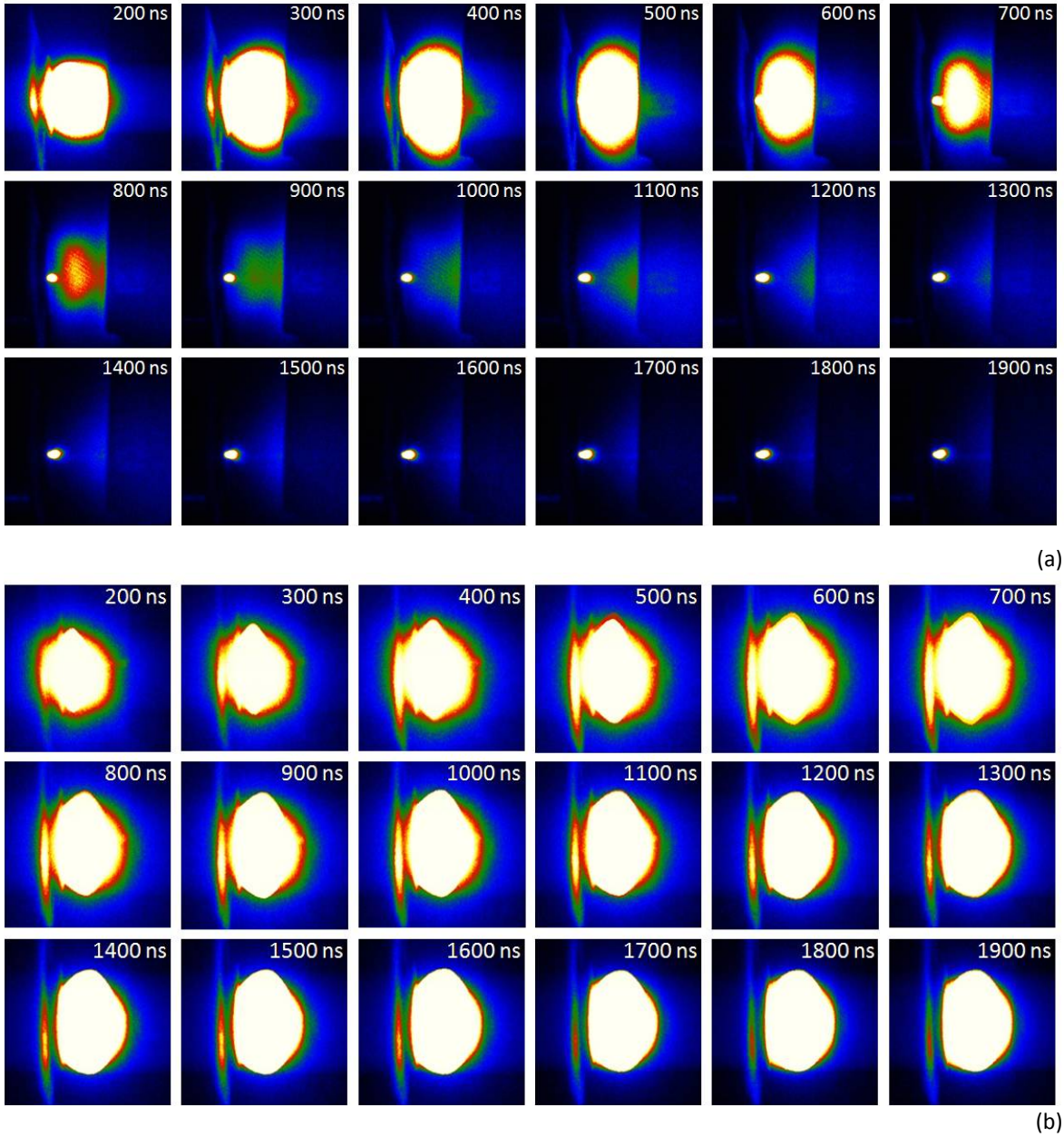

Fig. 6.15.: The plasma evolution of FeLCP in vacuum condition (a) and at 100 Pa Argon (b) acquired with gate of 100 ns

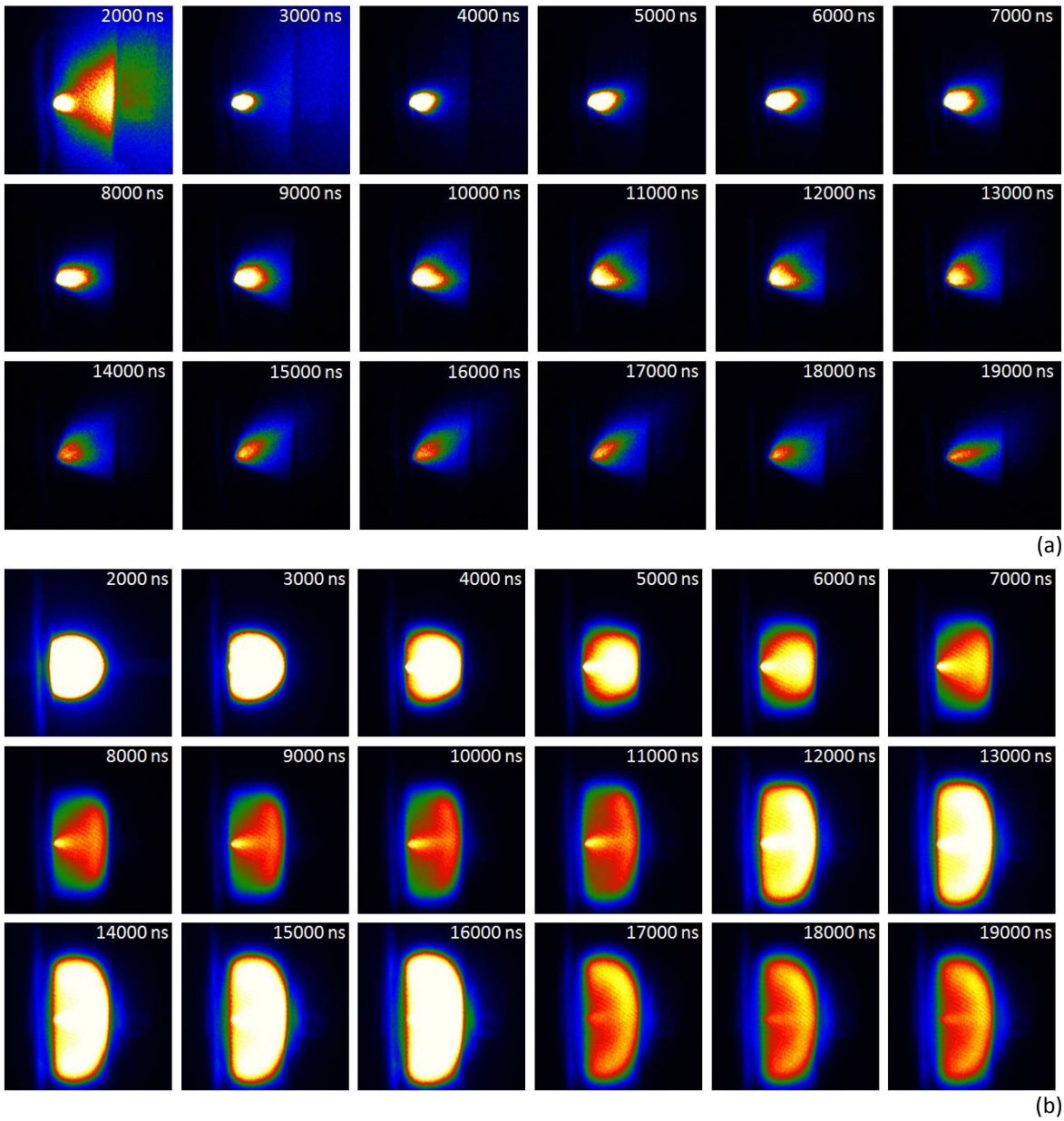

Fig. 6.16.: The plasma evolution of FeLCP in vacuum condition (a) and at 100 Pa Argon (b) acquired with gate of 1000 ns

The differences in space and time evolution of plasmas have an impact on morphology and cristallinity of thin films obtained, as explained in next section.

6.6. Thin film characterization

The FeLCP films deposited in vacuum (1.5 x 10^{-4} Pa) and at a 100 Pa of gas pressure of oxygen or argon, starting from a target with a composition corresponding to $LiCo_{0.9}Fe_{0.1}PO_4$ are characterized by different techniques, namely TEM, SEM and XRD.
In the following section, the details of the instruments are described.

6.6.1. Instrumental set up for thin film characterization

6.6.1.1. Transmission Electron Microscopy (TEM)

The first steps of the films growth has been characterized by Transmission Electronic Microscope (TEM). In this work, TEM measurements has been performed by High – Resolution (HRTEM) Fei-TECNAI G2 20 TWIN (Fig. 6.17), operating at 200 kV, and the material was deposited on holey carbon coated copper grids. TEM is used to study the first step of thin film formation, pointing out the individual particles ablated from the target.

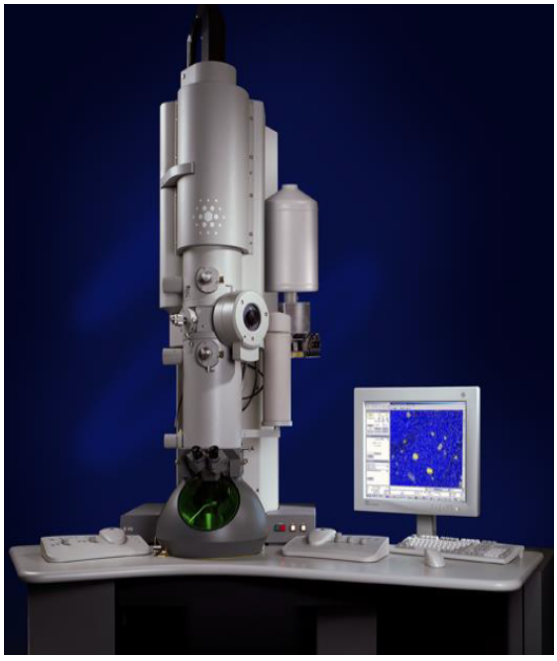

Fig. 6.17.: Transmission electron microscope Fei-TECNAI G2 20 TWIN

The electronic microscope employs an electron beam as radiation source and, because the resolution is inversely proportional to the radiation source wavelength, it is characterized by very high resolution, in this case the resolving power of this instrument is of about 0.2 nm.

In a TEM microscope, the electron beam passes through a vacuum column and then completely crosses the sample, that has to be an ultra – thin sample, with a thickness ranging from 50 to 500 nm.

The image is obtained after the interaction of the electrons transmitted through specimen. The electron beam strikes a fluorescent screen and a real and magnified image, in black and white, of the portion of the sample, previously crossed, is projected on it.

For these experiments, the sample are prepared by placing a holey carbon – coated copper grid, as a substrate, and deposited on it for 10 minutes.

6.6.1.2. Scanning Electron Microscope (SEM)

The morphology of the films is carried out using a Scanning Electron Microscope (PHILIPS-FEI ESEM XL 30) equipped with an Energy Dispersive X-Ray Spectroscopy (EDX) apparatus, which has boron as its first detectable element (Fig. 6.18.).

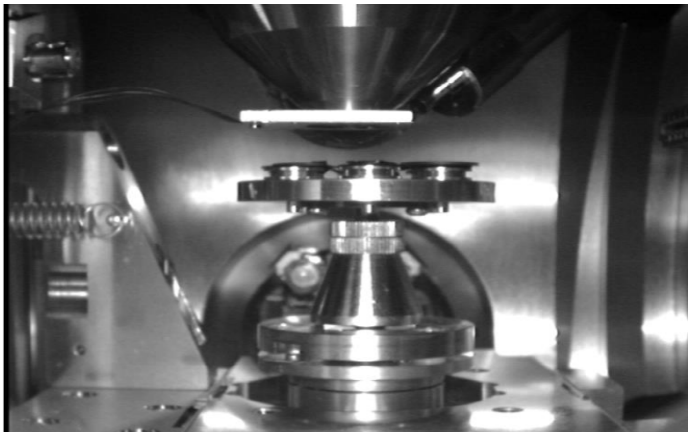

Fig. 6.18.: Chamber inside of Scanning electron microscope PHILIPS-FEI ESEM XL 30.

The electron emitter, a LaB_6 crystal, the resolution of this instrument is 4 nm and the emission power value can reach 30 keV.

When the high energy electron beam is focused on the surface, different ‘‘particles’’ are emitted from the sample, detected and converted in electrical signal.

The magnified images are obtained from the secondary electrons (SE) of the sample, that derive from the inelastic collisions of the electronic beam on the sample.

The quantity of emitted SE is a function of the angle between the incident electron beam and the sample surface, hence different SE signals are related to different topography of the surface.

The SEM allows to obtain a bidimensional images of the sample surface and of its section analyzing the secondary and back – scattered electrons.

The images obtained are in shades of gray, according to different surface orientation.

6.6.1.3. X – Ray Diffractometer (XRD)

The films crystallinity has been evaluated by X-ray diffraction (XRD, Siemens D5000), using a Cu $K\alpha_1$ radiation (Fig. 6.19.).

XRD is based on the scattering of the electromagnetic radiation hitting the sample.

The scattering of the radiation is the variation of the wave trajectory after the interaction with another wave or particle.

Unlike the reflection and refraction phenomena, characterized by an ordered deflection process, in the case of diffraction the deflection occurs randomly.

A XRD spectrum can be obtained thanks to the coherent interaction of all the scattered electromagnetic waves by the atoms belonging to the same family of lattice planes.

The XRD technique presupposes that the sample would be crystalline, i.e. characterized by a long range ordered disposition of atoms.

The interpretation of a XRD spectrum allows to obtain different information, as the repetition units of the crystalline lattice.

Fig. 6.19.: X – ray diffractometer Siemens D 5000

6.6.2. Deposition mechanism and thin film growth.

The characteristics of the deposited films are clearly related to the mechanism of material deposition on the substrate that, in turn, depends strictly on characteristics of the plasma plume.Comparing the SEM images (Fig.6.20.) of films deposited at a pressure of 100 Pa of oxygen with those obtained at 10^{-4} Pa, the morphology are significantly different.

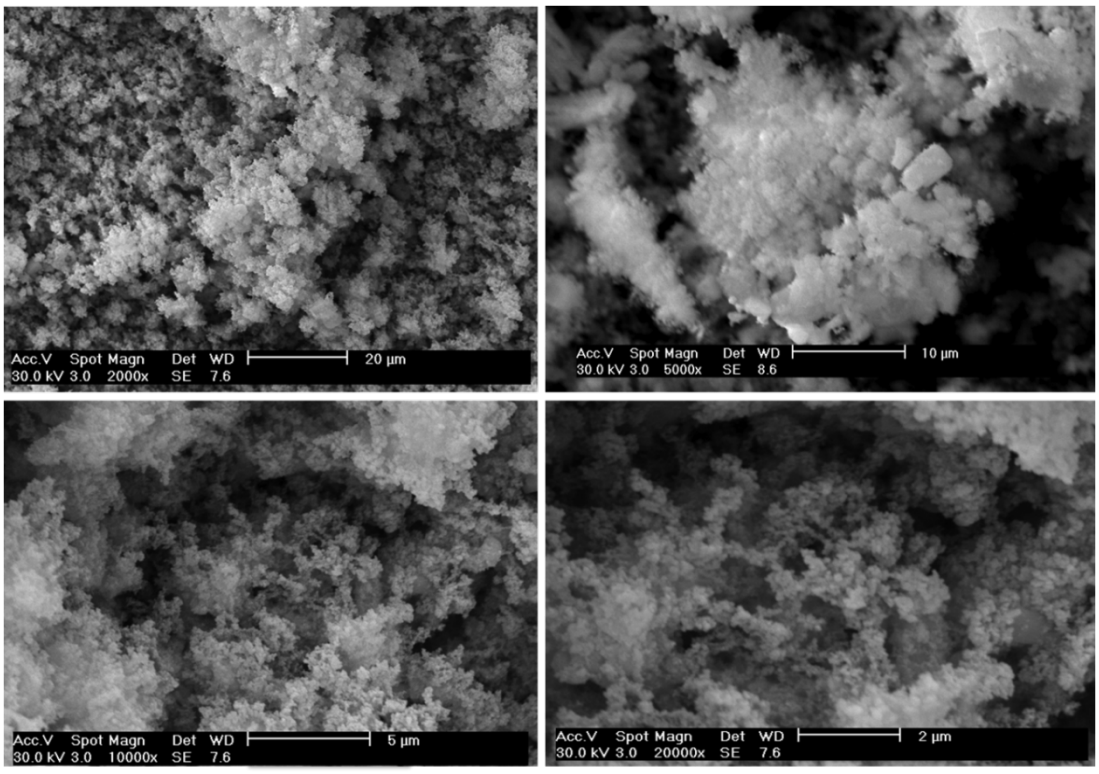

(a)

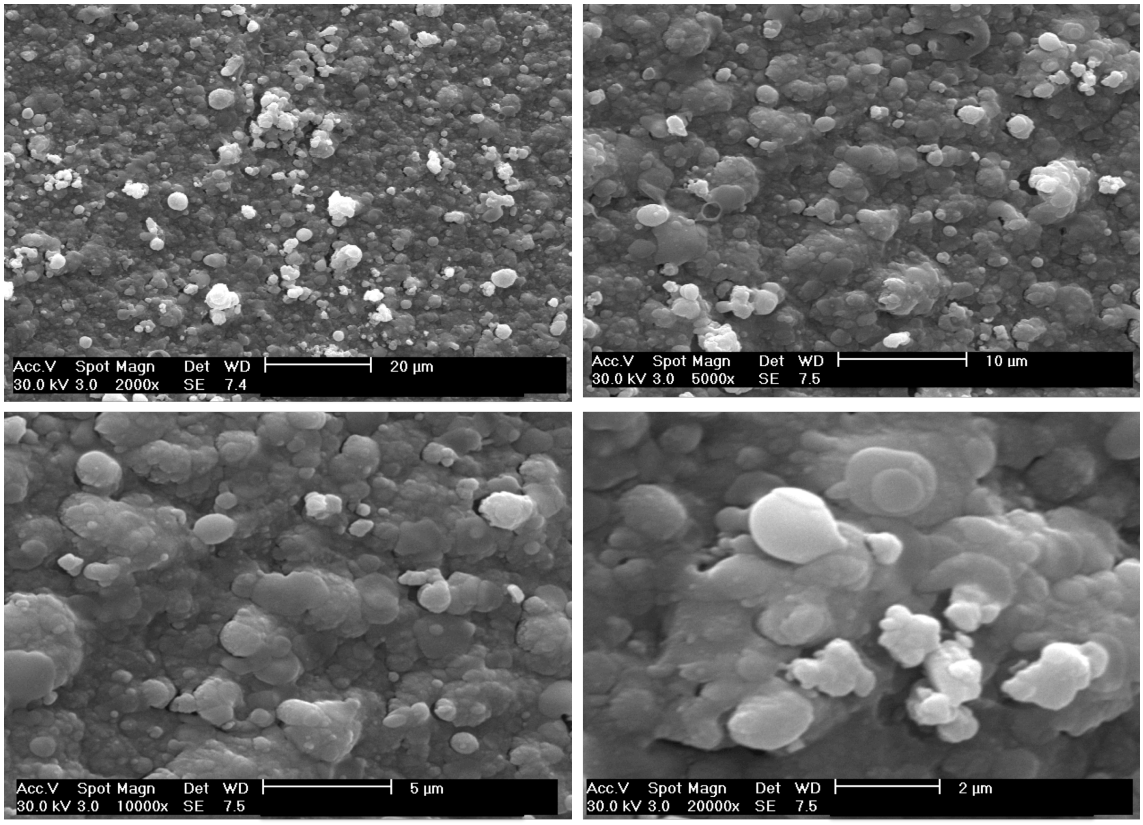

(b)

Fig. 6.20.: The SEM micrographs (a) are obtained at 100 Pa of oxygen and shows the presence of crystalline structures on the surface. (b) areobtained at pressure of $1.5 \cdot 10^{-4}$ Pa and shows few crystalline structures and a large number of microscopic particles expulsed from target.

From SEM images, both in vacuum and in gas, the films are compact and the surface seems to be formed by the coalescence of a large number of nano and micro particles. The only difference in the morphology among the films deposited in oxygen pressure (at 100 Pa) and in vacuum, is the presence, in the first case, of crystalline structures on the surface. These structures are completely absent in the case of the films deposited in vacuum.

This different morphology can be explained taking into account that the addition of gas may produces two effects on the expansion and evolution of the plasma such as a decrease of the kinetic energy of the species that compose it and a confinement into a smaller volume than the free expansion in the vacuum.

These conditions promote a different thin film growth mechanism: in presence of the buffer gas, the nucleation and the condensation of clusters and nanoparticles from the

plasma is favored, also due to the short target-substrate distance, which further increases the confinement of the plume already induced by the pressure of gas.

On the other hand, for the films deposited in vacuum, the deposition mechanism is linked to the coalescence of micro and nanoparticles mainly ejected directly from target as droplets or molten material.

The possibility of obtaining stoichiometric thin film of multicomponet target is also confirmed by the EDX analyses, indeed, the spectrum obtained at 100 Pa show that the Co/Fe molar ratio is exactly 9 (Fig. 6.21.).

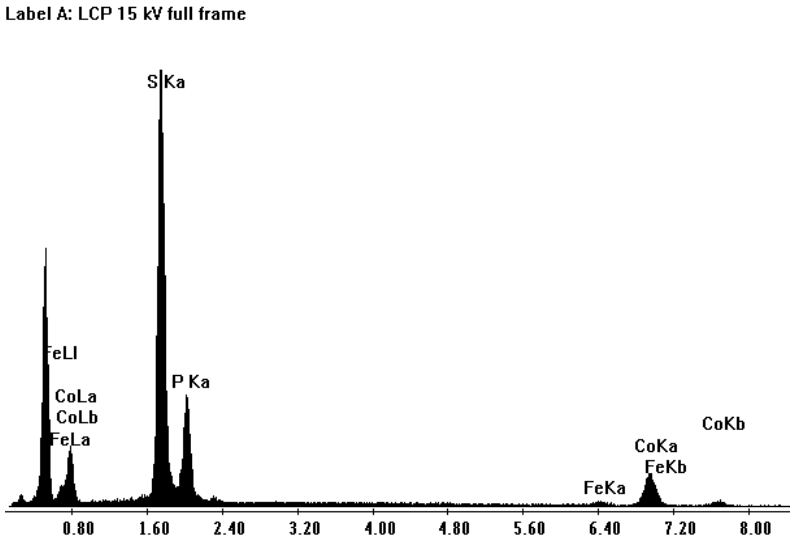

Element	wt%
P K	27.53
Fe K	7.15
Co K	65.32
Total	100.00

Fig. 6.21.: EDX spectra of FeLCP thin film obtained at 100 Pa Oxygen on Si substrate

All of these factors could therefore explain the higher degree of crystallinity of FeLCP thin films deposited in pressure conditions, as shown by the XRD diffractrogramms.

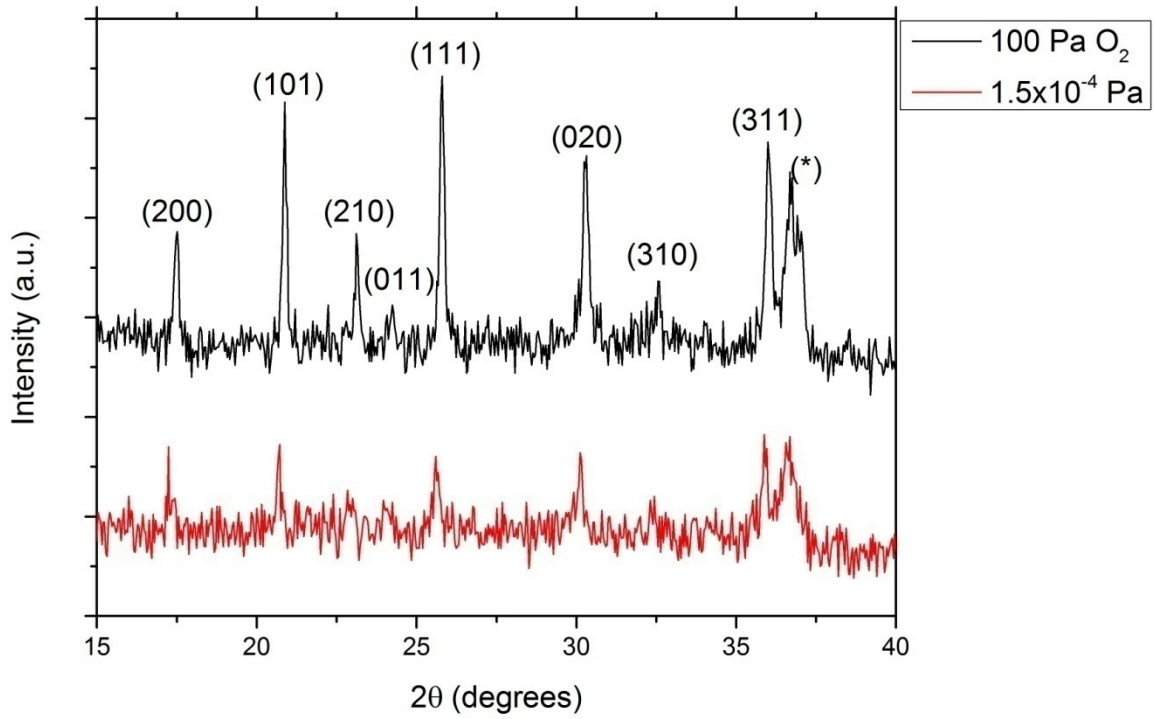

Fig. 6.22.: XRD spectra of the films deposited on steel at 100 Pa of oxygen and in vacuum condition.

The effect of plasma confinement, due to increase of gas pressure, on the film cristallinity has been confirmed compared two spectra obtained.

The Fig. 6.22. shows the XRD spectra of thin film deposited at 100 Pa of oxygen and in vacuum condition. In XRD spectra obtained, all peaks correspond to reflections of crystalline planes of FeLCP, as showed in the next table (Table 6.3.).

2θ (degrees)	**Crystalline planes**
17.36	(200)
20.72	(101)
23.00	(210)
23.64	(011)
25.68	(111)
30.20	(020)
32.52	(301)
35.96	(311)

Table 6.3.: XRD peaks and correspondent crystalline plane of FeLCP obtained at 100 Pa and 1 Pa of oxygen

Only the peak at 2θ = 36.84 does not corresponds to FeLCP phase but it can be assigned to iron oxide and, probably, is due to a reaction between the steel substrate and the oxygen present in the plasma produced by laser ablation of the FeLCP target.

This assignment has been made taking into account that this peak is not present neither in the spectrum of the steel substrate nor in the spectra of the films deposited in the same conditions on Si.

However, the deposition mechanism through condensation of the nanoparticles from the plasma in the presence of a buffer gas is also favoured by the substrate position, as highlighted by ICCD images of the plasma with gate 1000 ns.

In fact, in the presence of the substrate and with a gas pressure of 100 Pa, the plasma emission lasts up to 140 μs before quenching (Fig.6.16(b)), while in the same conditions but without substrate it is quenched after about 40 μs (Fig.6.15(b)).

In conclusion, the high degree of cristallinity seems to depend strongly on the mechanical confinement of the pressure and the substrate.

From the overall data it is evident the importance of the gas pressure in order to obtain crystalline thin films.

However, the type of gas may affects the crystallinity because the oxygen gas role could influence the dynamics of the expanded plasma produced by the laser ablation and also restore potential losses of oxygen from the target.

To verify these hypotheses the diffractogramm is recorded also on a thin film deposited at 100 Pa of argon, that is a non reactive gas, using the same experimental condition used before for the experiments in oxygen (Fig.6.23.).

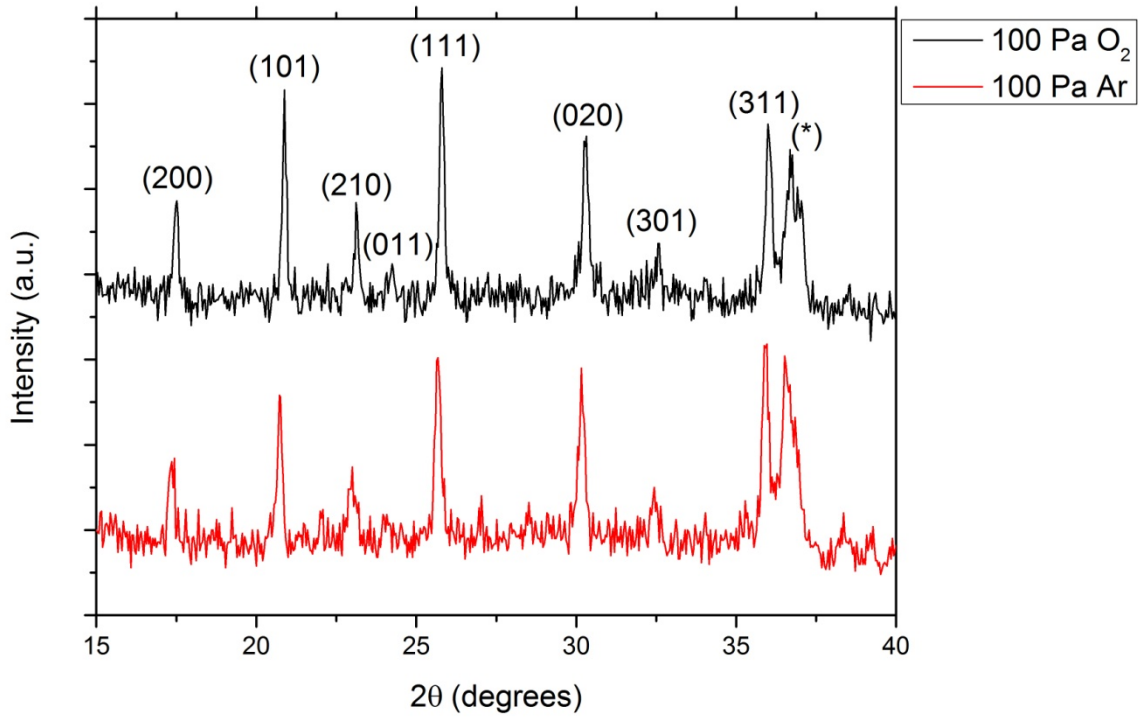

Fig. 6.23.: XRD spectra of the films deposited on steel at 100 Pa of oxygen and at 100 Pa of argon

Comparing this spectrum with that obtained in oxygen atmosphere is possible to see that they are very similar so deducing that the reactive properties of oxygen seem to play no role in the film characteristics.

Moreover, also in the film deposited in Ar atmosphere the peak at 2θ = 36.84 is still present, confirming that the substrate oxidation is due to oxygen from the decomposition of the substrate under the action of the laser beam.

The XRD analysis also can be used to determine the size of the crystallites using the Scherrer formula:

$$\tau = \frac{K\lambda}{\beta\cos(\vartheta)} \qquad \text{(eq. 6.3.)}$$

where: K is a coefficient that corresponds to the crystallite form, λ is incident wavelength, β corresponds to the FWHM of considered peak.

In this case, K is equal to 0.9, λ corresponds to 1.54 Å and the β values (FWHM) are calculated using the most intense peak that corresponds to (111) crystalline plane of the olivine phase.

The results, shown in table 6.4., indicate that a higher pressure produces larger crystallites.

Gas pressure	**Medium size of crystallites**
10^{-3} Pa	33 nm
100 Pa O_2	49 nm
100 Pa Ar	50 nm

Table 6.4: Medium size of the crystallites obtained at different pressure conditions

Further confirmation that the morphology of the films deposited in the same conditions but in the different gases is the same, is given by the SEM image of the cross section (Fig.6.24.) of a film deposited on steel in Ar atmosphere (p = 100 Pa).

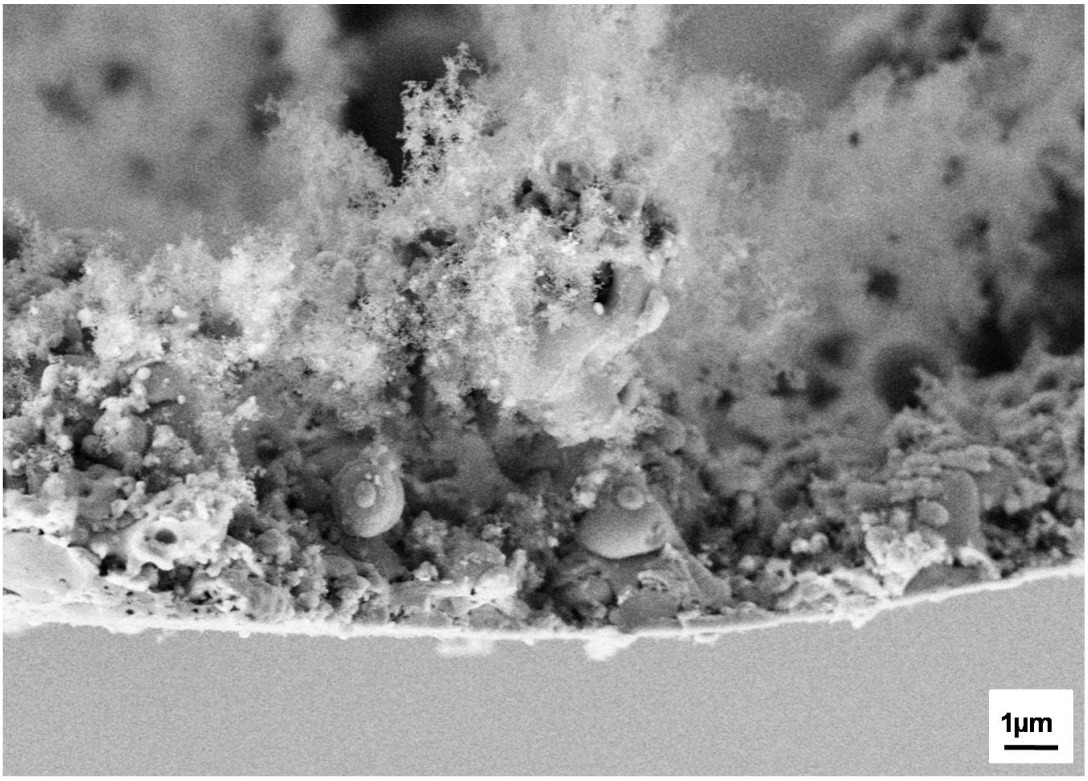

Fig. 6.24.: SEM micrograph of the cross section of a film deposited on steel at 100 Pa of argon.

The film seems to be formed by both solidified melted particles and crystals, which have characterized by the same composition, as evidenced by the elemental EDX maps of the cross section, reported in Fig. 6.25.

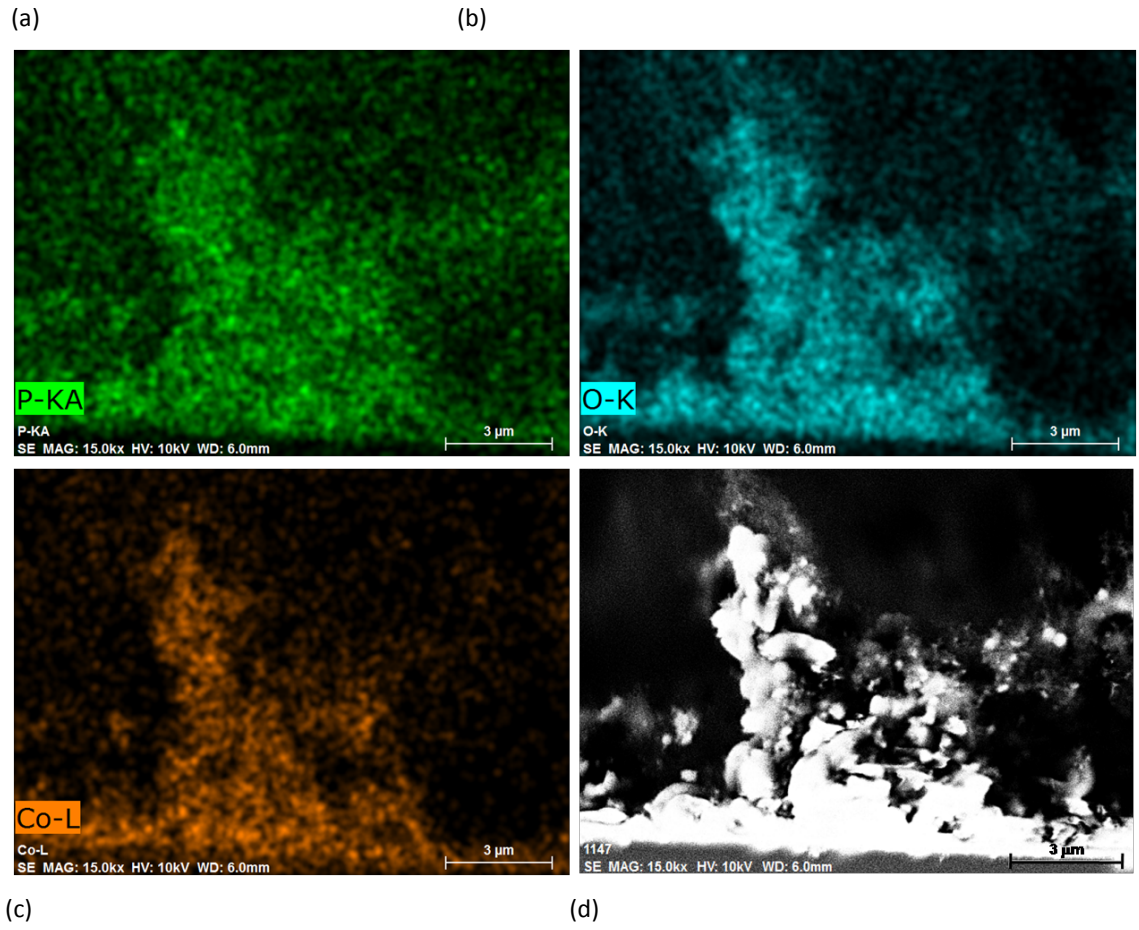

Fig. 6.25.: EDX maps of the elements of in the film the cross section: (a) Phosphorous, (b) Oxygen, (c) Cobalt. The SEM image (secondary electrons) of the cross section is reported in (d).

All of EDX maps show a uniform distribution of different elements, confirming that the ablation process is stoichiometric. In order to understand the first steps of the growth of a film, TEM analysis are made on the film deposited with Ar pressure of 100 Pa and in vacuum condition.

The TEM images, acquired at pressure of 100 Pa Ar, evidence the presence of two types of particles. The larger particles (with diameters ranging from 100 nm to 1 µm) have been clearly emitted as melted droplets from the target, while the smaller one, of nanometric

size, could derive from condensation from the plasma (Fig.6.26.). Some of these nanometric particles show crystalline planes which distances, calculated using Fourier method, correspond to (301) and (311) planes of orthorhombic FeLCP (Fig.6.27.).

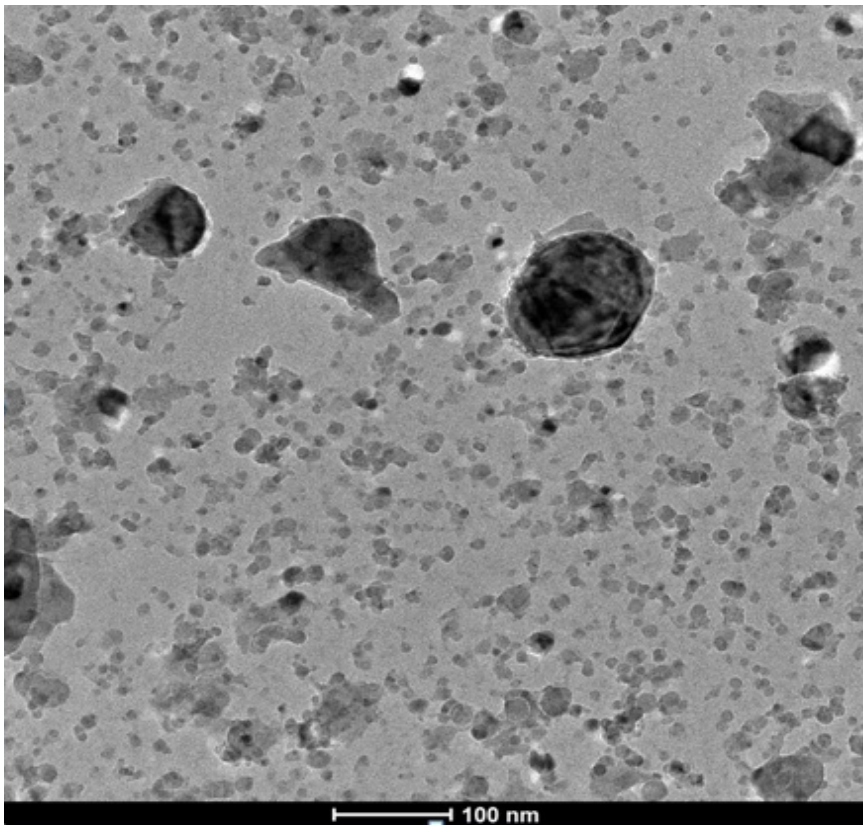

Fig. 6.26.: TEM image showing the first steps of the growth of films deposited with an Ar pressure of 100 Pa

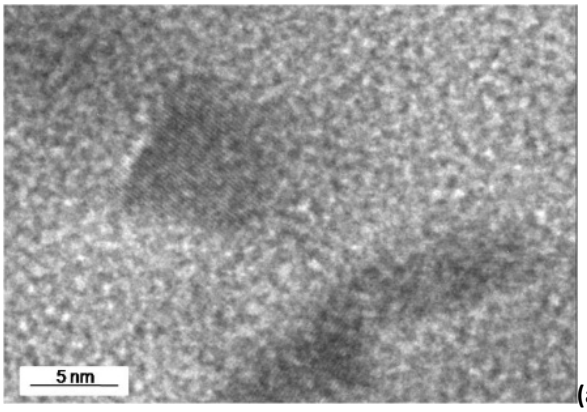

(a)

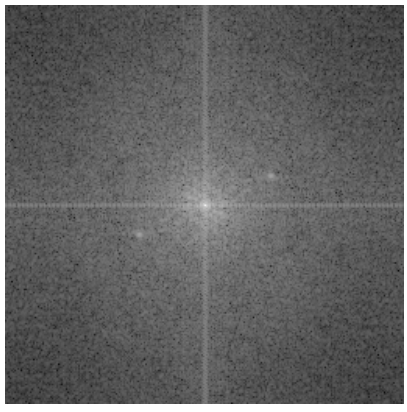

(b)

Fig. 6.27.: TEM image at higher magnification showing NPs (a); 2D FFT of a NP where the bright diffractions pots allow to evaluate a lattice spacing of 0.27 nm with distance corresponding to (301) planes of orthorhombic FeLCP (b).

In vacuum conditions, the TEM images shows only the presence of particles with micrometric size with a very small quantity of particles with nanometric size (Fig.6.28.).

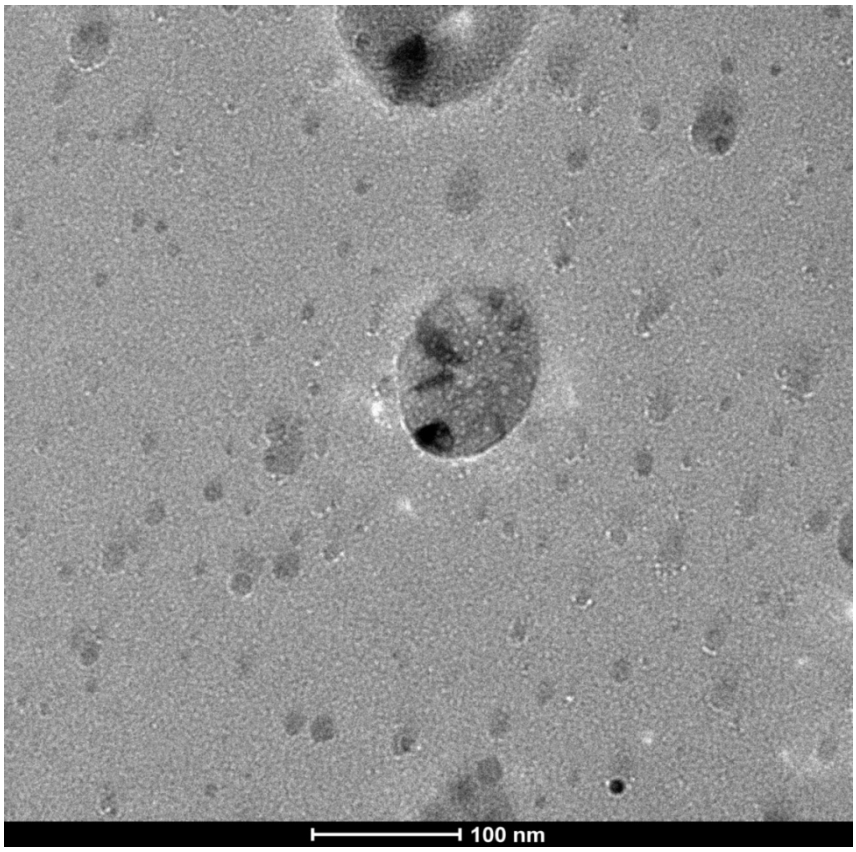

Fig. 6.28.: TEM image showing the first steps of the growth of films deposited in vacuum condition

A very peculiarity of this work is the crystallinity of thin films obtained at room temperature.

In literature [27]–[29], [31], [33], [35]–[39], [43], [49] to obtain a crystalline growth of thin film, the deposition is carried out at high temperature or with a post annealing treatments.

It has been shown, generally, that the films obtained at room temperature does not present a diffraction profile, pointing out their amorphous state and an ex situ thermal treatment is necessary for increasing the crystallinity with the disadvantage of obtaining also a undesirable secondary phases.

However, the films obtained in this work are annealed ex situ in Argon atmosphere at 700 °C for 2 h in order to check whether a thermal treatment can further improve or not crystallinity (Fig.6.29.).

Comparing X-Ray diffraction patterns of the thin films deposited on Stainless Steel substrates at room temperature and annealed at 700 °C (fig....), it is evident that, in the latter case, other secondary reflection peaks, probably due to another phase formation, are present.

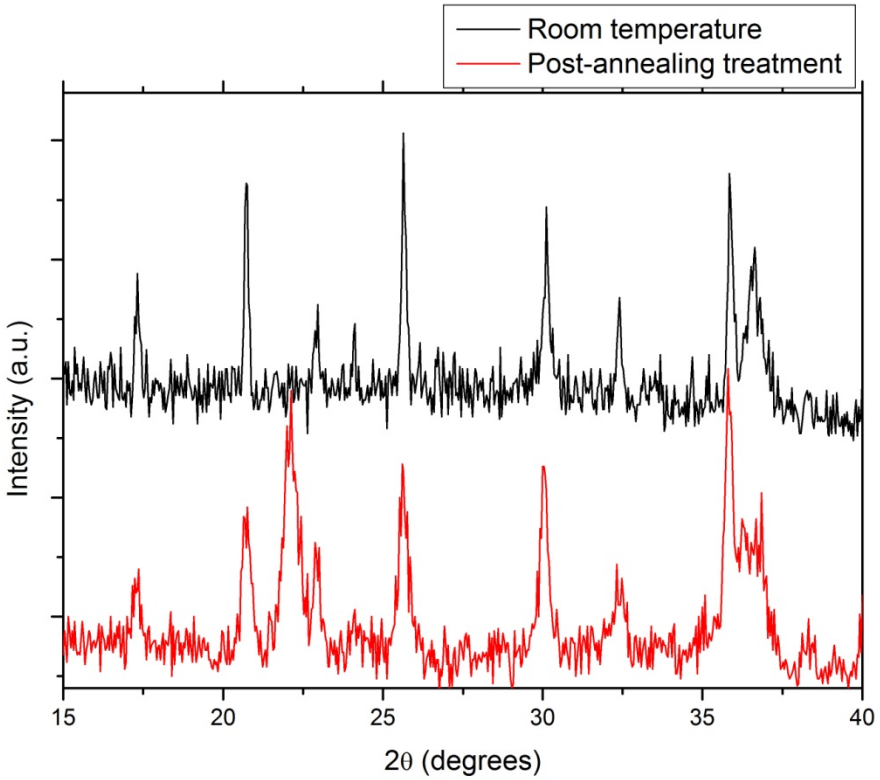

Fig. 6.29.:XRD spectra of the films deposited at room temperature (a) and with post annealing treatment (b)

To conclude, taking into account these results, the PLD procedure seems to be adequate for obtaining desired thin films with one step deposition at room temperature.

The preparation using PLD without any type of thermal treatment is an advantage in terms of cost-effective equipment and of the simplicity of process.

The condition of pulsed laser deposition for fLCP thin films are optimized to obtain films with pure olivine phase.

The crystallinity, surface morphology and, consequently, the electrochemical properties of these thin films are strongly influenced by pressure of surrounding gas.

6.6.3. Electrochemical characterization

Finally, an electrochemical characterization has been carried out on FeLCP thin films, deposited at 10^2 Pa on a stainless steel foil.

This films are tested in lithium cells in galvanostatic cycling, in which, the charge and discharge current are often expressed as a C-rate, calculated from the battery capacity.

The C-rate is a measure of the rate at which a battery is charged or discharged relatively to its maximum capacity.

In this work, a current density of 2 μAcm^{-2} (corresponding approximately to a 1h for a full charge/discharge, 1C current rate) between 5 and 3.5 V is employed.

The voltage profile of the lithium cell assembled is shown in Fig.6.30. in comparison to the voltage profile obtained from the starting bulk material for a similar 1C current rate.

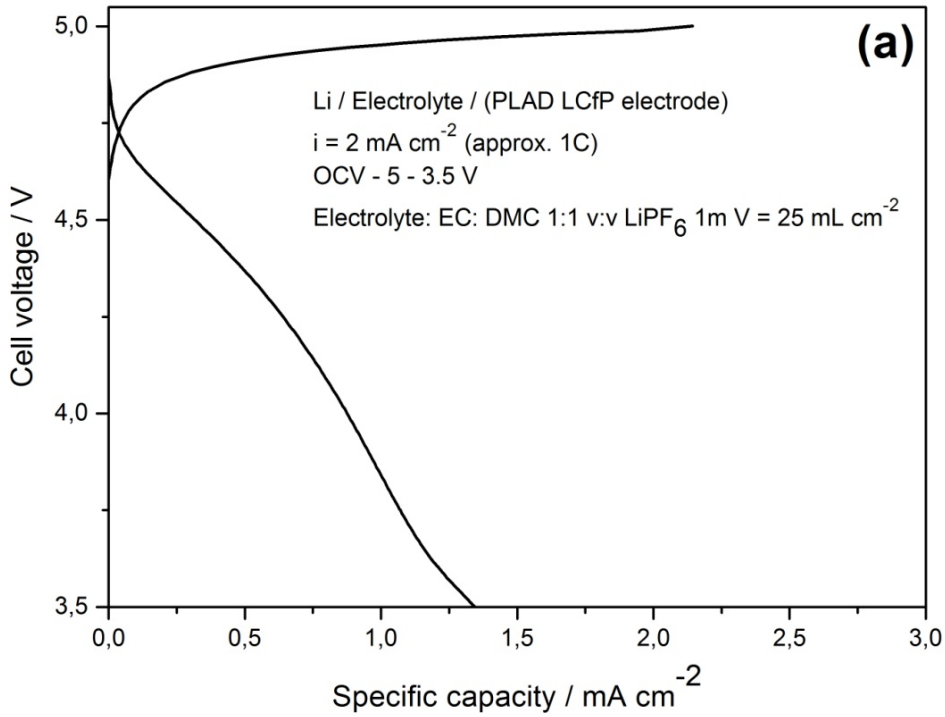

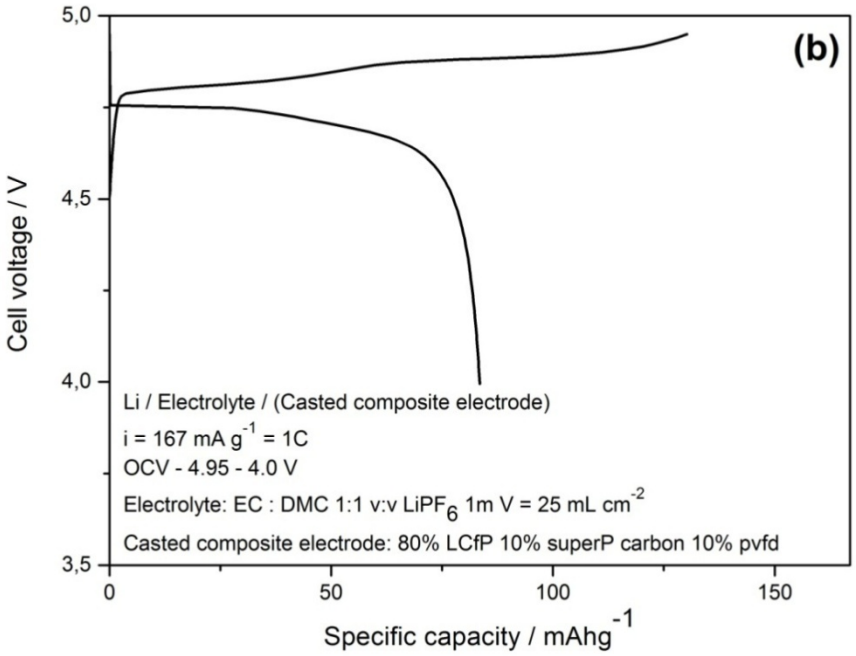

Fig. 6.30.: Voltage profile of (a) lithium cell assembled using the LCfP microelectrode and (b) voltage profile obtained from the starting bulk material for a similar 1C current rate.

It is important to stress that the capacity normalization for the two set of data, i.e. microelectrode vs. bulk electrode, is unavoidably different due to the highly questionable evaluation of the real amount of deposit from PLD, approximately 0.1-0.2 mg cm^{-2}.

In fact, the inaccuracy on the mass evaluation massively impacts on the corresponding error on the microelectrode performance expressed in terms of $mAhg^{-1}$ (approx. 100%). Thus, it is preferable to show the two set of data with different specific capacity normalization.

However, as the two galvanostatic tests have been carried out at similar current rates, it is possible a qualitative comparison between the electrode responses in terms of profile shape.

The microelectrode is able to give a reversible galvanostatic response even though the coulombic efficiency (i.e. the ratio between the capacity exchanged in discharge and charge) is only slightly above 50% in the first cycle.

Upon charge the shape of the voltage profile is comparable with the bulk material, i.e. a long and stable plateau at about 4.8 - 4.9 V.

On the other hand in discharge the bulk material shows a reversible plateau at 4.5-4.7 V whereas the microelectrode exhibits a decreasing slope ranging from 4.6-3.5 V.

This different behavior may be related to the massive impact of the possible accumulation of degradation by-products (solid electrolyte interphase, SEI) over the surface of the microelectrode.

In fact the working voltage of the FeLCP material is very close the upper limit of the stability window of the used electrolyte and solvent degradation has been reported to spontaneously occur on the surface of charged electrodes. However in the case of microelectrodes the SEI formation may have a more severe impact on the electrochemical response. In fact, compared to the bulk electrodes, microelectrodes unavoidably suffer of a smaller electronic conductivity, due to the lack of any carbonaceous conductor, and a poor mechanical stability due to the absence of any polymeric binder. In FeLCP microelectrodes at high potentials the electrode volume changes due to the lithium extraction/insertion from/into the crystal latticeis mechanically un-buffered: this effect may lead to particle pulverization and thus to the exposure of new bare surface able to react with the electrolyte. This continuous precipitation of electronically insulating organic byproducts over the microelectrode particles may reflect on the overall microelectrode resistance and explain the increase of the overvoltage upon discharge.

6.7. References

[1] B. Scrosati and J. Garche, “Lithium batteries: Status, prospects and future,” *J. Power Sources*, vol. 195, pp. 2419–2430, 2010.

[2] A. De Giacomo, M. Dell’Aglio, R. Gaudiuso, S. Amoruso, and O. De Pascale, “Effects of the background environment on formation, evolution and emission spectra of laser-induced plasmas,” *Spectrochim. Acta - Part B At. Spectrosc.*, vol. 78, pp. 1–19, 2012.

[3] R. Teghil, A. De Bonis, A. Galasso, A. Santagata, P. Villani, and D. J. Sordelet, “Role and importance of nanoparticles in femtosecond pulsed laser ablation deposition of Al-Cu-Fe quasicrystal,” *Chem. Phys. Lett.*, vol. 438, pp. 85–88, 2007.

[4] L. D’Alessio, A. De Bonis, A. Galasso, A. Morone, A. Santagata, R. Teghil, P. Villani, and M. Zaccagnino, “Characterisation of ultrashort pulse laser ablation of SmBaCuO,” *Appl. Surf. Sci.*, vol. 248, pp. 295–298, 2005.

[5] J. V. Rau, R. Teghil, D. Ferro, A. Generosi, V. Rossi Albertini, M. Spoliti, and S. M. Barinov, “Deposition and characterisation of MoSi2 films,” *Thin Solid Films*, vol. 518, pp. 2050–2055, 2010.

[6] L. D’Alessio, A. Galasso, A. Santagata, R. Teghil, A. R. Villani, P. Villani, and M. Zaccagnino, “Plume dynamics in TiC laser ablation,” *Appl. Surf. Sci.*, vol. 208–209, pp. 113–118, 2003.

[7] R. Teghil, L. D’Alessio, A. Santagata, D. Ferro, and G. De Maria, “Pulsed laser ablation of Nd and Pr carbides,” *Appl. Surf. Sci.*, vol. 208–209, pp. 119–124, 2003.

[8] D. Ferro, J. V. Rau, V. Rossi Albertini, A. Generosi, R. Teghil, and S. M. Barinov, “Pulsed laser deposited hard TiC, ZrC, HfC and TaC films on titanium: Hardness and an energy-dispersive X-ray diffraction study,” *Surf. Coatings Technol.*, vol. 202, pp. 1455–1461, 2008.

[9] J. V. Rau, R. Teghil, A. De Bonis, A. Generosi, B. Paci, R. Generosi, M. Fosca, D. Ferro, V. Rossi Albertini, and N. S. Chilingarov, “Pulsed laser deposition of hard and superhard carbon thin films from C60 targets,” *Diam. Relat. Mater.*, vol. 19, pp. 7–14, 2010.

[10] A. De Bonis, A. Galasso, N. Ibris, A. Laurita, A. Santagata, and R. Teghil, “Rutile microtubes assembly from nanostructures obtained by ultra-short laser ablation of titanium in liquid,” *Appl. Surf. Sci.*, vol. 268, pp. 571–578, 2013.

[11] S. Brutti and S. Panero, “Recent Advances in the Development of $LiCoPO_4$ as High Voltage Cathode Material for Li-Ion Batteries,” *Nanotechnol. Sustain. Energy*, pp. 67–99, 2013.

[12] N. Nitta, F. Wu, J. T. Lee, and G. Yushin, “Li-ion battery materials: Present and future,”

Mater. Today, vol. 18, pp. 252–264, 2015.

[13] R. Eason and D. P. Norton, "Pulsed laser deposition of thin films, applications-led growth, Edited by Eason R, 2007.

[14] Z. Li, D. Zhang, and F. Yang, "Developments of lithium-ion batteries and challenges of LiFePO4 as one promising cathode material," *J. Mater. Sci.*, vol. 44, pp. 2435–2443, 2009.

[15] N. V. Kosova, O. A. Podgornova, E. T. Devyatkina, V. R. Podugolnikov, and S. A. Petrov, "Effect of Fe^{2+} substitution on the structure and electrochemistry of $LiCoPO_4$ prepared by mechanochemically assisted carbothermal reduction," *J. Mater. Chem. A*, vol. 2, pp. 20697–20705, 2014.

[16] M. Haruta, S. Shiraki, T. Ohsawa, T. Suzuki, A. Kumatani, Y. Takagi, R. Shimizu, and T. Hitosugi, "Preparation and in-situ characterization of well-defined solid electrolyte/electrode interfaces in thin-film lithium batteries," *Solid State Ionics*, vol. 285, pp. 118–121, 2016.

[17] e J. H. K. and G. R. Yong-Mook Kang,*ac Yong-Il Kim,bc Min-Wook Oh,c Ri-Zhu Yin,d Youngmin Lee,a Dong-Wook Han,e Hyuk-Sang Kwon, "Structurally stabilized olivine lithium phosphate cathodes with enhanced electrochemical properties through Fe doping," *Energy Environ. Sci.*, vol. 4, pp. 4978–4983, 2011.

[18] N. N. Bramnik, K. Nikolowski, G. Baehtz, K. G. Bramnik, and H. Ehrenberg, "Phase transitions occurring upon lithium insertion-extraction of $LiCoPO_4$," *Chem. Mater.*, vol. 19, pp. 908–915, 2007.

[19] Y. Wang, B. Liu, Q. Li, S. Cartmell, S. Ferrara, Z. D. Deng, and J. Xiao, "Lithium and lithium ion batteries for applications in microelectronic devices: A review," *J. Power Sources*, vol. 286, pp. 330–345, 2015.

[20] S. Ferrari, M. Loveridge, S. D. Beattie, M. Jahn, R. J. Dashwood, and R. Bhagat, "Latest advances in the manufacturing of 3D rechargeable lithium microbatteries," *J. Power Sources*, vol. 286, pp. 25–46, 2015.

[21] D. Di Lecce, J. Manzi, F. M. Vitucci, A. De Bonis, S. Panero, and S. Brutti, "Effect of the iron doping in $LiCoPO_4$ cathode materials for lithium cells," *Electrochim. Acta*, vol. 185, pp. 17–27, 2015.

[22] H. Kim, T. E. Sutto, and A. Piqué, "Laser materials processing for micropower source applications: a review," *J. Photonics Energy*, vol. 4, p. 40992, 2014.

[23] C. W. Schneider and T. Lippert, "Laser Ablation and Thin Film Deposition," in *LASER PROCESSING OF MATERIALS - Fundamentals, Applications and Developments*, 2010, pp.

89–112.

[24] Y. Iriyama, M. Inaba, T. Abe, and Z. Ogumi, “Preparation of c-axis oriented thin films of $LiCoO_2$ by pulsed laser deposition and their electrochemical properties,” *J. Power Sources*, vol. 94, pp. 175–182, 2001.

[25] A. Rougier, K. A. Striebel, S. J. Wen, T. J. Richardson, R. P. Reade, and E. J. Cairns, “Characterization of pulsed laser-deposited LiMn2O4 thin films for rechargeable lithium batteries,” *Appl. Surf. Sci.*, vol. 134, pp. 107–115, 1998.

[26] C. Julien, E. Haro-Poniatowski, M. A. Camacho-Lopez, L. Escobar-Alarcon, and J. Jimenez-Jarquin, “Growth of $LiMn_2O_4$ thin films by pulsed-laser deposition and their electrochemical properties in lithium microbatteries,” *Mater. Sci. Eng. B Solid-State Mater. Adv. Technol.*, vol. 72, pp. 36–46, 2000.

[27] T. Matsumura, N. Imanishi, A. Hirano, N. Sonoyama, and Y. Takeda, “Electrochemical performances for preferred oriented PLD thin-film electrodes of $LiNi_{0.8}Co_{0.2}O_2$, $LiFePO_4$ and $LiMn_2O_4$,” *Solid State Ionics*, vol. 179, pp. 2011–2015, 2008.

[28] C. Ouyang, H. Deng, Z. Ye, M. Lei, and L. Chen, “Pulsed laser deposition prepared $LiMn_2O_4$ thin film,” *Thin Solid Films*, vol. 503, pp. 268–271, 2006.

[29] I. Yamada, T. Abe, Y. Iriyama, and Z. Ogumi, “Lithium-ion transfer at LiMn2O4 thin film electrode prepared by pulsed laser deposition,” *Electrochem. commun.*, vol. 5, pp. 502–505, 2003.

[30] F. Simmen, T. Lippert, P. Novák, B. Neuenschwander, M. Döbeli, M. Mallepell, and A. Wokaun, “The influence of lithium excess in the target on the properties and compositions of Li_{1+x} $Mn_2O_{4-\delta}$ thin films prepared by PLD,” *Appl. Phys. A Mater. Sci. Process.*, vol. 93, pp. 711–716, 2008.

[31] D. Albrecht, H. Wulfmeier, and H. Fritze, “Preparation and Characterization of c-$LiMn_2O_4$ Thin Films prepared by Pulsed Laser Deposition for Lithium-Ion Batteries,” *Energy Technol.*, vol. 4, pp. 1558–1564, 2016.

[32] K. Tang, J. Sun, X. Yu, H. Li, and X. Huang, “Electrochemical performance of $LiFePO_4$ thin films with different morphology and crystallinity,” *Electrochim. Acta*, vol. 54, pp. 6565–6569, 2009.

[33] J. Sun, K. Tang, X. Yu, H. Li, and X. Huang, “Needle-like $LiFePO_4$ thin films prepared by an off-axis pulsed laser deposition technique,” *Thin Solid Films*, vol. 517, pp. 2618–2622, 2009.

[34] F. Sauvage, L. Laffont, J. M. Tarascon, and E. Baudrin, “Factors affecting the

electrochemical reactivity vs. lithium of carbon-free $LiFePO_4$ thin films," *J. Power Sources*, vol. 175, pp. 495–501, 2008.

[35] F. Sauvage, E. Baudrin, L. Laffont, and J. M. Tarascon, "Origin of electrochemical reactivity enhancement of post-annealed LiFePO4 thin films: Preparation of heterosite-type $FePO_4$," *Solid State Ionics*, vol. 178, pp. 145–152, 2007.

[36] V. Palomares, I. Ruiz de Larramendi, J. Alonso, M. Bengoechea, A. Goñi, O. Miguel, and T. Rojo, "$LiFePO_4$ thin films grown by pulsed laser deposition: Effect of the substrate on the film structure and morphology," *Appl. Surf. Sci.*, vol. 256, no. 8, pp. 2563–2568, 2010.

[37] C. Yada, Y. Iriyama, S.-K. Jeong, T. Abe, M. Inaba, and Z. Ogumi, "Electrochemical properties of $LiFePO_4$ thin films prepared by pulsed laser deposition," *J. Power Sources*, vol. 146, pp. 559–564, 2005.

[38] F. Sauvage, E. Baudrin, L. Gengembre, and J. M. Tarascon, "Effect of texture on the electrochemical properties of $LiFePO_4$ thin films," *Solid State Ionics*, vol. 176, pp. 1869–1876, 2005.

[39] C. Legrand, L. Dupont, K. Tang, H. Li, X. J. Huang, and E. Baudrin, "Structural and textural characterization of $LiFePO_4$ thin films prepared by pulsed laser deposition on Si substrates," *Thin Solid Films*, vol. 518, pp. 5447–5451, 2010.

[40] H. Xia, L. Lu, and Y. S. Meng, "Growth of layered $LiNi_{0.5}Mn_{0.5}O_2$ thin films by pulsed laser deposition for application in microbatteries," *Appl. Phys. Lett.*, vol. 92, p. 11912, 2008.

[41] G. X. Wang, M. J. Lindsay, M. Ionescu, D. H. Bradhurst, S. X. Dou, and H. K. Liu, "Thin-film Electrodes Deposited By Laser Ablation," vol. 98, pp. 298–302, 2001.

[42] J. D. Perkins, C. S. Bahn, P. A. Parilla, J. M. McGraw, M. L. Fu, M. Duncan, H. Yu, and D. S. Ginley, "$LiCoO_2$ and $LiCo_{1-x}Al_xO_2$ thin film cathodes grown by pulsed laser ablation," *J. Power Sources*, vol. 81–82, pp. 675–679, 1999.

[43] V. Daramalla, T. R. Penki, N. Munichandraiah, and S. B. Krupanidhi, "Fabrication of $TiNb_2O_7$ thin film electrodes for Li-ion micro-batteries by pulsed laser deposition," *Mater. Sci. Eng. B Solid-State Mater. Adv. Technol.*, vol. 213, pp. 90–97, 2016.

[44] B. Yan, J. Liu, B. Song, P. Xiao, and L. Lu, "Li-rich Thin Film Cathode Prepared by Pulsed Laser Deposition," *Sci. Rep.*, vol. 3, p. 3332, 2013.

[45] J. Schou, "Physical aspects of the pulsed laser deposition technique: The stoichiometric transfer of material from target to film," *Appl. Surf. Sci.*, vol. 255, pp. 5191–5198, 2009.

[46] "NIST Database, National Institute Of Standard and Tecnology, Gaithersburg Md, USA, 2003, http://www.nist.gov," *NIST Database, National Institute Of Standard and Tecnology,*

Gaithersburg Md, USA, 2003, http://www.nist.gov.

[47] http: // www. cfa. harvard. edu/amp/ampdata. kurucz23/sekur. htm. Kurucz Atomic Spectral Lines Database.

[48] R. Teghil, L. D'Alessio, A. De Bonis, A. Galasso, N. Ibris, A. M. Salvi, A. Santagata, and P. Villani, "Nanoparticles and thin film formation in ultrashort pulsed laser deposition of vanadium oxide.," *J. Phys. Chem. A*, vol. 113, pp. 14969–74, 2009.

[49] H. Xia, L. Lu, and G. Ceder, "Substrate effect on the microstructure and electrochemical properties of $LiCoO_2$ thin films grown by PLD," *J. Alloys Compd.*, vol. 417, pp. 304–310, 2006.

Conclusions

The aim of this work has been dual: first of all, using femtosecond Nd: Glass laser, the CF inverse LIBS method has been optimized for the study of seven copper based certified standard.

This method allows to determine the plasma temperature using a single standard sample and consists in inverting the CF method for quantitative analysis.

However, in order to provide more accurate quantitative analysis, the correction with calibration curves has proved to be necessary.

The analytical performance of the inverse method has been tested for the systematic analysis of archaeological bronze artefacts, coming from three archaeological sites in Basilicata, and the LIBS data have been compared with those from classical calibration curve LIBS and with those from independent measurements performed by XRF.

The agreement among different series of data has been satisfactory for all ancient findings confirming the validity of the method.

The LIBS methodology has confirmed to be an useful technique for the elemental analysis of complex samples and, furthermore, thanks to the micro destructiveness of the femtosecond laser employed, can be used also for analysis of precious and rare samples such as silver jewels from different archaeological sites in Basilicata.

In addition another application of Laser Induced Breakdown Spectroscopy (LIBS), namely optical emission spectroscopy of laser-induced plasmas, has been used to analyze the plasma generated by nanosecond Nd: YAG for the evaluation of the role of the buffer gas on the plume evolution.

This study has been applied to a material useful for cathode in lithium ion batteries, i.e. $LiCoFePO_4$ in order to deposit by PLD thin films for micro batteries.

Stoichiometric thin films with high crystallinity have been obtained in presence of a buffer gas pressure of 100 Pa, without the necessity of thermal treatments.

This work has demonstrated how the physical study of laser induced plasma can be useful for a wide range of applications, that include the study of cultural heritage materials and the manufacture of high technology materials.